The Astrophysical Journal Supplement Series, 277:28 (48pp), 2025 March https://doi.org/10.3847/1538-4365/adb0b6

Weak-lensing Characterization of the Dark Matter in 29 Merging Clusters that Exhibit Radio Relics

Kyle Finner[1,2], M. James Jee[2,3], Hyejeon Cho[2,4], Kim HyeongHan[2], Wonki Lee[2], Reinout J. van Weeren[5], David Wittman[3], and Mijin Yoon[5]
[1] IPAC, California Institute of Technology, 1200 E California Boulevard, Pasadena, CA 91125, USA; kfinner@caltech.edu
[2] Department of Astronomy, Yonsei University, 50 Yonsei-ro, Seodaemun-gu, Seoul 03722, Republic of Korea
[3] Department of Physics and Astronomy, University of California, Davis, One Shields Avenue, Davis, CA 95616, USA
[4] Center for Galaxy Evolution Research, Yonsei University, 50 Yonsei-ro, Seodaemun-gu, Seoul 03722, Republic of Korea
[5] Leiden Observatory, Leiden University, P.O. Box 9513, 2300 RA Leiden, The Netherlands
Received 2024 June 25; revised 2025 January 13; accepted 2025 January 29; published 2025 March 4

Abstract

We present a multiwavelength analysis of 29 merging galaxy clusters that exhibit radio relics. For each merging system, we perform a weak-lensing analysis on Subaru optical imaging. We generate high-resolution mass maps of the dark matter distributions, which are critical for discerning the merging constituents. Combining the weak-lensing detections with X-ray emission, radio emission, and galaxy redshifts, we discuss the formation of radio relics from the past collision. For each cluster, we obtain mass estimates by fitting a multicomponent Navarro–Frenk–White model with and without a concentration–mass relation. We compare the mass estimates of each subcluster to their velocity dispersion measurements and find that they preferentially lie below the expected velocity dispersion scaling relation, especially at the low-mass end ($\sim 10^{14}\,M_{\odot}$). We show that the majority of the clusters that exhibit radio relics are in major mergers with a mass ratio below 1:4. We investigate the position of the mass peak relative to the galaxy luminosity peak, number density peak, and brightest cluster galaxy (BCG) locations and find that the BCG tends to better trace the mass peak position. Finally, we update a golden sample of eight galaxy clusters that have the simplest geometries and can provide the cleanest picture of the past merger, which we recommend for further investigation to constrain the nature of dark matter and the acceleration process that leads to radio relics.

Unified Astronomy Thesaurus concepts: Gravitational lensing (670); Weak gravitational lensing (1797); Dark matter distribution (356); Galaxy clusters (584); Shocks (2086); Intracluster medium (858); Large-scale structure of the universe (902)

1. Introduction

On large scales of the Universe, dark matter, gas, and stars are organized into galaxy clusters that are connected by filaments: the cosmic web (P. J. E. Peebles 1980; J. R. Bond et al. 1996). Galaxy clusters grow through the hierarchical buildup of mass where low-mass structures form and merge to produce more-massive structures. Major growth events occur when galaxy clusters merge.

Merging galaxy clusters provide an extreme environment to study the Universe in regions where the most energetic events since the Big Bang occur (C. L. Sarazin 2002). The merging of galaxy clusters is driven by the gravitational force. It begins with clusters detaching from the cosmic expansion and starting a Gyr-long plunge toward each other. As the outskirts of the galaxy clusters come in contact (a few virial radii separated), the intracluster medium (ICM), able to undergo electromagnetic interactions, feels a ram pressure as gas particles collide (see, for example, D. Eckert et al. 2012, for gas density profiles of clusters). The relative velocity of the galaxy clusters increases as they approach pericenter and particle interactions become more frequent. The clusters begin moving at supersonic velocities with Mach numbers in the range of 1–5 (S. Gabici & P. Blasi 2003). At these velocities, ram pressure becomes an important perturber of the ICM causing a significant momentum exchange between the gas of the two clusters and consequently a deceleration. Unlike the ICM, galaxies, being sparse in the cluster environment, are effectively collisionless and follow a path that gravity defines. This leads to the open and alluring question as to the nature of dark matter, the most massive component of galaxy clusters. The Bullet cluster (1E 0657-56) is a prime example of a cluster that is valuable to understanding the nature of dark matter. The cluster demonstrates a clear spatial separation of the ICM from the dark matter and galaxies (M. Markevitch et al. 2004; D. Clowe et al. 2006). This spatial configuration provides a laboratory to study the nature of dark matter (e.g., S. W. Randall et al. 2008).

A result of clusters colliding at supersonic velocities is the formation of shocks. These shocks can be classified as equatorial shocks that propagate perpendicular to the merger axis and bow (or axial) shocks that propagate along the merger axis (J.-H. Ha et al. 2018). Shocks are visible in X-ray observations as an abrupt surface brightness drop, but one must take care to not confuse them with contact discontinuities (e.g., M. Markevitch & A. Vikhlinin 2007). Shocks are also sometimes visible in radio observations as radio relics (also known as cluster radio shocks), which in some of the best cases appear as giant (up to a few Mpc) arc-shaped radio emission (see R. J. van Weeren et al. 2019 for a review).

Radio relics are extended synchrotron emission from charged particles that are accelerated by the magnetic fields of merger-induced shocks. It is postulated that diffusive shock acceleration (DSA; L. O. Drury 1983) is the primary acceleration mechanism. However, the inefficiency of DSA to accelerate electrons from a thermal distribution to energies that

are sufficient to see the observed radio relic brightness has been an issue given the low Mach number of these shocks (G. Brunetti & A. Lazarian 2007; H. Kang et al. 2012; A. Botteon et al. 2020a). The reacceleration of previously energized electrons is the favored scenario with evidence compounding (A. Bonafede et al. 2014; R. J. van Weeren et al. 2017; W. Lee et al. 2022). The rarity of radio relics, with not all merging clusters hosting them, remains another unresolved issue. Simulations have shown that projection may be somewhat to blame for the rarity of radio relics and the interpretation of radio emission (F. Vazza et al. 2012; S. W. Skillman et al. 2013; W. Lee et al. 2024). Furthermore, if reacceleration is required, then a preexisting population of suprathermal electrons should be present for the passing shock to accelerate.

Merging clusters are an ideal laboratory to study the nature of dark matter, high-energy astrophysics, and the evolution of the large-scale structure of the Universe. However, observations provide only a single snapshot into the Gyr-long process. Therefore, to gain an understanding of the progression of the merger, multiwavelength observations and a large sample of cluster mergers are needed. X-ray and radio observations provide insight into the ICM. Optical and IR observations track the galaxies. Dark matter, which by definition does not emit light, can be detected through its gravitational potential via the gravitational-lensing effect.

Weak gravitational lensing (WL hereafter) is a statistical analysis of galaxy shapes. WL analysis permits the detection of the total mass distribution of galaxy clusters (for a review, see K. Umetsu et al. 2020). It provides valuable information on the centroid and morphology of the dark matter. It can discern substructures and detect the connection to the large-scale structure (D. Eckert et al. 2015; K. HyeongHan et al. 2024b), which is critical to understanding the formation and evolution of clusters. Additionally, it can be used to estimate the masses of the substructures. By combining the WL results with multiwavelength observations of the ICM and stars, the past collision of merging clusters can be reconstructed.

This work entails a WL analysis of galaxy clusters that exhibit radio relics. The primary goal of the work is to identify and characterize the substructures that are merging using the WL effect. In Section 2, observations, data reduction, and photometry are described. Section 3 presents an overview of the WL pipeline, which covers WL formalism, point-spread function (PSF) modeling, source selection, lensing efficiency, convergence mapping, substructure identification, and mass estimation. Results for each cluster are described in Section 4, and the clusters are put into the context of the multiwavelength literature. Section 5 discusses the sample of clusters as a whole and presents a statistical analysis of the cluster masses. We summarize our conclusions in Section 6.

All magnitudes are presented in the AB magnitude system. In all calculations and presentations, a flat cold dark matter cosmology is assumed with $H_0 = 70\,\mathrm{km\,s^{-1}\,Mpc^{-1}}$, $\Omega_m = 0.3$, and $\Omega_\Lambda = 0.7$. Masses are defined as the mass within a sphere of radius R_Δ, where R_Δ is the radius at which the average density within is Δ times the critical density of the Universe at the redshift of the cluster.

1.1. Radio Relic Sample

The sample of clusters that are analyzed in this work exhibits Mpc-scale radio emission. The identification of the radio relics was done in past radio studies such as R. J. van Weeren et al. (2011b) and L. Feretti et al. (2012). Some of the clusters have bow-shaped radio emission that clearly resembles a spherical shock. However, some have patchy radio emission that may have arisen from other particle acceleration phenomena. The study of radio relics is a very active field of astronomy, and new insights into the nature of the radio relics are occurring daily. We include the most up-to-date information of the radio relics in our interpretations of the mergers.

By design, the galaxy clusters studied in this work are merging systems. This selection should be considered when making conclusions. The detection of these clusters is dependent on the brightness of the radio emission, and therefore, the sample is probing bright radio sources. Furthermore, the existence of the radio relics is an indication that the clusters are likely post-pericenter systems (F. Vazza et al. 2012; S. W. Skillman et al. 2013; W. Lee et al. 2024). Conclusions in this work are made with the understanding that the clusters belong to a small subset of galaxy clusters and may not be representative of all merging clusters.

Table 1 lists the radio relic merging clusters that are studied here. The sample of radio relic clusters range in redshift from 0.07–0.54. This range of redshifts is ideal for ground-based WL due to the dependence of the lensing signal on the distances of the lens and background galaxies. N. Golovich et al. (2019a, hereafter G19) performed a thorough dynamical analysis of the clusters utilizing a vast catalog of spectroscopic redshifts. Their study identified subclusters using Gaussian mixture modeling (GMM) and derived velocity dispersions. Combining X-ray and radio observations with the GMM-defined subclusters, they developed merger scenarios for each of the systems. A key finding of their study is that the majority of these clusters are merging near the plane of the sky. D. Wittman et al. (2018) provided quantitative constraints on the viewing angle of some of the clusters.

2. Observations and Data Reduction

Our analysis combines WL with X-ray, radio, and optical observations to provide a multiwavelength insight into past cluster–cluster merger events that resulted in radio relics. In this section, we describe the multiwavelength observations that we utilize in our analysis.

2.1. Subaru Observations

The observations used in this study to make WL measurements were obtained with the Subaru telescope. The Subaru telescope has a primary mirror diameter of 8.2 m and is an optical/infrared telescope located at the top of Maunakea on Hawaii. The optical observations used in this study come from two instruments: Suprime-Cam (S. Miyazaki et al. 2002) and Hyper Suprime-Cam (HSC; S. Miyazaki et al. 2018; Y. Komiyama et al. 2018; S. Kawanomoto et al. 2018; H. Furusawa et al. 2018). The Suprime-Cam is a 5 × 2 array of 4k × 2k Hamamatsu CCDs with a $34' \times 27'$ field of view. In 2017, the Suprime-Cam was decommissioned, and the HSC became the primary imager. The HSC is a 116 CCD instrument (104 science detectors) with a $1.^\circ5$ diameter field of view.

The imaging presented in this work are summarized in Table 2. For about one-third of the clusters, archival imaging is available. For those that lack Subaru imaging, additional observations were gathered by PI: D. Wittman and more recently by PI: H. Cho. These observations were performed

Table 1
Overview of 29 Merging Cluster Samples

Cluster	Short Name	R.A.	Decl.	Redshift	Discovery Band
1RXS J0603.3+4212	1RXSJ0603	06:03:13.4	+42:12:31	0.226	Radio
Abell 115	A115	00:55:59.5	+26:19:14	0.193	Optical
Abell 521	A521	04:54:08.6	−10:14:39	0.247	Optical
Abell 523	A523	04:59:01.0	+08:46:30	0.104	Optical
Abell 746	A746	09:09:37.0	+51:32:48	0.214	Optical
Abell 781	A781	09:20:23.2	+30:26:15	0.297	Optical
Abell 1240	A1240	11:23:31.9	+43:06:29	0.195	Optical
Abell 1300	A1300	11:32:00.7	−19:53:34	0.306	Optical
Abell 1612	A1612	12:47:43.2	−02:47:32	0.182	Optical
Abell 2034	A2034	15:10:10.8	+33:30:22	0.114	Optical
Abell 2061	A2061	15:21:20.6	+30:40:15	0.078	Optical
Abell 2163	A2163	16:15:34.1	−06:07:26	0.201	Optical
Abell 2255	A2255	17:12:50.0	+64:03:11	0.080	Optical
Abell 2345	A2345	21:27:09.8	−12:09:59	0.179	Optical
Abell 2443	A2443	22:26:02.6	+17:22:41	0.110	Optical
Abell 2744	A2744	00:14:18.9	−30:23:22	0.306	Optical
Abell 3365	A3365	05:48:12.0	−21:56:06	0.093	Optical
Abell 3411	A3411	08:41:54.7	−17:29:05	0.163	Optical
CIZA J2242.8+5301	CIZAJ2242	22:42:51.0	+53:01:24	0.189	X-ray
MACS J1149.5+2223	MACSJ1149	11:49:35.8	+22:23:55	0.544	X-ray
MACS J1752.0+4440	MACSJ1752	17:52:01.6	+44:40:46	0.365	X-ray
PLCK G287.0+32.9	PLCKG287	11:50:49.2	−28:04:37	0.383	SZ
PSZ1 G108.18−11.53	PSZ1G108	23:22:29.7	+48:46:30	0.335	SZ
RXC J1053.7+5452	RXCJ1053	10:53:44.4	+54:52:21	0.072	X-ray
RXC J1314.4−2515	RXCJ1314	13:14:23.7	−25:15:21	0.247	X-ray
ZwCl 0008.8+5215	ZwCl0008	00:11:25.6	+52:31:41	0.104	Optical
ZwCl 1447+2619	ZwCl1447	14:49:28.2	+26:07:57	0.376	Optical
ZwCl 1856.8+6616	ZwCl1856	18:56:41.3	+66:21:56	0.304	Optical
ZwCl 2341+0000	ZwCl2341	23:43:39.7	+00:16:39	0.270	Optical

Note. Source: N. Golovich et al. (2019b).

with WL analysis in mind. A dithering and rotation technique was executed to minimize degradation of the images from the diffraction spikes caused by bright stars, bad columns, cosmic rays, and bleeding trails. This imaging technique has been shown to increase the number of usable galaxies available for WL studies (M. J. Jee et al. 2015, 2016).

WL analysis requires a careful modeling of the PSF because it mimics the lensing effect. For ground-based observations, the PSF is predominately affected by atmospheric seeing. Subaru observations were obtained in some of the best seeing conditions with typically subarcsecond seeing achieved (Table 2). For each cluster, we selected the filter for WL analysis by carefully balancing exposure time (maximize) and seeing (minimize) with a preference given to the redder filter when the choice was close. Redder filters are preferred in WL analysis because the redder light from galaxies tends to be less clumpy than the blue, star-forming light and is thus better fit with a smooth model (B. Lee et al. 2018). The filter selected for WL is highlighted in bold font in Table 2.

2.2. Subaru Data Reduction

Data reduction requires special care to produce a WL-quality image. Subaru `SDFRED` 1 (pre 2009) and 2 (post 2009) packages[6] were used for the basic reduction steps of overscan subtraction, bias correction, flat-fielding, and distortion correction for the Suprime-Cam images. SExtractor (E. Bertin & S. Arnouts 1996) was run on each frame to prepare a catalog of objects for SCAMP (E. Bertin 2006). SCAMP was applied to correct for residual distortions and to refine the World Coordinate System (WCS) for each frame. We used the Pan-STARRS photometric catalog (K. C. Chambers et al. 2016) as a reference in SCAMP to compute the astrometry. For the HSC images, the LSST Science Pipelines (J. Bosch et al. 2018, 2019; T. Jenness et al. 2022) were used for overscan/bias/dark subtraction, flat-fielding, astrometric correction, etc.

The final step in creating a WL-quality image is to coadd the frames into a mosaic image. The best signal-to-noise ratio (S/N) mosaic is created by mean averaging the frames. However, the frames are prone to cosmic rays, saturation trails, and other detector effects. For this reason, a two-step process was used to coadd the frames. First, SWarp (E. Bertin et al. 2002) was applied to the frames to generate a median-stacked mosaic image. In preparation for coaddition, SWarp translates, rotates, and distortion corrects the frames. These individual `RESAMP` frames are critical to our PSF modeling (Section 3.2) and were stored for later use. After resampling, the frames were carefully aligned using the WCS solution from SCAMP and coadded by SWarp into a median-stacked mosaic image. The median-stacking process outputs a weight file for each component frame. We utilized the weight files to remove the aforementioned spurious signals. The median-stacked mosaic image was compared to the `RESAMP` frames, and pixels from

[6] http://subarutelescope.org/Observing/Instruments/SCam/sdfred

Table 2
Subaru Imaging

Cluster	Filters	Dates	Seeing (arcseconds)	Exp. Time (s)	Src. Dens. (arcmin^{-2})	$\langle\beta\rangle$	$n_{\rm in}/n_{\rm out}$
1RXSJ0603	*g*, ***r***	2014/02/25	0.57, **0.57**	720, **2800**	31	0.66	1.01 ± 0.06
A115	***V***, *i*	2003/09/25, 2005/10/03	**0.58**, 0.65	**1530**, 2100	24	0.54	1.04 ± 0.06
A521	*V*, *R*, ***i***	2001/10/14, 2001/10/15	0.59, 0.65, **0.59**	1800, 1620, **2040**	44	0.63	1.05 ± 0.06
A523	*g*, ***r***	2014/02/26	1.00, **0.78**	720, **2880**	19	0.81	1.05 ± 0.06
A746	*g*, ***r2***	2023/01/16,20,22	1.26, **0.75**	3480, **4320**	24	0.63	1.14 ± 0.06
A781	*V*, ***i***	2010/03/14, 2010/03/15	0.90, **0.80**	3360, **2160**	28	0.55	0.95 ± 0.06
A1240	*g*, ***r***	2014/02/25	0.67, **0.58**	720, **2880**	43	0.73	1.02 ± 0.05
A1300	*g*, ***r***	2014/02/26	0.89, **0.88**	720, **2913**	23	0.55	0.98 ± 0.05
A1612	*g*, ***i***	2014/02/25, 2010/04/11	0.62, **0.65**	2880, **1920**	19	0.70	1.02 ± 0.06
A2034	*g*, ***R***	2005/04/11, 2007/06/19	0.82, **0.90**	720, **12880**	35	0.82	0.98 ± 0.05
A2061	*g*, ***r***, *i*	2013/07/13, 2014/02/26	0.68, **0.67**, 0.65	720, **2550**, 4120	41	0.87	1.07 ± 0.05
A2163	*V*, ***R***	2009/04/30, 2008/04/07	0.70, **0.75**	2100, **4500**	27	0.69	1.02 ± 0.06
A2255	*B*, *R*, ***i***	2007/08/14, 2008/07/30	0.98, 1.00, **0.64**	1260, 2520, **1200**	26	0.86	0.96 ± 0.05
A2345	*V*, ***i***	2005/10/03, 2010/06/10, 2010/11/08	0.70, **0.72**	3600, **2100**	17	0.68	0.99 ± 0.06
A2443	…	…	…	…	…	…	…
A2744	*B*, *R*, ***z***	2013/07/15, 2013/07/16	1.00, 1.14, **0.79**	2100, 3120, **3600**	25	0.52	0.92 ± 0.06
A3365	*g*, *r*, ***i***	2014/02/25	0.97, 0.71, **0.62**	720, 720, **2880**	20	0.81	…
A3411	*g*, *r*, ***i***	2014/02/25	0.8, 0.82, **0.77**	1000, 720, **2880**	13	0.69	0.95 ± 0.06
CIZAJ2242	*g*, ***i***	2013/07/13	0.63, **0.55**	720, **2880**	14	0.62	0.96 ± 0.06
MACSJ1149	*V*, ***R***	2003/04/05, 2005/03/05, 2010/03/18	0.90, **0.86**	2520, **5490**	26	0.40	0.84 ± 0.10
MACSJ1752	*g*, *r*, ***i***	2013/07/13	0.62, 0.64, **0.73**	2520, 720, **4400**	26	0.62	0.98 ± 0.06
PLCKG287	*g*, ***r***	2014/02/26	0.81, **0.97**	720, **2880**	27	0.55	1.08 ± 0.07
PSZ1G108	*g*, ***i2***	2017/08/20, 2017/08/19	0.65, **0.72**	1440, **2880**	15	0.48	0.93 ± 0.09
RXCJ1053	*g*, ***r***	2014/02/26	0.83, **0.92**	720, **2910**	…	…	…
RXCJ1314	*g*, ***r***	2014/02/25	0.86, **0.71**	720, **2880**	18	0.64	0.96 ± 0.06
ZwCl0008	*g*, ***r***	2013/07/13	0.52, **0.57**	720, **2880**	24	0.81	1.06 ± 0.05
ZwCl1447	*g*, ***r***, *i*	2014/02/26	0.91, **0.76**, 0.55	720, **2880**, 720	44	0.52	0.99 ± 0.06
ZwCl1856	*g*, ***r***	2015/09/12	0.70, **0.65**	720, **2520**	31	0.55	1.07 ± 0.06
ZwCl2341	*g*, ***r***	2013/07/13	0.49, **0.50**	720, **2880**	20	0.69	0.95 ± 0.06

Note. The filter used for WL is in bold font. Exp. Time is the total exposure time per band, Src. Dens. is the source density of galaxies used for WL, and $n_{\rm in}/n_{\rm out}$ is the number density ratio of WL sources within 750 kpc (in) and from 750–1500 kpc (out).

the RESAMP frames that deviated more than 3 times from the rms of the median-stacked image were set to zero in the corresponding weight file. A second pass of SWarp was done by weight-averaging the input frames, and a mean-stacked mosaic image was created. This process was performed on the filter with the longest exposure time first, and then the header information was applied to the remaining filters to ensure the same alignment and footprint.

Figure 1 presents a color version of the coadded mosaic for galaxy cluster A2061. The three channels of the RGB image are *i*, *r*, and *g*, respectively. The rotation and dithering technique is noticeable around the edges of the mosaic and the benefit of the technique is apparent by comparing the bright star in the center to the stars near the edge. The Suprime-Cam's large field of view provides ample coverage to perform a WL analysis of a galaxy cluster (∼4 Mpc diameter field of view at $z = 0.1$).

2.3. Keck/DEIMOS Observations

Throughout this study, we utilize redshifts that were measured from Keck DEep Imaging Multi-Object Spectrograph (DEIMOS) observations. The survey and data reduction of the observations are thoroughly described in N. Golovich et al. (2019b). G19 performed an analysis of the spectroscopic redshifts and identified subclusters utilizing a GMM method.

2.4. MMT Hectospec Observations and Data Reduction

Some of the clusters in G19 have insufficient numbers of spectroscopic redshifts to discern substructures. We collected MMT/Hectospec (D. Fabricant et al. 2005) fiber observations (PI: K.Finner) at the 6.5 m monolithic-mirrored MMT telescope on Mount Hopkins, Arizona. Cluster targets were selected based on the scarcity of their spectroscopic coverage and on the prospect of them having detectable large-scale filaments. The MMT/Hectospec is an efficient instrument for simultaneously achieving these two scientific goals because it has a 1° diameter field of view and 300 fibers. However, fibers collide at distances of about 20″, which limits how densely the cores of clusters can be sampled, especially for those at higher redshifts.

We observed A521, A746, A1240, and A2443 with approximately 1.5 hr of exposure time each. Two configurations of the Hectospec instrument were designed for each galaxy cluster utilizing the 270 grating (spectral range 3650–9200 Å). The goal of the observations was to securely measure redshifts for galaxies that reside in the clusters. We plotted color–magnitude diagrams (CMDs) from Subaru imaging for A521, A746, and A1240 and Sloan Digital Sky

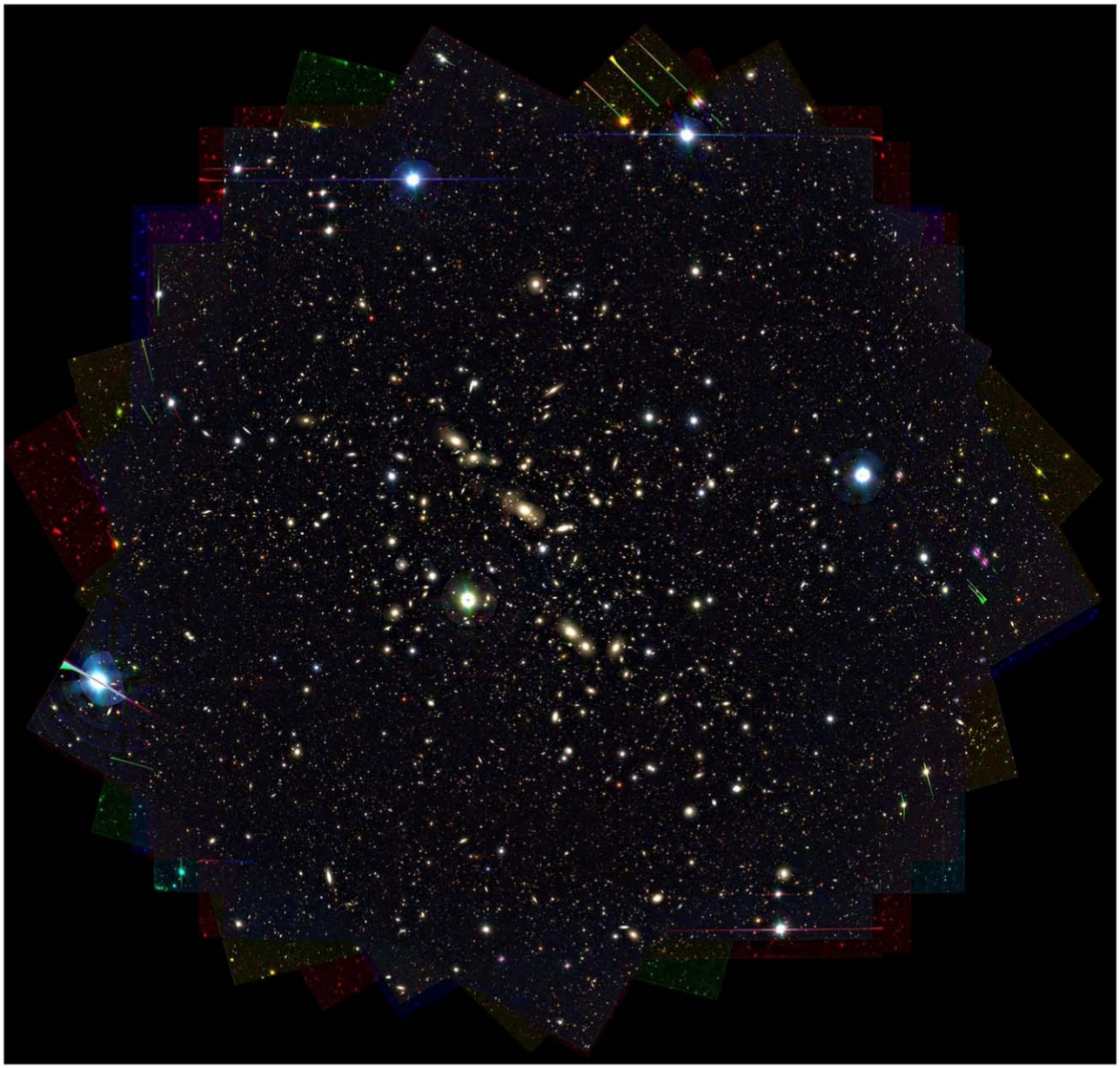

Figure 1. The Subaru color image of the galaxy cluster A2061 provides an example of the quality of the imaging (blue = g band, green = r band, red = i band). The rotation and dithering technique of the observations is noticeable at the perimeter of the image and is beneficial to WL analysis because it minimizes the diffraction spikes caused by stars and allows for a better sampling of the PSF.

Survey (SDSS) imaging for A2443. The spectroscopically confirmed cluster galaxies in the CMD form a red sequence. We fit a line to the red sequence to select cluster member candidates that fall within a color range of $g - r \pm 0.1$ with the r-band brightness limit set to 21.5.

Raw spectra were processed with the `hs_pipeline_wrap` command in HSRED 2.1[7] to produce sky-subtracted and variance-weighted spectra. The IRAF add-on RVSAO (M. J. Kurtz & D. J. Mink 1998) was used to cross-correlate a set of template spectra and estimate redshifts. To select robust redshift estimates, we only retained estimates with a cross-correlation r-value > 4. The MMT/Hectospec redshift catalogs are published in M. Yoon et al. (2020) for A521, H. Cho et al. (2022) for A1240, K. HyeongHan et al. (2024a) for A746, and H. Cho et al. (2025, in preparation) for A2443.

2.5. Archival Radio and X-Ray Observations

In this study, we rely on archival radio and X-ray observations to investigate the relation of dark matter and ICM. Table 3 summarizes the sources of the radio and X-ray data. Radio images were kindly provided by the authors listed in the Radio References column. X-ray data were retrieved from the respective archive and processed.

Chandra observations were downloaded from the Chaser[8] archive. Utilizing the Python version of the CIAO[9] package,

[7] https://github.com/MMTObservatory/hsred

[8] https://cda.harvard.edu/chaser/

[9] https://cxc.cfa.harvard.edu/ciao/

Table 3
Archival Radio and X-Ray Imaging Utilized in This Study

Cluster	Radio Image	Radio References	X-Ray Telescope	Exposure (ks)
1RXSJ0603	GMRT 610 MHz	R. J. van Weeren et al. (2012b)	Chandra	250
A115	LOFAR 150 MHz	A. Botteon et al. (2022a)	Chandra	360
A521	MeerKAT 1.3 GHz	K. Knowles et al. (2022)	Chandra	170
A523	VLA 1.4 GHz	R. J. van Weeren et al. (2011b)	Chandra	30
A746	LOFAR 150 MHz	A. Botteon et al. (2022a)	XMM-Newton	184
A781	LOFAR 150 MHz	A. Botteon et al. (2022a)	Chandra	48
A1240	LOFAR 150 MHz	A. Botteon et al. (2022a)	Chandra	52
A1300	GMRT 325 MHz	T. Venturi et al. (2013)	Chandra	100
A1612	GMRT 325 MHz	R. J. van Weeren et al. (2011b)	Chandra	31
A2034	LOFAR 150 MHz	A. Botteon et al. (2022a)	Chandra	261
A2061	LOFAR 150 MHz	A. Botteon et al. (2022a)	Chandra	32
A2163	VLA 1.4 GHz	L. Feretti et al. (2001)	Chandra	90
A2255	WSRT 350 MHz	R. F. Pizzo & A. G. de Bruyn (2009)	XMM-Newton	42
A2345	VLA 1.4 GHz	A. Bonafede et al. (2009)	XMM-Newton	93
A2443	VLA 325 MHz	A. S. Cohen & T. E. Clarke (2011)	Chandra	116
A2744	MeerKAT 1.3 GHz	K. Knowles et al. (2022)	Chandra	132
A3365	VLA 1.4 GHz	R. J. van Weeren et al. (2011b)	XMM-Newton	161
A3411	GMRT 325 MHz	R. J. van Weeren et al. (2017)	Chandra	215
CIZAJ2242	WSRT 1382 MHz	R. J. van Weeren et al. (2010)	Chandra	206
MACSJ1149	LOFAR 150 MHz	L. Bruno et al. (2021)	Chandra	372
MACSJ1752	LOFAR 150 GHz	A. Botteon et al. (2022a)	XMM-Newton	13
PLCKG287	GMRT 325 MHz	A. Bonafede et al. (2014)	Chandra	200
PSZ1G108	GMRT 323 MHz	F. de Gasperin et al. (2015)	Chandra	27
RXCJ1053	WSRT 1382 MHz	R. J. van Weeren et al. (2011b)	Chandra	31
RXCJ1314	MeerKAT 1.3 GHz	K. Knowles et al. (2022)	XMM-Newton	110
ZwCl0008	WSRT 1382 MHz	R. J. van Weeren et al. (2011c)	Chandra	411
ZwCl1447	GMRT 700 MHz	W. Lee et al. (2022)	Chandra	30
ZwCl1856	LOFAR 150 MHz	A. Jones et al. (2021)	XMM-Newton	12
ZwCl2341	GMRT 610 MHz	R. J. van Weeren et al. (2009)	Chandra	227

the multiple visits for each cluster were reprocessed and combined into a broad flux image containing emission from 0.5–7 keV. For this reduction, we followed the Diffuse Emission tutorial.

XMM-Newton images were downloaded from the XMM-Newton science archive.[10] The images were reduced and combined with the SAS pipeline following the procedures for diffuse extended sources described in the XMM-ESAS Cookbook.[11] The final combined images have an energy range of 0.5–7 keV.

Unless otherwise stated, the X-ray imaging processed through these methods are used purely for qualitative analysis.

2.6. Object Detection and Photometry

The detection of the WL signal requires a statistical analysis of galaxy shapes. A main source of noise that contributes to a WL analysis is shape noise, which is caused by the dispersion of the intrinsic ellipticity of galaxies. To reduce the contribution from shape noise, a large number of galaxies is needed. Therefore, we optimize our object detection method to robustly detect as many galaxies as possible.

We performed photometry with SExtractor (E. Bertin & S. Arnouts 1996) in dual-image mode. As the name implies, dual-image mode uses two images. The detection image is kept constant while the measurement image is varied between runs to ensure that the resulting filter-specific catalogs have the same objects. For each cluster, we created a detection image by weight-averaging all available filters together. When running SExtractor, a weight image for the detection image was provided that was created by weight-averaging the SWarp weight images together. Measurements were taken on the measurement image (one for each filter) with an rms image provided for weighting. The rms image was created by multiplying the weight image of the filter by the background rms of its mosaic and masking spurious pixels. Our configuration of SExtractor set `DETECT_MINAREA` to 5 pixels and `DETECT_THRESH` to 2 pixels. The settings for deblending were `DEBLEND_NTHRESH` of 32 and `DEBLEND_MINCOUNT` of 10^{-4} to maximize detection of overlapping objects.

The Subaru photometric zero-point was calibrated by matching stars to an external star catalog. The first choice was the SDSS DR14 photometric catalog, but when not available (due to decl.), the Pan-STARRS DR1 catalog was used. In all cases, the difference in filter throughput was accounted for by performing synthetic photometry (M. Sirianni et al. 2005). To derive the correct photometric zero-point, the magnitude of stars from the reference catalog were compared to the SExtractor `MAG_AUTO` measurements. The left panel of Figure 2 displays the magnitude difference as a function of magnitude for the stars in the A2061 *r*-band image. Instead of relying on the full population of stars, we selected unsaturated stars from the stellar locus, as shown in the right panel. The magnitude difference follows a linear relation over the region shown, and in most cases has a slope close to 0. We repeated this method for each filter and applied the linear calibration to the Subaru magnitudes.

[10] http://nxsa.esac.esa.int/nxsa-web/
[11] http://heasarc.gsfc.nasa.gov/docs/xmm/esas/cookbook/

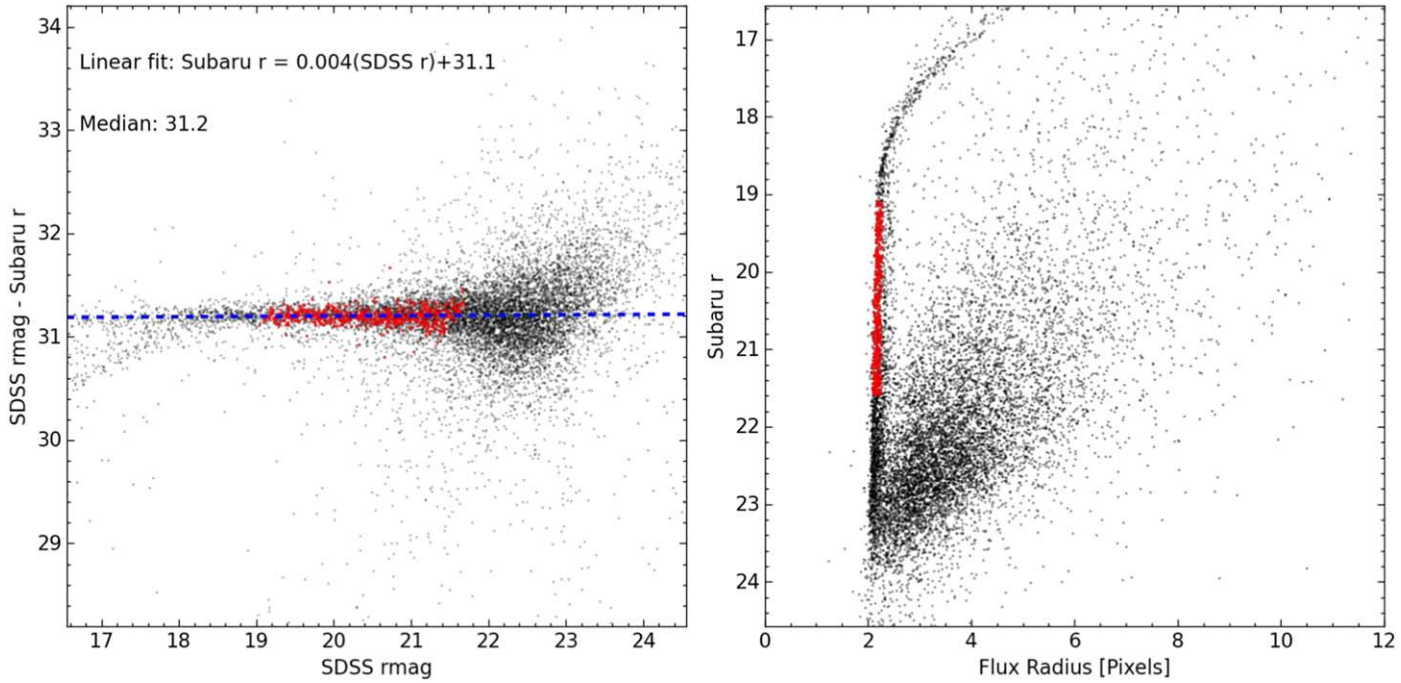

Figure 2. Photometric zero-point calibration of A2061 (left panel). The SDSS catalog is used as a reference. Stars (red circles) are selected from the size–magnitude plot (right panel) and matched with stars in the reference catalog. The magnitude offset as a function of SDSS *r*-band magnitude is plotted, and a linear fit to the stars is made to determine the zero-point. The same stars are utilized in PSF modeling.

3. WL Theory and Methodology

3.1. Gravitational-lensing Formalism

M. Bartelmann & P. Schneider (2001), H. Hoekstra (2013), and M. Meneghetti (2022) provide comprehensive reviews of gravitational-lensing theory. For brevity, we state the critical ideas and nomenclature that are required to understand our analysis.

The gravitational-lensing effect is caused by the deflection of light by a gravitational potential. The deflection of light leads to a shift in the apparent position of the light source, a galaxy in our case. The relation between the true source position $\boldsymbol{\eta}$ and the observed position $\boldsymbol{x}$ is

$$\boldsymbol{\eta} = \boldsymbol{x} - \boldsymbol{\alpha}(\boldsymbol{x}), \tag{1}$$

where

$$\boldsymbol{\alpha}(\boldsymbol{x}) = \frac{1}{\pi}\int \kappa(\boldsymbol{x}')\frac{\boldsymbol{x}-\boldsymbol{x}'}{|\boldsymbol{x}-\boldsymbol{x}'|^2}d^2\boldsymbol{x} \tag{2}$$

is the scaled deflection angle. The scaling depends on the convergence

$$\kappa(\boldsymbol{x}) = \frac{\Sigma(\boldsymbol{x})}{\Sigma_c}, \tag{3}$$

which is a dimensionless quantity of the projected mass density divided by the lensing critical density. The lensing critical density is

$$\Sigma_c = \frac{c^2 D_s}{4\pi G D_l D_{ls}}, \tag{4}$$

where D_l is the angular diameter distance to the lens, D_s is the angular diameter distance to the source, D_{ls} is the angular diameter distance from lens to source, c is the speed of light, and G is the gravitational constant. The ratio $\beta = D_{ls}/D_s$ is referred to as the lensing efficiency.

The tidal gravitational field causes an anisotropic distortion, called the shear (γ), that stretches galaxy images tangential to the local gravitational potential gradient. When the gravitational-lensing effect is in the weak regime ($\kappa \ll 1$, $\gamma \ll 1$), single galaxy images appear, and the distortions are small. N. Kaiser & G. Squires (1993) showed that the shear and convergence are related by the convolutions

$$\kappa(\boldsymbol{x}) = \frac{1}{\pi}\int D^*(\boldsymbol{x}-\boldsymbol{x}')\gamma(\boldsymbol{x}')d^2\boldsymbol{x}', \tag{5}$$

$$\gamma(\boldsymbol{x}) = \frac{1}{\pi}\int D(\boldsymbol{x}-\boldsymbol{x}')\kappa(\boldsymbol{x}')d^2\boldsymbol{x}', \tag{6}$$

where $D(\boldsymbol{x}) = -1/(x_1 - ix_2)^2$ is the convolution kernel.

Observationally, we detect the reduced shear

$$g = \frac{\gamma}{1-\kappa}, \tag{7}$$

which is the combination of the convergence and the shear. The distortions caused by WL may be expressed by the Jacobian matrix

$$A = (1-\kappa)\begin{bmatrix} 1-g_1 & -g_2 \\ -g_2 & 1+g_1 \end{bmatrix}. \tag{8}$$

The reduced shear is encoded as a complex term ($g = g_1 + ig_2$) where positive (negative) values of g_1 distort galaxy images along the $x(y)$-directions and positive(negative) values of g_2 distort images along the $x = y(x = -y)$-directions. In this work, we define the ellipticity (shape) of galaxies as $e = (a-b)/(a+b)$, where a and b are the semimajor and semiminor axes, respectively. Each observed galaxy has a measured ellipticity

that includes its intrinsic shape and the local shear

$$e \approx e_{\rm intrinsic} + g. \quad (9)$$

Under the assumption that galaxy images have random orientations, the averaged ellipticity of galaxy images is the reduced shear

$$\langle e \rangle \approx g. \quad (10)$$

3.2. Point-spread Function Modeling

WL requires the careful measurement of galaxy shapes. However, the turbulent atmosphere and the diffraction of light through the telescope cause a significant anisotropic blurring of the galaxy images. It is critical for a WL analysis to properly model and remove the effect of the PSF. For our analysis, we utilize a principal component analysis (PCA) approach to deriving a spatial and temporal PSF model. M. J. Jee et al. (2007) showed that the PCA approach accounts for small- and large-scale structures of the PSF. PCA is also beneficial because it derives the basis functions from the data set itself and requires few components. The PCA technique that is used in this work has been applied to a variety of space- and ground-based observations (K. Finner et al. 2017, 2020, 2023b, 2023c; K. HyeongHan et al. 2020, 2024a) including the James Webb Space Telescope (JWST) in K. Finner et al. (2023a).

The dynamic atmosphere causes the PSF of Subaru to vary temporally and spatially. Furthermore, both the Suprime-Cam and HSC have a large field of view, which leads to a complex PSF across the full mosaic that is difficult to interpolate and suffers from discontinuities at CCD boundaries (in a similar fashion to that shown in the Deep Lens Survey; M. J. Jee et al. 2013). To resolve these issues, we create PSF models on a frame-by-frame basis and then stack them into a final PSF model that is usable for measurement from the coadded mosaic.

For brevity, we will list the steps of the PSF pipeline. For an in-depth explanation of the pipeline, we refer the reader to K. Finner et al. (2017). First, a PCA is performed on stars that best represent the PSF (isolated, bright but not saturated, etc.).

1. Select stars for each frame based on size and magnitude. The right panel of Figure 2 illustrates the selection process for one cluster. Create 21 pixel by 21 pixel postage stamps of each selected star and shift them to be centered on the cutout.
2. Store the mean star and a residual array (N stars by 441 pixels) that is created by subtracting the mean star from each individual star.
3. Perform a PCA of the residual and keep the 21 components with the highest variance. The choice for keeping 21 components was found empirically by evaluating the PSF residuals as presented later in this section.

The PCA and the mean star can be utilized to generate a PSF at any position in the frame, which can then be stacked into PSF models for the coadded mosaic as follows.

1. Fit the PCA result with a third-order polynomial.
2. Add the fitted PCA result onto the mean star.
3. Repeat for all objects of interest in the frame.
4. For each object in the mosaic image, determine which frames compose the mosaic and stack the PSF models for those frames to a coadded PSF model.

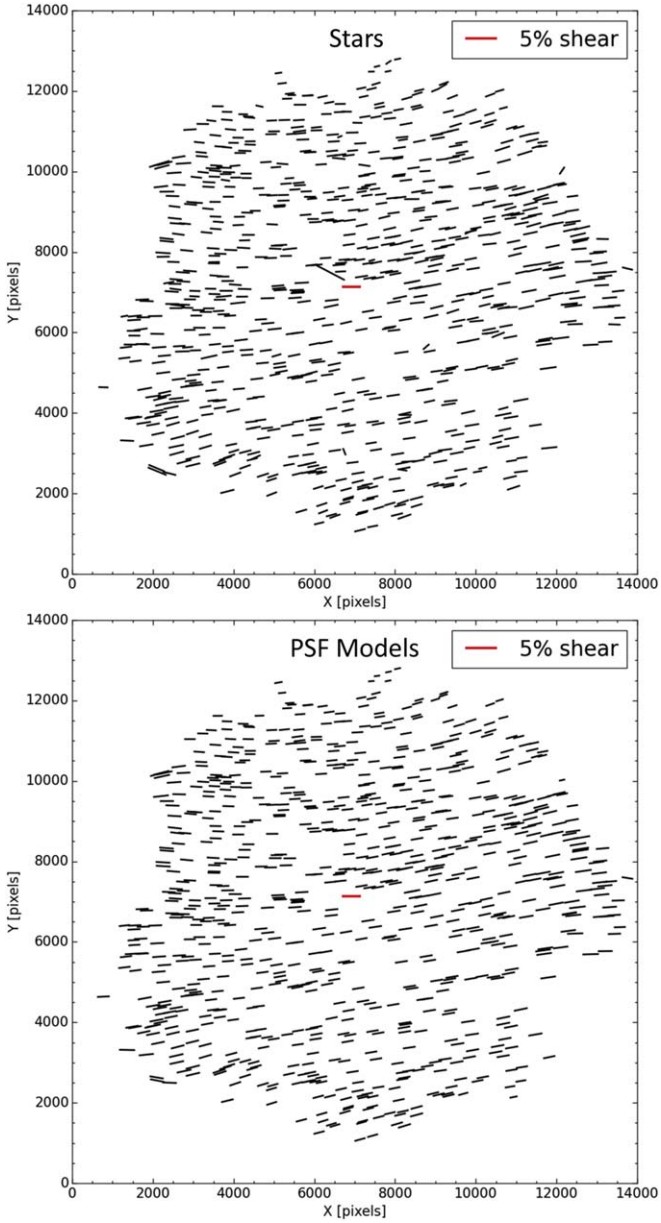

Figure 3. A2061 PSF distortion. Top: measured ellipticity of a selection of stars from the mosaic coadded image. The lines represent the direction and magnitude of the ellipticity of stars. Outliers have not been removed and clearly do not follow the general trend of the PSF. Bottom: ellipticity of the model PSFs at each star location. Models are designed in each component frame and stacked to a coadded PSF. Comparing the top and bottom panels shows that the measured stellar shape is well reproduced by the PSF model.

Figure 3 compares the ellipticity of stars (top) in A2061 to the corresponding PSF models (bottom). In most cases, the PSF models trace the magnitude and direction of the ellipticity of stars. Figure 4 displays the statistics of the correction made by the PSF model. The red circles are the ellipticity of stars in the mosaic. By subtracting the ellipticity of the PSF model for each star, we get the residual (black circles). There are two desired effects that are important to see when comparing the measured ellipticity of stars and the residual. First, the distribution should shift toward 0 if the average ellipticity is being corrected. Second, the distribution should tighten if the spatial variation of the ellipticity is being corrected. We see that both effects are being corrected for. A2061 demonstrates the typical residual

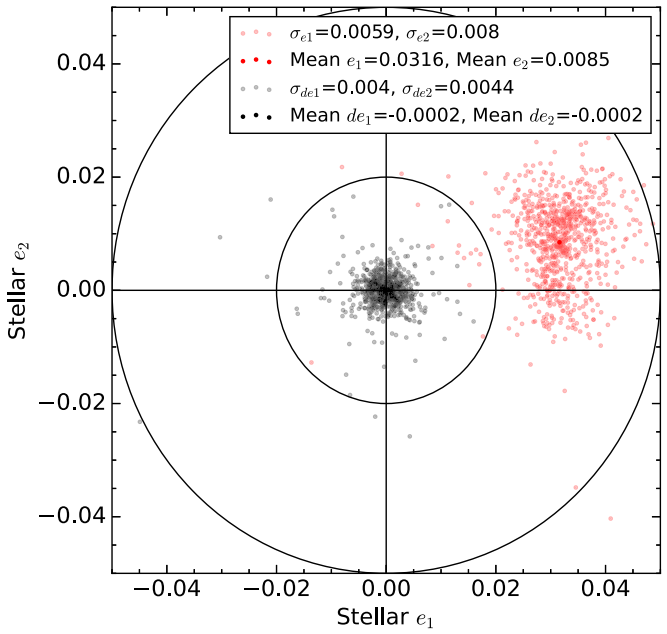

Figure 4. A2061 PSF model correction. Red circles denote the observed ellipticity of stars. Black circles are the corrected ellipticities where the PSF model ellipticities have been subtracted from the observed ellipticities of their respective stars. The figure demonstrates that the ellipticity is being corrected. The goal is to tighten the dispersion and shift the centroid to zero. As the legend shows, the dispersion is decreased by ~2, and the centroid is corrected to the 10^{-4} level.

for our PSF models with a mean ellipticity residual of the order of 10^{-4} and standard deviation of 10^{-3}. This level of accuracy is sufficient for WL analysis of galaxy clusters.

3.3. Galaxy Shape Measurement with PSF Correction

Detection of the WL effect requires a statistical analysis of the shapes of distorted galaxy images. We employed a model-fitting technique to measure the shapes of galaxies. For each cluster, we follow the same recipe for measuring galaxy shapes.

To measure the shape of a single galaxy, we cut out a postage stamp image of the galaxy from the mosaic image. A corresponding rms noise postage stamp $\sigma_{\rm rms}$ was also cut out from the rms mosaic image. It is important to consider the size of the postage stamp image. A large postage stamp image will contain the light from nearby objects, which may significantly alter the shape measurement. However, a small postage stamp may prematurely truncate the galaxy light profile and lead to truncation bias (R. Mandelbaum 2018). We chose to cut large postage stamp images that are 8 times the size of the half-light radius as measured by SExtractor (E. Bertin & S. Arnouts 1996), with a 10 pixel floor for very small objects. Making use of the SExtractor segmentation map, we masked any nearby bright objects that could influence the shape measurement by setting the relevant pixels in the rms noise postage stamp to 10^6.

We fit an elliptical Gaussian function, G, to the postage stamp image, I, while forward modeling the corresponding PSF model, P, as follows:

$$\chi^2 = \sum \left(\frac{I - G \circledast P}{\sigma_{\rm rms}} \right)^2, \tag{11}$$

where the summation is over the pixels of the postage stamp. The elliptical Gaussian function has seven free parameters: background, amplitude, position (x and y), semimajor axis (a), semiminor axis (b), and orientation angle (ϕ). To fit the galaxies, we utilized a Python version of the Levenburg–Marquardt least-squares fitting code MPFIT. Uncertainties returned by MPFIT are determined from the Hessian matrix and assume a Gaussian distribution. We fixed the background, x, and y to the SExtractor values of `BACKGROUND`, `XWIN_IMAGE`, and `YWIN_IMAGE` while fitting the remaining four parameters. Complex ellipticities were determined from the fitted values of a, b, and ϕ as

$$e_1 = \frac{a-b}{a+b} \cos 2\phi,$$
$$e_2 = \frac{a-b}{a+b} \sin 2\phi. \tag{12}$$

Galaxy shape measurement techniques suffer from biases that must be corrected for. The biases are typically encoded into a linear correction factor with a multiplicative and additive bias. We derived a calibration factor from simulations of our pipeline to correct for multiplicative bias. Following the technique called SFIT (M. J. Jee et al. 2013), which was the best-performing technique in the GREAT3 challenge (R. Mandelbaum et al. 2015), we processed simulated images with our Subaru WL pipeline and compared the input shear to the measured shear. We found that a multiplicative calibration factor of 1.15 was necessary to correct the biases of our pipeline, and that additive biases were low ($<10^{-4}$).

For each cluster, galaxy shape measurements were made in the WL image (see Table 2), and shape catalogs were compiled. The shape catalogs created through this procedure will be further culled in the following sections to a background source catalog that ideally contains only lensed galaxies.

3.4. Source Selection

The ideal catalog for a WL analysis contains only galaxies that are at a greater distance than the lens (cluster) from the observer. Having distance measurements for each galaxy would make source selection trivial. However, gathering spectroscopic redshifts for all background galaxies is an immense undertaking. Photometric redshifts are a second option, but a reliable redshift requires vast multiband imaging, which is not readily available for our sample of galaxy clusters. We instead rely on colors and magnitudes to separate foreground, cluster, and background galaxies.

There are multiple properties of galaxies that are useful for placing galaxies into these three categories. Galaxies residing in a cluster environment tend to have lower star formation rates, an overall older population of stars, and a large amount of dust compared to field galaxies (A. Dressler 1984). In addition, an accumulation of metals that are deposited by past star formation leads to a prominent feature in the spectral energy distribution of evolved cluster galaxies called the 4000 Å break. The 4000 Å break manifests a red-sequence relation in a CMD when observed with two filters that bracket the feature. In the redshift range of our sample (0.07–0.54), the 4000 Å break is well bracketed by the g and r or g and i filters. Figure 5 presents the CMD of A2061. The red sequence is clearly marked by the red circles of spectroscopically confirmed cluster galaxies. However, it can also be seen extending to fainter magnitudes within the green, dashed rectangle. We make a photometric selection of cluster galaxy candidates (dashed, green rectangle) by extending the red sequence to an r-band magnitude of 21.

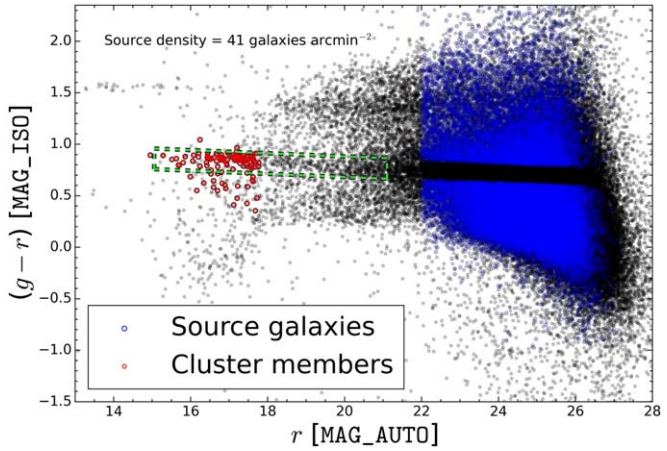

Figure 5. CMD for A2061 with $g - r$ [MAG_ISO] color and r [MAG_AUTO] from SExtractor. Red circles represent the spectroscopically confirmed cluster member galaxies within $z \pm 0.03$ of the cluster redshift. The green dashed box highlights the photometrically selected sample of cluster member candidates based on a linear fit to the red sequence. Background galaxies (blue circles) are selected following the criteria described in Section 3.4. A red selection of source galaxies is included for A2061 because of its low redshift ($z = 0.08$).

We opt to select galaxies that are within 0.1 in $g - r$ color to the linear fit, which encapsulates the majority of red-sequence galaxies. Following this recipe, we create a catalog of cluster galaxies that are used to plot galaxy luminosity and number density maps in Section 4.

The color and magnitude properties are also useful for selecting background galaxies. Galaxies behind the cluster are on average fainter than the cluster members, as apparent brightness is proportional to inverse-squared distance. Identifying background galaxies based on color is more complicated. The cosmological expansion of space redshifts galaxy emission. However, there is the competing evolutionary effect where galaxies at greater distances appear on average to be younger than nearby galaxies. When viewed through the color of $g - r$ or $g - i$, the evolutionary effect tends to be stronger than the redshift effect beyond a redshift of 0.5, which leads to background galaxies being bluer than cluster and foreground galaxies (see T. Schrabback et al. 2018, for an example). Therefore, we select galaxies that are bluer than the red sequence for clusters that are above a redshift of 0.2. Below a redshift of 0.2, limiting the background galaxy catalog to only sources that are bluer than the red sequence leads to a low source density. Therefore, in these cases, we include both red and blue galaxies in our source catalog but reject the galaxies that exist in the color space that follows the red sequence. The CMD for A2061 in Figure 5 shows this selection technique. In all cases, we set a brightness limit for the source catalog of 22nd magnitude because the likelihood of brighter galaxies being foreground or cluster galaxies is high.

Some weak-lensing studies have shown that selecting source galaxies from color–color relations can effectively remove a significant portion of foreground and cluster galaxies that dilute the lensing signal (see E. Medezinski et al. 2010; K. Umetsu et al. 2014, and references therein). Our tests indicate that two-band imaging is also effective at selecting background galaxies while limiting contamination from foreground and cluster member galaxies. In Figure 6, we utilize the COSMOS2020 photometric redshift catalog (J. R. Weaver et al. 2022) to estimate the contamination from foreground galaxies. When the color constraint is loose (HSC-g − HSC-r < 2), the relations

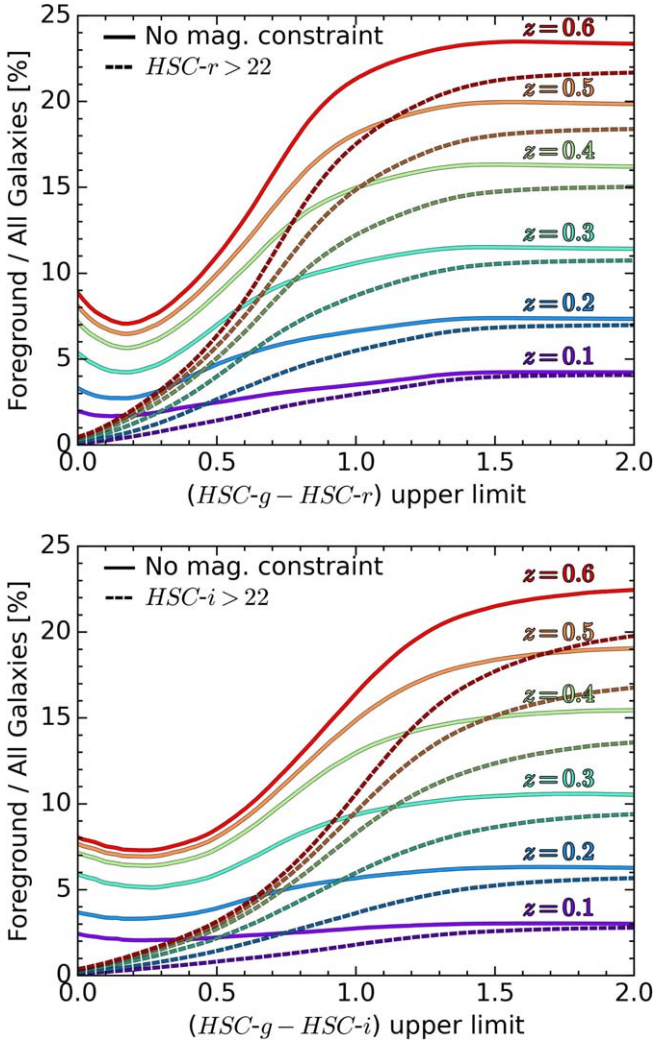

Figure 6. Foreground contamination percentage as a function of upper-limit color constraint from the photometry and redshifts of the COSMOS2020 catalog (J. R. Weaver et al. 2022). The rainbow color gradient signifies curves of a range of redshifts that demarcate foreground and background galaxies (i.e., a cluster redshift). Light, solid curves are for all galaxies, and dark, dashed curves are for HSC-r > 22 (top) and HSC-i > 22 (bottom) galaxies. The combination of a magnitude and color constraint are effective at removing contamination by foreground galaxies.

flatten, which indicates that contamination has reached its maximum. The maximum contamination by foreground galaxies ranges from ∼2.5% at a lens (cluster) redshift of $z_{\rm lens} = 0.1$ to ∼22.5% at $z_{\rm lens} = 0.6$. Applying a bluer color constraint reduces the contamination by foreground galaxies, and the reduction is more effective for higher-redshift clusters. Including a magnitude constraint (dark, dashed curves) provides a greater reduction in the contamination.

The contamination by cluster galaxies can be estimated from the source catalogs by investigating the cluster-centric number density of galaxies. It is expected that the inclusion of cluster galaxies into the source catalog will lead to more source galaxies near the cluster center than in the outskirts. In Table 2, we quantify the number density ratio ($n_{\rm in}/n_{\rm out}$) of source galaxies within 750 kpc to those in the range of 750–1500 kpc. Since these merging systems are composed of multiple subclusters, we choose a general radius of 750 kpc to separate the inner to outer regions. We find that contamination levels

from the number density ratios are consistent with random scatter about unity for a χ^2 test. In addition, we verified that the radial number density of source galaxies for each cluster is close to a flat relation. Therefore, the dilution effect from the levels of contamination that occur when selecting source galaxies in color–magnitude space is subdominant to the statistical errors in the analysis (M. J. Jee et al. 2014, 2017). Additional motivation for our choice of color–magnitude over color–color selection is that most of the clusters in this study have sufficiently deep imaging in only two bands. Additionally, using two different selection methods would introduce a new systematic into our study.

In addition to these magnitude and color selection criteria, we constrain the background source catalog by our ability to measure their shapes. We ensure that spurious objects that are too small to be lensed galaxies are removed by constraining the semiminor axis to be greater than 0.3 pixels. Highly elongated objects are rejected by forcing the measured ellipticity to be <0.9. We require the ellipticity error to be <0.3. Finally, only "well-fit" objects from the MPFIT fitter are kept (MPFIT status of 1).

These constraints lead to a robust source catalog that carefully balances the purity and number density of the source (lensed) galaxy catalog. The source densities for each cluster are summarized in Table 2. The average source density is 25 arcmin^{-2}.

3.5. Redshift Estimation

In a WL analysis, each source galaxy provides a probe of the projected galaxy cluster potential. As is apparent in Equation (3), the effectiveness of the gravitational lens varies on a source-by-source basis with the lensing efficiency ratio, β. Unfortunately, distances to each of the source galaxies in our sample are unavailable. To remedy this, we rely on the photometric redshift catalog (T. Dahlen et al. 2010) of the GOODS-S field as a reference for our source galaxy catalog. A version of the GOODS-S catalog that is modeled to represent the source catalog is used to quantify the effective redshift of the source catalog by the method described below. This technique is common in WL studies that do not have the luxury of redshifts for each source galaxy (to name a few; M. J. Jee et al. 2011; N. Okabe & G. P. Smith 2016; T. Schrabback et al. 2018).

The GOODS-S reference catalog is constrained with the same color and magnitude criteria that are applied when selecting the source galaxies. Figure 7 shows the galaxy number density of the constrained GOODS-S catalog and the A2061 source catalog. The GOODS-S observations are much deeper than the Subaru observations and probe to much fainter magnitudes. To alleviate the difference in depth, the constrained GOODS-S catalog is weighted by the number density ratio for each bin. From the constrained and weighted GOODS-S catalog, an effective β for the source galaxies of the Subaru imaging is then inferred. The effective β is calculated as follows:

$$\langle\beta\rangle = \left\langle \max\left(0, \frac{D_{ls}}{D_s}\right)\right\rangle, \tag{13}$$

where D_{ls} and D_s are the angular diameter distances from lens to source and observer to source, respectively. These distances are derived from the photometric redshifts. The maximum

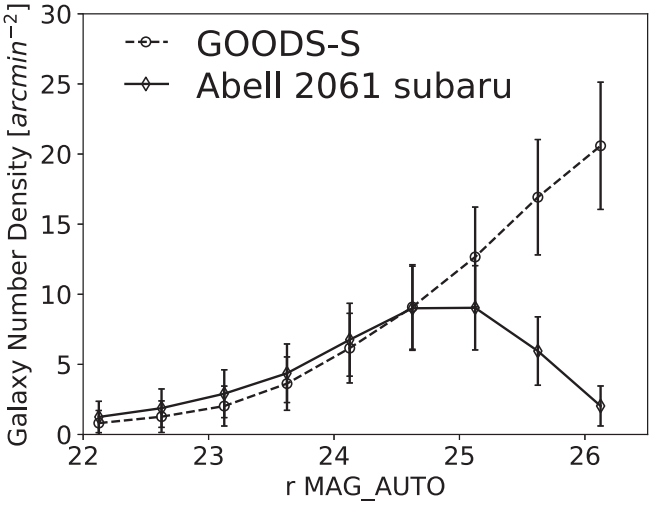

Figure 7. Galaxy number density by magnitude for the constrained (by color) GOODS-S reference catalog and A2061 source galaxy catalog. The GOODS-S observations are much deeper, which gives rise to the large difference in source density at faint magnitudes. To make up for the difference in depth, the GOODS-S catalog is weighted by the ratio of the bins when used as a reference catalog.

function is needed because sources that are foreground are not lensed. The $\langle\beta\rangle$ values for each cluster are tabulated in Table 2. Since the source galaxies are represented by a single $\langle\beta\rangle$, a first-order correction (C. Seitz & P. Schneider 1997)

$$g' = \left[1 + \left(\frac{\langle\beta^2\rangle}{\langle\beta\rangle^2} - 1\right)\kappa\right] g \tag{14}$$

is applied to the reduced shear to take the width of the distribution into consideration. Foregoing this correction can lead to an overestimation of cluster masses (e.g., H. Hoekstra et al. 2000).

3.6. Convergence Reconstruction

In Section 3.1, the basic inversion method for convergence reconstruction was introduced. The simplest method to recover the convergence is to average galaxy shapes in spatial bins across the field of view of the cluster. The spatial averaging of galaxy shapes produces a map of the reduced shear. Then, by the convolution of Equation (5), the convergence distribution can be recovered. This convolution method is prone to edge effects that can artificially increase the lensing signal near the edge of the image. In this work, we utilize a code called `FIATMAP` (D. Wittman et al. 2006, 2023; R. Stancioli et al. 2024) that performs a convolution of the observed shear field with a kernel

$$\left(1 - \exp\left[\frac{-r^2}{2r_i^2}\right]\right) r^{-2} \exp\left[\frac{-r^2}{2r_o^2}\right], \tag{15}$$

where r_i and r_o are the inner and outer radii of the filter. The inner radius cutoff prevents extreme statistical fluctuations from affecting the measurement, and the outer radius cutoff suppresses noise. We set the inner and outer radii to 200″ and 400″, respectively. The resulting mass maps have a pixel scale that ranges from approximately 5″ at the lowest redshift to 7″ at the highest.

For each cluster, we present contours that represent S/N of convergence. To measure the noise level of the map, 1000 realizations of the mass map are generated by bootstrap resampling the source catalog and producing maps through the same convergence reconstruction procedure. From the 1000 realizations, the rms noise is measured. The S/N map is then calculated by dividing the original convergence map by the rms map.

3.7. Substructure Identification

One of the goals of this study is to identify the merging subclusters that may be responsible for the formation of radio relics. For all of the clusters in this study, multiple peaks in the WL maps are expected. However, not all of these peaks should be taken as merging subclusters (substructures).

In order to identify the real WL peaks from the statistical fluctuations, we utilize the multiwavelength data. Significant subclusters are expected to be massive enough to emit brightly in X-rays. Furthermore, they are expected to have bright cluster galaxies in the vicinity of their WL peaks. Therefore, we will identify subclusters as those with significant WL peaks ($S/N \gtrsim 3$) and nearby galaxy overdensities or X-ray brightness peaks.

3.8. Mass Estimation

There are multiple methods to estimate the mass of a galaxy cluster. One method is to use a proxy for the mass and calibrate it with a robust mass estimate. These methods are called mass-scaling relations and rely on the emission from the gas and stars as a tracer of the cluster potential. The mass–richness relation is a commonly used scaling relation, which positively correlates the number of cluster galaxies to the total mass of the system (e.g., R. Murata et al. 2019). Other scaling relations utilize the X-ray emission or the Sunyaev–Zel'dovich (SZ; R. A. Sunyaev & Y. B. Zeldovich 1972) effect from the gas to estimate the mass (e.g., C. Ge et al. 2019). The galaxies and gas can also provide a mass estimate directly by assuming that they are in hydrostatic equilibrium (HSE). With that assumption, the gravitational potential can be equated to the outward pressure force of the gas. In this work, we derive mass from the galaxy velocity dispersion measurements presented in G19 by applying the scaling relation from A. E. Evrard et al. (2008):

$$M_{200} = \left(\frac{\sigma_{\rm DM}}{\sigma_{\rm DM,15}}\right)^{1/\alpha} 10^{15}\, M_{\odot}, \tag{16}$$

where $\sigma_{\rm DM,15} = 1082 \pm 4\,{\rm km\,s^{-1}}$ and $\alpha = 0.3361 \pm 0.0026$ are derived from cosmological simulations.

The validity of applying HSE when estimating the mass of a galaxy cluster has been questioned. D. Suto et al. (2013), and more recently V. Biffi et al. (2016), found that the HSE assumption for clusters in cosmological simulations had mass estimates that departed from the true cluster mass by as much as 30%. As expected, these studies found that the disturbed systems show the largest deviations from HSE.

Mass estimates based on the WL signal from galaxy clusters do not require an HSE assumption. Furthermore, the WL signal is caused by the complete mass (gravitational potential) of the cluster, which is predominantly dark matter. Thus, WL should be a more accurate probe of the mass of merging systems. However, there are recent investigations into the bias of fitting Navarro–Frenk–White (NFW; J. F. Navarro et al. 1997) models to the WL signal of merging galaxy clusters that suggest that mass estimates may be biased at certain stages of the cluster merger process (W. Lee et al. 2023).

3.8.1. Multiple Halo Mass Estimation

The clusters that are analyzed in this paper contain multiple substructures. Hence, it would be improper to model them as a single object. Instead, we fit a multihalo NFW model to the observed data to estimate the masses of each subcluster simultaneously. The fit is accomplished by predicting the reduced shear at every source galaxy position and then calculating the χ^2 between the observed galaxy ellipticity and modeled shear

$$\chi^2 = \sum_{i,j}\left(\frac{e_{i,j} - g_{i,j}}{\sigma_{i,j}}\right)^2 \tag{17}$$

where i is summed over each galaxy, and j is summed over the two components of the shear (ellipticity). In this equation, $\sigma_{i,j} = (\delta e_{i,j}^2 + \sigma_{\rm SN}^2)^{-0.5}$ is the ellipticity measurement uncertainty $\delta e_{i,j}$ and the shape noise $\sigma_{\rm SN}^2$ added in quadrature. We fix the shape noise to $\sigma_{\rm SN} = 0.25$. The reduced shear at the position of a galaxy is modeled following the NFW equations from C. O. Wright & T. G. Brainerd (2000). The χ^2 is minimized with the optimization code, MPFIT, and the resulting masses and their uncertainties are fit.

In this analysis, we use two different methods to constrain the mass with the NFW profile. The first method utilizes a concentration–mass (c–M) relation. Relations for c–M are typically found from cosmological simulations that can cover a wide range of redshifts and cluster masses. One of the more common c–M relations that is applied in WL studies is that of A. R. Duffy et al. (2008). Their c–M relation is derived from `Gadget2` simulations with a box size of 400 Mpc and is as follows:

$$M_{200} = 2(1+z)^{-B/A}\left(\frac{c}{5.71 \pm 0.12}\right)^{1/A} 10^{14}\, M_{\odot}, \tag{18}$$

where $A = -0.084 \pm 0.006$ and $B = -0.47 \pm 0.04$ for clusters in a redshift range of $0 < z < 2$. However, c–M relations are subject to the limitations of the simulations that they are derived from, such as the limited box size and cosmology imprinted on the initial conditions. These limitations manifest a variety of c–M relations (e.g., A. R. Duffy et al. 2008; A. A. Dutton & A. V. Macciò 2014; B. Diemer & M. Joyce 2019). For our study, we elect to use the A. R. Duffy et al. (2008) relation because it has been commonly applied in past WL studies and will ease comparison.

An alternative to using a c–M relation is to fit both concentration and mass. We will refer to this method as 2PNFW (for two parameters) from here on. However, there is a degeneracy between the concentration and mass that prevents this technique from converging for clusters that have low WL signal (K. Finner et al. 2017). Therefore, we sample the c–M parameter space with Markov Chain Monte Carlo (MCMC). We confine the MCMC to uniform priors that sufficiently cover the typical range of the mass ($10^{13}\, M_{\odot} < M_{200} < 10^{16}\, M_{\odot}$) and concentration ($1 < c < 9$) for galaxy clusters. Masses are determined from the highest likelihood returned from Equation (17). In most cases, the uncertainty on the

concentration for this method is large, and therefore we choose not to present their values. However, we marginalize over the concentration to propagate its uncertainty to the mass.

In both of these methods, multiple halos are simultaneously fit to the WL signal. The location of the halo centers must be chosen carefully. We choose to fix each halo to its mass peak's corresponding brightest cluster galaxy (BCG). The BCG is not necessarily the center of the cluster, but on average it is a good tracer of the cluster potential centroid (A. Zitrin et al. 2012) and is well defined. Another good choice is the WL-derived mass peak, but there is a large positional uncertainty associated with it for low-S/N WL results. In many of these merging cluster cases, the X-ray peak would be a poor choice for the center because recent merging activity can cause a significant departure of the gas from the dark matter density peak.

It has been shown that miscentering can lead to biases of up to 10% in WL mass estimates (M. R. Becker & A. V. Kravtsov 2011; M. Oguri & T. Hamana 2011; B. E. Lee et al. 2018). M. W. Sommer et al. (2022) investigated the impact of miscentering with c–M relations and showed that miscentering bias is sensitive to the c–M relation and cluster mass. More recently, M. W. Sommer et al. (2024) showed that mass estimates can be biased high by 2%–6% when using the ICM-based center. These estimates give an idea of the bias of miscentering but cannot be directly applied to our method because we are fitting multiple NFW halos to the clusters. To mitigate the effects of miscentering, following the methods of previous WL studies (e.g., D. E. Johnston et al. 2007; K. Umetsu et al. 2014), we do not use source galaxies that are within 200 kpc of the centroid of each halo when fitting the NFW models. This precaution serves two purposes. First, it mitigates the effects of miscentering, which are most sensitive near the center of the cluster potential. Also, it bypasses regions that are subject to dilution by the cluster galaxies (e.g., T. Broadhurst et al. 2005; E. Medezinski et al. 2010; K. Umetsu et al. 2014). The dilution comes from the unlensed foreground and cluster galaxies that are mistakenly included into the source catalog. In Section 3.4, we demonstrated that the radial number density of galaxies for the clusters is relatively flat, which suggests that dilution by cluster galaxies is minimal.

4. Weak-lensing Mass Distributions

In this section, the WL analysis of 29 radio relic merging galaxy clusters is presented and discussed. A summary of the literature on these merging clusters is presented in G19. For this reason, we will try not to repeat the work of G19 but will describe the relevant merging features, summarize previous WL results, and present/compare our new WL results. Our goal is to provide new insight into the merging systems with the mapping of the dark matter.

For each cluster, we present a four-panel figure. The top-left panel is the WL mass map S/N contours plotted over the Subaru color image. Contours start at S/N = 2σ and increase in intervals of S/N = 1σ unless otherwise noted in the figure caption. These WL mass maps are available upon request to the authors. We indicate each of the significant subclusters (S/N $\gtrsim$ 3) with a blue, dashed circle that is centered on the BCG that we have assigned to the subcluster. The radius of the circles is chosen to be R_{3000} because it fits elegantly into the field of view, where $\Delta = 3000$ is the density contrast. Each R_{3000} is derived from the mass estimates following the masses of the c–M relation fits in Table 4. The top-right panel shows the WL contours over the X-ray imaging with radio contours (green). The bottom-left and bottom-right panels have the WL contours plotted over the galaxy luminosity and number density maps, respectively, where these galaxies were selected following the method in Section 3.4. The Gaussian smoothing kernels applied to the density maps are presented in the bottom-right corner.

Table 4 contains the mass estimates for all of the subclusters that we identified as securely detected. As mentioned, WL mass estimates are done via the 2PNFW method with c and M as free parameters and via the c–M relation of A. R. Duffy et al. (2008). In addition, the velocity dispersion measurements from G19 are included in the table. The assignment of velocity dispersion measurements to WL peaks was done as follows. First, we identified the standout bright cluster galaxies in the vicinity of each WL peak and assigned the brightest one as the local BCG. We then found the subcluster that G19 had assigned that local BCG to and matched the WL-defined and GMM-defined subclusters. The similar spatial distribution of the G19 subclusters and our WL subclusters made matching straightforward. In cases where G19 were unable to identify subclusters (for example PSZ1G108), we assigned the velocity dispersion measurement to the primary subcluster (the more massive from the WL mass estimate).

4.1. 1RXS J0603.3+4212 (z = 0.226)

1RXSJ0603, also known as the Toothbrush cluster, is a well-studied merging cluster because of its 2 Mpc radio relic that resembles a toothbrush (R. J. van Weeren et al. 2012b, 2016; A. Stroe et al. 2016; K. Rajpurohit et al. 2018, 2020; F. de Gasperin et al. 2020). The morphology of the relic was reproduced in hydrodynamic simulations (M. Brüggen et al. 2012). R. J. van Weeren et al. (2016) suggested that reacceleration is occurring at the Toothbrush relic and simulations agreed that reacceleration is likely (H. Kang 2016a; H. Kang et al. 2017). Radio measured Mach numbers for the Toothbrush relic range from 2.8–4.6 (R. J. van Weeren et al. 2012b, 2016; K. Rajpurohit et al. 2018).

The X-ray emission has an elongated morphology that stretches approximately 1.5 Mpc in a north–south direction with the radio relic lying to its north. The southern region of the X-ray emission has sharp edges that resemble ram pressure stripping from a bullet-like core. G. A. Ogrean et al. (2013b) identified two distinct subclusters in the X-ray emission and provided evidence for three shocks with Mach numbers <2. M. Itahana et al. (2015) measured the Mach number in the north shock to be ∼1.5.

A WL analysis of Subaru and HST imaging is presented in M. J. Jee et al. (2016). Their study detected four substructures of which two were deemed significant and referred to as subclusters. These two subclusters are located at the BCGs in the north and south and are likely the subclusters that collided to create the radio relic. G19 identified four subclusters from galaxy redshifts with the two having the largest velocity dispersion corresponding to the most significant WL detections. M. J. Jee et al. (2016) assumed the A. R. Duffy et al. (2008) c–M relation and estimated the mass of the northern and southern subclusters as $M_{200} = 6.3^{+2.2}_{-1.6} \times 10^{14}\,M_{\odot}$ and $M_{200} = 2.0^{+1.2}_{-0.7} \times 10^{14}\,M_{\odot}$, respectively.

WL result. Our WL analysis is done on solely the Subaru imaging (Figure 8). We detect the two primary subclusters that

Table 4
WL Subcluster Mass Estimates

Cluster	Index	Duffy M_{200} ($10^{14}M_{\odot}$)	2PNFW M_{200} ($10^{14}M_{\odot}$)	σ_v (km s^{-1})	WL Peak S/N
1RXSJ0603 N	A	6.2 ± 1.2	$12.9^{+3.3}_{-3.1}$	925 ± 51	4.5
1RXSJ0603 S	A	2.8 ± 0.8	$1.9^{+1.0}_{-0.6}$	763 ± 100	4.2
A115 N	B	1.4 ± 0.5	$1.0^{+0.5}_{-0.3}$	1056 ± 60	3.8
A115 S	B	3.0 ± 0.8	$3.3^{+1.4}_{-1.0}$	1108 ± 70	3.7
A521 C	C	3.5 ± 0.9	$5.9^{+2.4}_{-1.9}$	990 ± 85	4.6
A521 NW	C	1.1 ± 0.5	$0.5^{+0.6}_{-0.2}$	⋯	3.6
A521 SE	C	2.5 ± 0.7	$1.9^{+1.2}_{-0.8}$	735 ± 67	3.8
A523 N	D	2.7 ± 0.9	$2.2^{+1.7}_{-1.0}$	814 ± 60	4.6
A523 S	D	1.6 ± 0.7	$1.8^{+1.8}_{-0.9}$	673 ± 53	3.6
A746 S	E	2.0 ± 0.8	$3.1^{+1.9}_{-1.8}$	1094 ± 95	4.6
A746 N	E	2.1 ± 0.8	$1.5^{+1.5}_{-1.1}$	⋯	3.6
A746 W	E	1.7 ± 0.7	$0.8^{+1.1}_{-0.5}$	⋯	3.6
A781[a] East	F	3.3 ± 0.8	$2.8^{+1.6}_{-1.0}$	⋯	3.8
A781 Middle	F	4.2 ± 0.9	$5.0^{+2.9}_{-1.8}$	821 ± 65	4.6
A781 Main	F	3.5 ± 0.8	$4.0^{+2.0}_{-1.4}$	830 ± 54	4.2
A781[a] North	F	1.7 ± 0.6	$1.5^{+1.2}_{-0.6}$	⋯	3.3
A1240 N	G	2.6 ± 0.6	$3.3^{+0.9}_{-1.1}$	706 ± 52	7.6
A1240 S	G	1.1 ± 0.4	$0.8^{+0.5}_{-0.5}$	727 ± 68	3.3
A1300 S	H	11.0 ± 1.8	$12.8^{+2.7}_{-1.3}$	1205 ± 51	5.3
A1612 E	I	4.0 ± 1.0	$6.6^{+2.9}_{-2.0}$	826 ± 83	3.3
A1612 W	I	1.8 ± 0.7	$1.0^{+0.8}_{-0.5}$	662 ± 118	3.0
A2034 N	J	1.1 ± 0.4	$0.9^{+0.4}_{-0.4}$	815 ± 94	5.1
A2034 S	J	2.6 ± 0.7	$2.0^{+1.2}_{-0.7}$	726 ± 57	7.0
A2034 SE	J	0.6 ± 0.3	$1.0^{+1.0}_{-0.5}$	366 ± 55	7.0
A2061 N	K	2.0 ± 0.6	$3.1^{+1.8}_{-1.3}$	841 ± 54	3.7
A2061 S	K	1.6 ± 0.5	$1.1^{+0.6}_{-0.4}$	⋯	4.0
A2163[a] N	L	1.1 ± 0.7	$0.8^{+0.6}_{-0.5}$	952 ± 92	3.6
A2163 E	L	9.2 ± 1.8	$9.0^{+2.3}_{-2.8}$	1389 ± 75	5.2
A2163 W	L	0.8 ± 0.6	$0.5^{+0.5}_{-0.3}$	741 ± 75	3.0
A2255 E	M	1.3 ± 0.6	$1.1^{+0.8}_{-0.5}$	⋯	4.1
A2255 W	M	4.7 ± 1.1	$5.1^{+3.2}_{-1.9}$	988 ± 36	5.3
A2345[a] E	N	4.7 ± 1.2	$5.0^{+1.3}_{-1.0}$	1065 ± 67	3.7
A2345 C	N	3.2 ± 1.0	$3.3^{+2.3}_{-1.5}$	1065 ± 67	3.8
A2345 W	N	2.1 ± 0.8	$1.6^{+1.6}_{-0.8}$	⋯	3.2
A2744 E	O	7.2 ± 1.8	$8.5^{+2.5}_{-2.5}$	772 ± 52	6.6
A2744 W	O	6.6 ± 2.3	$3.2^{+2.2}_{-1.5}$	678 ± 82	6.0
A2744 N	O	1.0 ± 0.8	$1.9^{+1.9}_{-1.0}$	1154 ± 70	3.0
A2744 S	O	0.6 ± 0.6	$0.8^{+0.6}_{-0.5}$	666 ± 52	3.6
A3411 W	P	2.3 ± 1.0	$3.9^{+3.9}_{-1.9}$	1204 ± 84	3.1
A3411 E	P	1.8 ± 1.0	$1.0^{+1.3}_{-0.6}$	⋯	3.3
A3412[a]	P	1.1 ± 0.8	$0.8^{+1.2}_{-0.5}$	1199 ± 82	2.8
CIZAJ2242 N	Q	8.2 ± 1.8	$12.3^{+3.9}_{-3.0}$	1102 ± 69	4.7
CIZAJ2242 S	Q	9.3 ± 1.8	$15.8^{+4.6}_{-3.5}$	1146 ± 88	5.4
MACSJ1149 C	R	16.4 ± 3.1	$13.5^{+3.5}_{-2.8}$	1295 ± 62	4.1
MACSJ1752 NE	S	5.6 ± 1.8	$5.5^{+1.9}_{-1.4}$	1006 ± 68	7.3
MACSJ1752 SW	S	5.6 ± 1.7	$5.1^{+2.0}_{-1.5}$	1038 ± 77	5.2
PLCKG287 SE	T	1.7 ± 0.7	$1.0^{+0.7}_{-0.6}$	680 ± 87	3.3
PLCKG287 C	T	20.4 ± 1.9	$20.0^{+2.4}_{-2.2}$	1373 ± 72	9.0
PLCKG287 NW	T	1.4 ± 0.7	$1.0^{+0.7}_{-0.5}$	⋯	3.0
PSZ1G108 M	U	6.9 ± 2.1	$7.6^{+2.5}_{-2.5}$	873 ± 90	5.2
PSZ1G108 NE	U	1.5 ± 1.2	$1.4^{+1.2}_{-0.8}$	⋯	3.0
RXCJ1314 E	V	2.3 ± 1.0	$3.9^{+2.1}_{-1.9}$	799 ± 73	3.3
RXCJ1314 W	V	4.2 ± 1.3	$2.5^{+1.2}_{-0.8}$	845 ± 99	4.5
ZwCl0008 E	W	2.9 ± 0.8	$2.8^{+1.5}_{-1.0}$	757 ± 62	4.2
ZwCl0008 W	W	2.7 ± 0.8	$2.8^{+1.5}_{-1.0}$	681 ± 66	3.8
ZwCl1447 N	X	2.7 ± 0.8	$2.0^{+1.8}_{-0.9}$	1147 ± 63	5.1
ZwCl1447 S	X	1.0 ± 0.5	$1.2^{+2.2}_{-0.8}$	⋯	4.8

Table 4
(Continued)

Cluster	Index	Duffy M_{200} ($10^{14}M_{\odot}$)	2PNFW M_{200} ($10^{14}M_{\odot}$)	σ_v (km s^{-1})	WL Peak S/N
ZwCl1447[a]	X	2.2 ± 0.7	$1.7^{+1.0}_{-0.6}$	⋯	4.9
ZwCl1856 N	Y	1.6 ± 0.8	$1.2^{+0.5}_{-0.5}$	934 ± 117	4.4
ZwCl1856 S	Y	1.5 ± 0.7	$1.0^{+0.4}_{-0.7}$	862 ± 133	4.2
ZwCl2341 NW	Z	0.8 ± 0.6	$0.6^{+0.7}_{-0.3}$	359 ± 39	3.0
ZwCl2341 C	Z	3.1 ± 1.2	$3.0^{+2.3}_{-1.3}$	⋯	4.1
ZwCl2341 S	Z	1.3 ± 0.7	$1.1^{+1.4}_{-0.6}$	801 ± 46	2.7

Notes. 68% uncertainties reported.
[a] Denotes subclusters that are not involved in the merger.

are presented in M. J. Jee et al. (2016). In addition, two other substructures from M. J. Jee et al. (2016) are detected as an elongation from the northern mass peak and a separate peak directly to its south. We estimate the mass of the subclusters to be $M_{200,N} = 6.2 \pm 1.2 \times 10^{14}\,M_{\odot}$ and $M_{200,S} = 2.8 \pm 0.8 \times 10^{14}\,M_{\odot}$, which are consistent with the M. J. Jee et al. (2016) result.

Merger insight. As is apparent from the offset between the mass peak (or BCG) and the X-ray emission in the south of the cluster, the Toothbrush cluster is a dissociative merger. The alignment of the radio relic and the elongated X-ray and WL distributions suggest that the northern and southern subclusters collided to form the shock. The ram-pressure-stripped morphology of the X-ray emission is expected when the impact parameter is small. The Toothbrush cluster is a strong candidate to constrain the properties of dark matter because of the large separation of the mass peak from the X-ray peak but the candidate subclusters may complicate the merging scenario.

4.2. A115 (z = 0.193)

A115 is a single radio relic cluster with double X-ray peaks (T. C. Beers et al. 1983; L. Feretti et al. 1984). It stands out from the rest of the merging clusters because both subclusters appear to have ram-pressure-stripped gas trailing behind cool cores, but the stripped gas does not align with the axis that the radio relic (shock) appears to be moving. Since the cluster has a unique X-ray distribution, it has been the subject of quite a few studies. R. Shibata et al. (1999) presented evidence that A115 is a merging cluster with temperature variations measured by the Advanced Satellite for Cosmology and Astrophysics. The dynamical analysis of R. Barrena et al. (2007) identified two structures in the galaxy distribution. A. Botteon et al. (2016) detected a shock in Chandra observations that is cospatial with the radio relic and determined the Mach number to be 1.7 ± 0.1. A hot region was found between the subclusters in the X-ray temperature analysis of E. J. Hallman et al. (2018). From Very Large Array (VLA) and Giant Metrewave Radio Telescope (GMRT) observations, they calculated the radio Mach number to be 2.1.

N. Okabe et al. (2010) included A115 in their WL analysis of 30 galaxy clusters, LoCuSS. Their WL mass map revealed two peaks. For the northern subcluster, a ∼300 kpc offset of the mass peak from the BCG is shown but with no statistical significance. H. Hoekstra et al. (2012) estimated the mass of each subcluster and found them to be $M_{\rm vir,N} = 5.7^{+1.7}_{-1.9} \times 10^{14}\,M_{\odot}$ and $M_{\rm vir,S} = 6.8^{+2.1}_{-1.9} \times 10^{14}\,M_{\odot}$.

WL result. Our WL analysis (Figure 9), published in M. Kim et al. (2019), characterizes the cluster as a bimodal merger with both WL mass peaks consistent with their X-ray peak and BCG counterparts. The northern cluster is found to have $M_{200,\rm N} = 1.5 \pm 0.5 \times 10^{14}\,M_{\odot}$, and the southern cluster has $M_{200,\rm S} = 3.0 \pm 0.8 \times 10^{14}\,M_{\odot}$. These mass estimates are lower than the mass estimates from the literature, and M. Kim et al. (2019) presented a detailed comparison of them.

Merger insight. The BCG, X-ray brightness peaks, and mass peaks are cospatial for each of the subclusters. The biggest mystery in A115 is reconciling the ram-pressure-stripped tails seen in X-rays with the position of the radio relic. If one assumes that the tails are signifying the past direction of motion for the subclusters, it does not agree with an axial shock origin for the radio relic. Utilizing the WL measurements of M. Kim et al. (2019), idealized RAMSES simulations of a two-cluster collision with a relatively large impact parameter by W. Lee et al. (2020) concluded that the ram-pressure-stripped tails could be slingshot tails that have rotated relative to the original collision axis. Their simulations also reproduced the radio relic in the observed location. The large impact parameter of A115 sets it as a unique merger that exhibits a radio relic.

4.3. A521 (z = 0.247)

M. Arnaud et al. (2000) showed that the X-ray emission of A521 has an irregular morphology with two peaks that are separated by about 500 kpc. S. Maurogordato et al. (2000) measured the radial velocities of 41 cluster galaxies and calculated a velocity dispersion of 1386^{+206}_{-139} km s^{-1}. C. Ferrari et al. (2003) provided evidence for a merging system by showing that the line-of-sight (LOS) velocity of the galaxies departs from a single-Gaussian distribution. The X-ray emission detected by Chandra is elongated in a northwest to southeast direction with two major components (C. Ferrari et al. 2006). The radio relic is situated to the east of the cluster and elongates north to south (S. Giacintucci et al. 2006; D. Dallacasa et al. 2009). The cluster has a distinct cool core that is cospatial with the BCG and is compressed on its southern side (H. Bourdin et al. 2013). H. Bourdin et al. (2013) highlighted a bullet-like shape extending from the cool core, which may be further evidence of the ongoing merger. They detected a shock at the location of the radio relic in the XMM-Newton X-ray observation and found the Mach number to be 2.4. MeerKAT observations from the cluster legacy survey (K. Knowles et al. 2022) are presented in Figure 10. A second radio relic is found in the NW of the cluster that may be a counter relic to the bright relic in the east (artificially placed arc

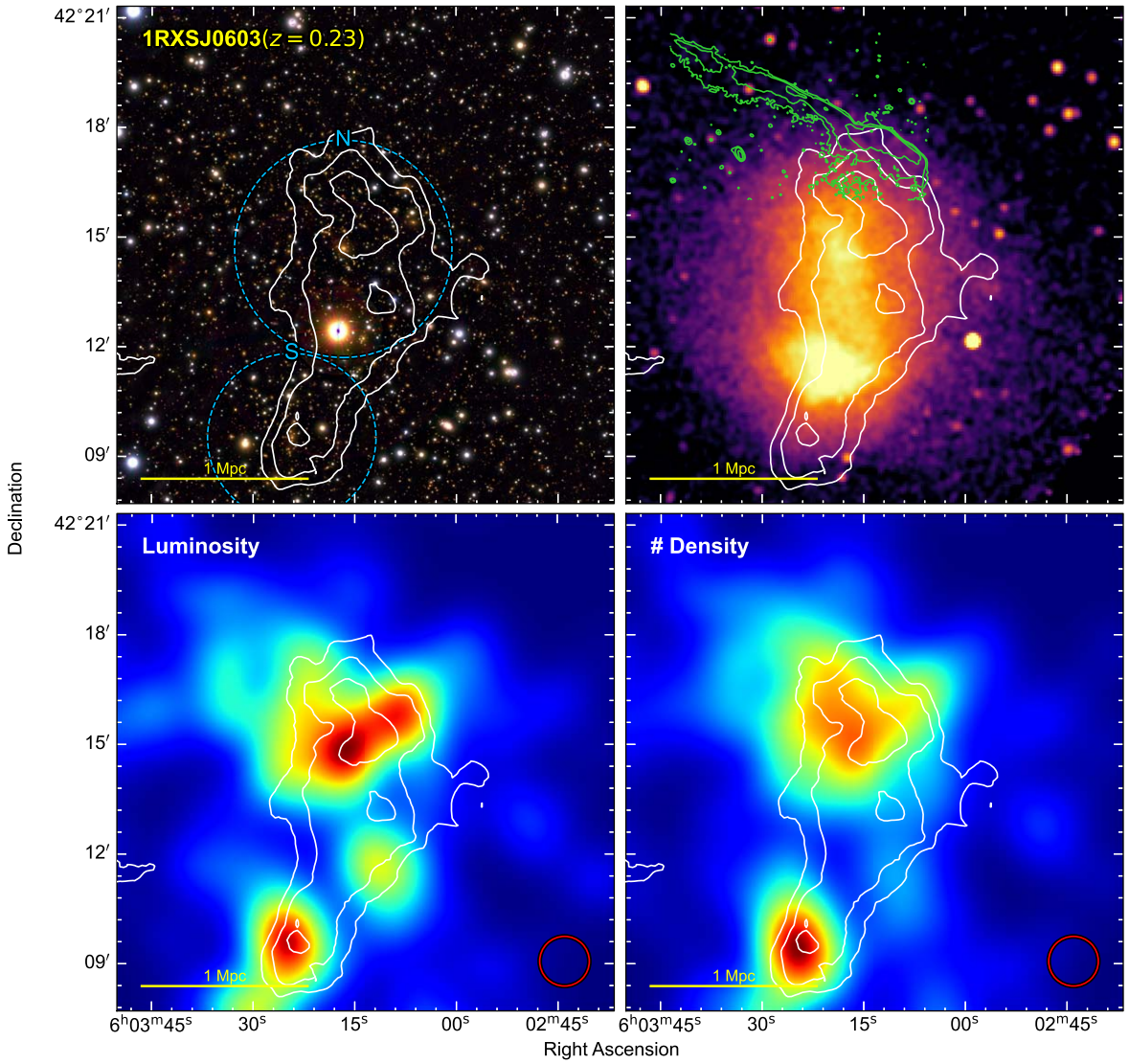

Figure 8. 1RXSJ0603. A dissociative merger with an extremely large radio relic. Top left: WL convergence S/N (white contours) of the Toothbrush cluster over Subaru color image. Contours start at 2σ and increase in intervals of 1σ. The dashed blue circles are centered on the local BCG of the subcluster and have a radius of R_{3000}. Top right: WL convergence S/N contours over X-ray emission with radio relic plotted as green contours. Bottom left: WL convergence S/N over galaxy luminosity density. Bottom right: WL convergence S/N over galaxy number density. The red circles in the galaxy panels are the FWHM of the Gaussian used to smooth the galaxy maps.

in Figure 10). The nature of the diffuse radio emission is investigated further in R. Santra et al. (2024).

A521 was mapped with WL in N. Okabe et al. (2010) and found to have a similar mass distribution as we present here. They reported a total mass for the system and do not analyze the individual subclusters. G19 mentioned that the galaxies of the cluster can be divided into three subclusters with the primary in the center, one to the northwest, and one to the southeast. However, their GMM does not separate the northwest from the central subcluster and results in two components.

WL result. Our work on A521 was published in M. Yoon et al. (2020). The WL signal has three peaks (Figure 10). The most significant peak is consistent with the BCG and X-ray peaks. In addition, WL peaks are found at the northwest BCG (second) and the southeast overdense galaxy region. Our mass estimates for the subclusters are $M_{200,\mathrm{C}} = \pm 0.9 \times 10^{14}\,M_{\odot}$, $M_{200,\mathrm{NW}} = 1.1 \pm 0.5 \times 10^{14}\,M_{\odot}$, and $M_{200,\mathrm{SE}} = 2.5 \pm 0.7 \times 10^{14}\,M_{\odot}$. We find that the total mass of the system is higher than the work of N. Okabe et al. (2010). The discrepancy is likely caused by the fitting of a single NFW halo to a complex merging system.

Merger insight. The elongation of the mass distribution is slightly rotated with respect to the X-ray emission, which gives it a better agreement with the morphology of the radio relics than the X-ray emission has. The separation of the two subclusters from the central subcluster does not provide clear evidence as to which subclusters collided to form the radio relics. Utilizing the wealth of information gained from the multiwavelength data, M. Yoon et al. (2020) tested merger scenarios with idealized simulations. Each tested merger scenario had its agreeing and disagreeing features with the observed features. The simulation showed that the subcluster that is now in the southeast could have approached from the north and collided with the central cluster with a large impact parameter to form the shock that is observed at the southeast radio relic position. That collision may have also caused the formation of the northwest radio relic. Alternatively, the radio relics could originate from two different collisions.

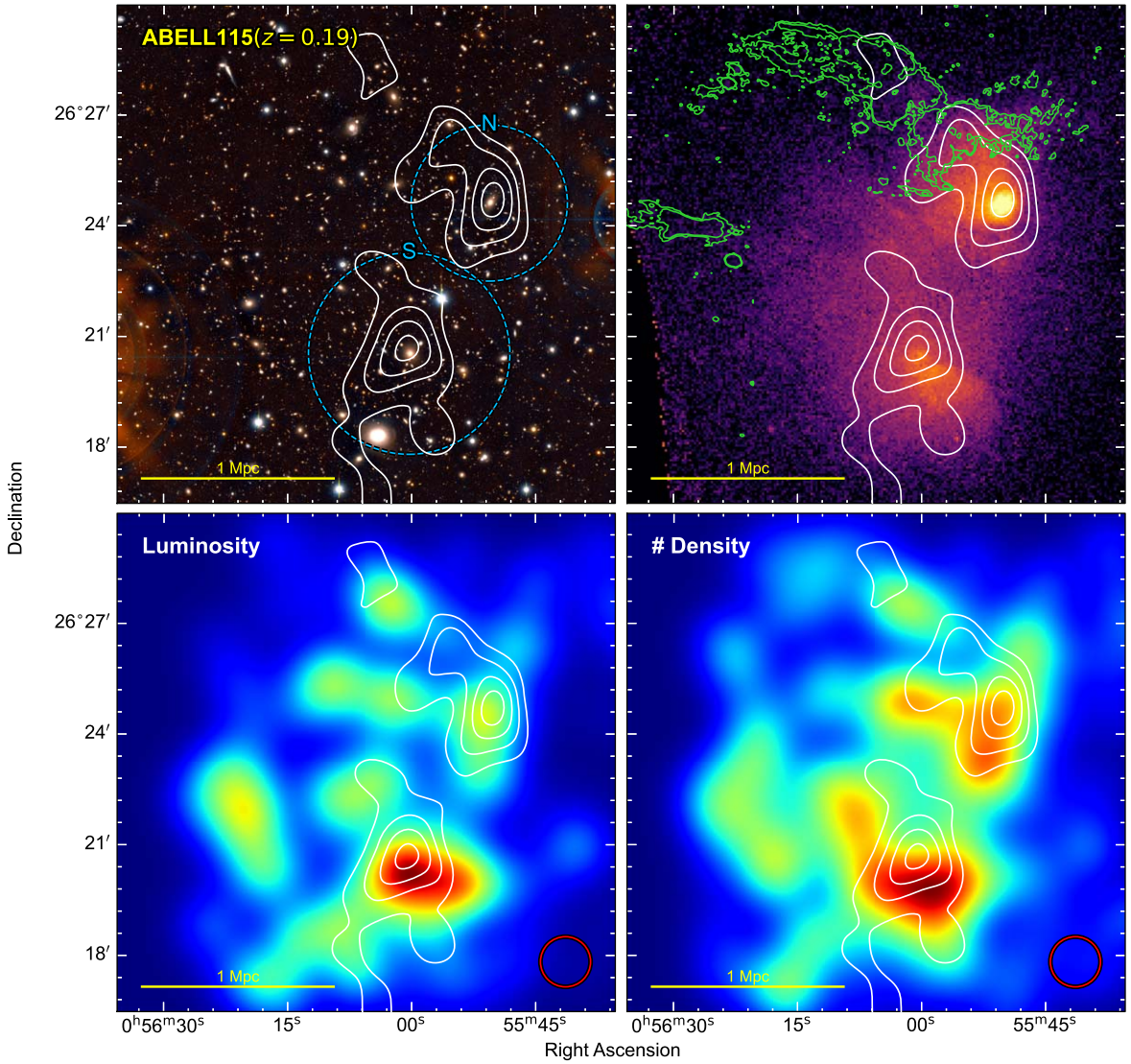

Figure 9. A115. A merger with peculiar ram-pressure-stripped gas that suggests a large impact parameter. WL contours increase in steps of 0.5σ.

4.4. A523 (z = 0.104)

A523 is a dissociative merger with the north ICM separated from the mass peak. M. Girardi et al. (2016) noted that there are two BCGs with the brightest in the north and second brightest in the south. In addition, they identified a galaxy overdensity directly west of the northern BCG and showed that two background structures straddle the cluster on the east and west. F. Cova et al. (2019) investigated the X-ray emission of the cluster with XMM-Newton and NuSTAR and detected a disturbed X-ray morphology, as well as the X-ray emission from the two background structures. Analyzing LOFAR and VLA observations of A523, V. Vacca et al. (2022a, 2022b) showed that the radio features are quite complex.

WL result. This is the first WL analysis of this cluster (Figure 11). Three mass clumps are detected from the Subaru imaging. The most significant detection is the north subcluster. The peak of the north subcluster is elongated north to south and encapsulates two bright cluster galaxies, of which the northern is brighter and elliptical, and the southern is bluer and disklike. The southern mass peak is situated to the south of the X-ray brightness peak and slightly north of the southern BCG. Our WL analysis also detects signal from the northwest (marked on Figure 11). However, we are unable to determine if this is a subcluster that belongs to A523 or to the western background structure. The WL detection is situated close to the western galaxy peak (M. Girardi et al. 2016) of A523, but the brightest galaxy in the region belongs to the background structure. A two-halo NFW fit with peaks in the north and south give masses of $M_{200,\mathrm{N}} = 2.7 \pm 0.9 \times 10^{14} M_{\odot}$ and $M_{200,\mathrm{S}} = 1.6 \pm 0.7 \times 10^{14} M_{\odot}$, respectively. If we include the northwest subcluster and assume it is at a redshift of 0.104, we find masses of $M_{200,\mathrm{N}} = 1.7 \pm 0.8 \times 10^{14} M_{\odot}$, $M_{200,\mathrm{S}} = 1.3 \pm 0.6 \times 10^{14} M_{\odot}$, and $M_{200,\mathrm{NW}} = 1.4 \pm 0.7 \times 10^{14} M_{\odot}$.

Merger insight. Since the X-ray emission is elongated in the north–south direction and the radio emission is perpendicular to that, we predict that a collision occurred between the northern and southern subclusters. The mass estimate shows that the clusters that collided have a mass ratio of approximately 2:1. It is interesting that the more massive cluster is in the north with the global BCG but the X-ray emission peak is closer to the southern subcluster. The luminosity and number density maps also show an inversion with the northern cluster being brighter but the southern having more galaxies. The offset of the mass

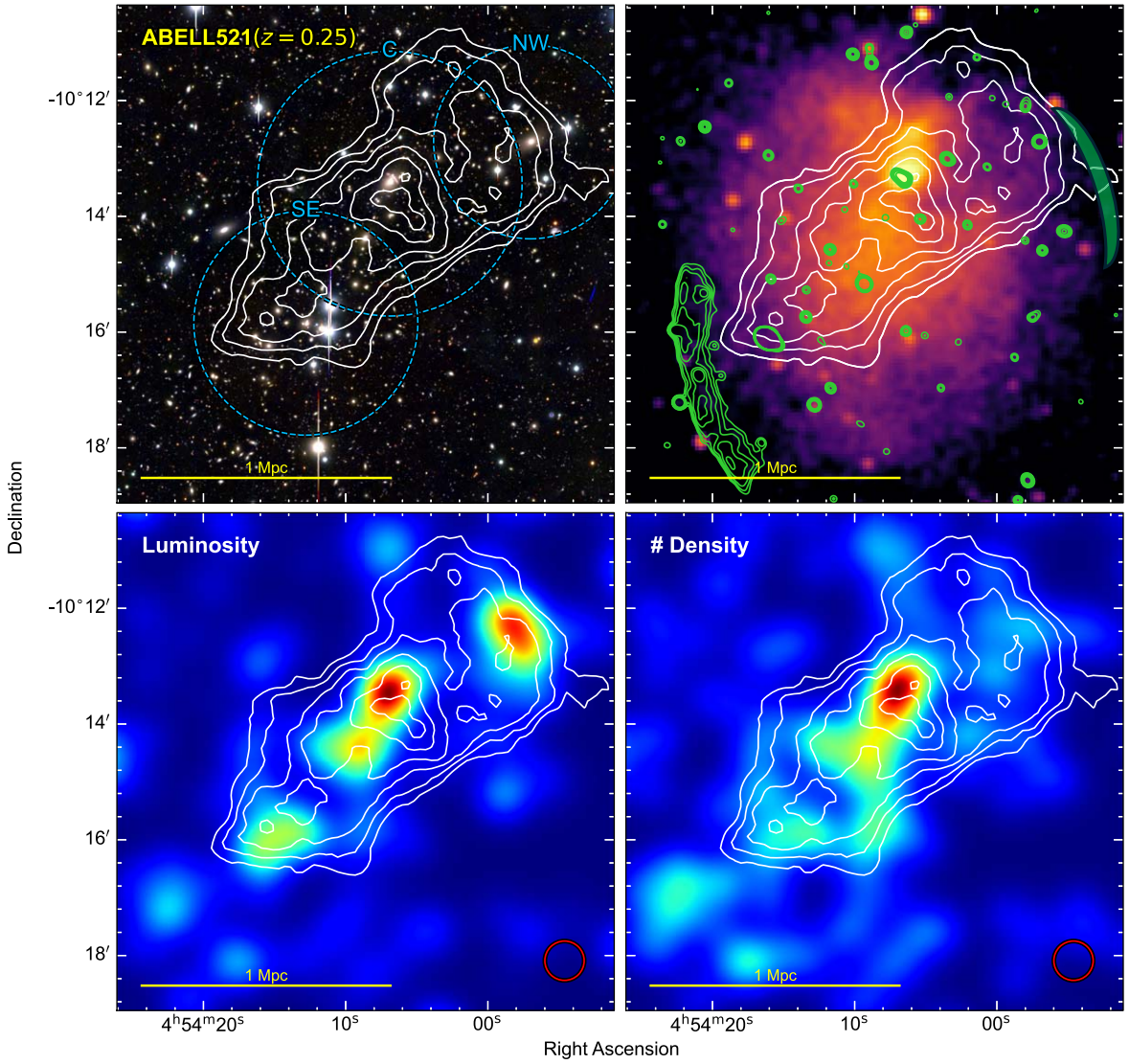

Figure 10. A521. A three-subcluster system with a cool core, a radio halo, and two radio relics. The NW radio relic is faint and marked with a green crescent. WL contours increase in steps of 0.5σ.

peaks and BCGs from the X-ray brightness peak presents A523 as a dissociative merger.

4.5. A746 (z = 0.214)

A746 is a complex system with double relics, two isolated relics, a candidate radio halo, and many X-ray features (K. Rajpurohit et al. 2024). The X-ray and radio analysis of K. Rajpurohit et al. (2024) detected three merger-driven shock fronts. They estimated that the southern region of the cluster has an average temperature of ∼9 keV and the northern has ∼4 keV. They show that the giant radio relic in the west has a filamentary emission.

WL result. The Subaru Suprime-Cam observations of A746 suffer from prominent ghosts from a nearby bright star. Subaru HSC observations were collected (PI: H. Cho) in 2022B with a careful planning to keep the bright star centered in the HSC field of view (for symmetry reasons) and with shorter exposure times per integration. The newly acquired HSC observations enabled a WL analysis that is presented in K. HyeongHan et al. (2024a). The WL analysis (Figure 12) shows a similar complexity to that found in the X-ray and radio emission. A dominant mass peak is found that coincides with the BCG and two less significant mass peaks are found to the west and north. K. HyeongHan et al. (2024a) found the total mass of the cluster is $M_{200} = 6.3 \pm 1.5 \times 10^{14} M_{\odot}$. We fit a three-halo model to the mass distribution and found masses of $M_{200,\mathrm{S}} = 2.0 \pm 0.8 \times 10^{14} M_{\odot}$, $M_{200,\mathrm{N}} = 2.1 \pm 0.8 \times 10^{14} M_{\odot}$, and $M_{200,\mathrm{W}} = 1.7 \pm 0.7 \times 10^{14} M_{\odot}$.

Merger insight. The complex features of A746 make it a difficult cluster to disentangle. The double relics suggest a merger in the west but X-ray emission and WL do not discern the two merger constituents. WL analysis with a telescope that can achieve a much higher number density of galaxies (i.e., HST, JWST, Euclid, or Roman) may provide details into this complex merging system.

4.6. A781 (z = 0.297)

A781 spans a large projected size on the sky (Figure 13). Here, we follow the naming scheme for clusters that was presented in N. Sehgal et al. (2008), S. Miyazaki et al. (2015), and D. Wittman et al. (2014). The field of view contains two subclusters that are at $z \sim 0.3$ (named Main and Middle), which

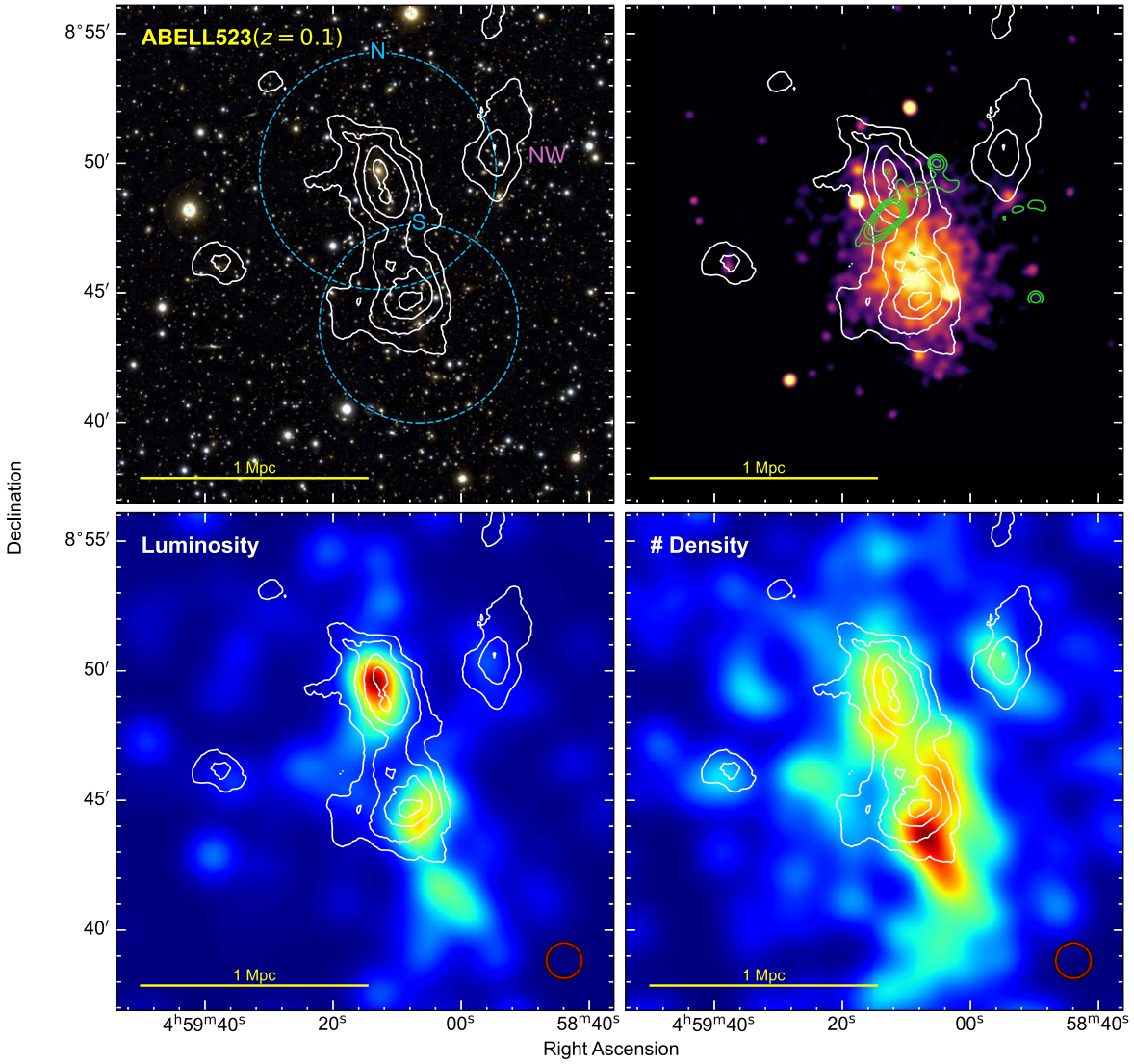

Figure 11. A523. A collision between two subclusters with radio emission in the middle. WL contours increase in steps of 0.5σ.

are flanked by subclusters at $z \sim 0.43$ called East and West (West is not shown in the figure). The candidate radio relic is situated between the Main and Middle subclusters (T. Venturi et al. 2008, 2011; F. Govoni et al. 2011). A. Botteon et al. (2019) performed an in-depth analysis of X-ray and radio observations and suggested that the radio relic may be a combination of a radio galaxy and a shock. However, the polarimetric study of B. Hugo et al. (2023) concluded that it is likely not a radio relic.

The cluster is within the field of view of the Deep Lens Survey (DLS; D. M. Wittman et al. 2002) and has many WL results (N. Sehgal et al. 2008; A. Abate et al. 2009; R. I. Cook & I. P. Dell'Antonio 2012; D. Wittman et al. 2014; S. Miyazaki et al. 2015). D. Wittman et al. (2014) detected the subclusters and determined their M_{200} masses to be $6.7^{+1.4}_{-1.3} \times 10^{14}\,M_{\odot}$, $4.3^{+1.6}_{-1.2} \times 10^{14}\,M_{\odot}$, and $2.8^{+1.9}_{-1.2} \times 10^{14}\,M_{\odot}$ for the Main, Middle, and East subclusters, respectively. R. I. Cook & I. P. Dell'Antonio (2012) detected the East, Main, and Middle subclusters but were unable to detect the West subcluster, which hosts a strong-lensing arc. S. Miyazaki et al. (2015) detected the cluster in a WL analysis of wide-field Subaru HSC observations. Their mass estimates are $7.0^{+1.8}_{-1.6} \times 10^{14}\,M_{\odot}$, $4.6^{+1.4}_{-1.2} \times 10^{14}\,M_{\odot}$, and $4.8^{+1.6}_{-1.3} \times 10^{14}\,M_{\odot}$ for the Main, Middle, and East subclusters, respectively.

G19 separated the cluster galaxies into four subclusters but not the same subclusters as the previous WL results. Instead, they detected the Middle subcluster and then separated the Main subcluster into three additional subclusters.

WL result. Our WL result detects five subclusters: Main, Middle, East, West (not shown in the figure), and one to the north. The Main subcluster coincides with the brightest X-ray emission and the BCG. The Main WL distribution is elongated in an east–west direction and has extensions to the west and north. These extensions are in agreement with the three substructures detected by G19. Both the Middle and East subclusters have X-ray emission counterparts. We remind the reader that the East subcluster is at a redshift of $z = 0.43$. The north detection is coincident with a galaxy overdensity ($z \sim 0.3$) and has X-ray emission as shown in A. Botteon et al. (2019). The north mass peak is detected in the DLS analysis (D. Wittman et al. 2014) and in S. Miyazaki et al. (2015), but the mass is not estimated. We fit a four-halo model to the mass distribution and find masses of $M_{200,\mathrm{Main}} = 3.5 \pm 0.8 \times 10^{14}\,M_{\odot}$, $M_{200,\mathrm{Middle}} = 4.2 \pm 0.9 \times 10^{14}\,M_{\odot}$,

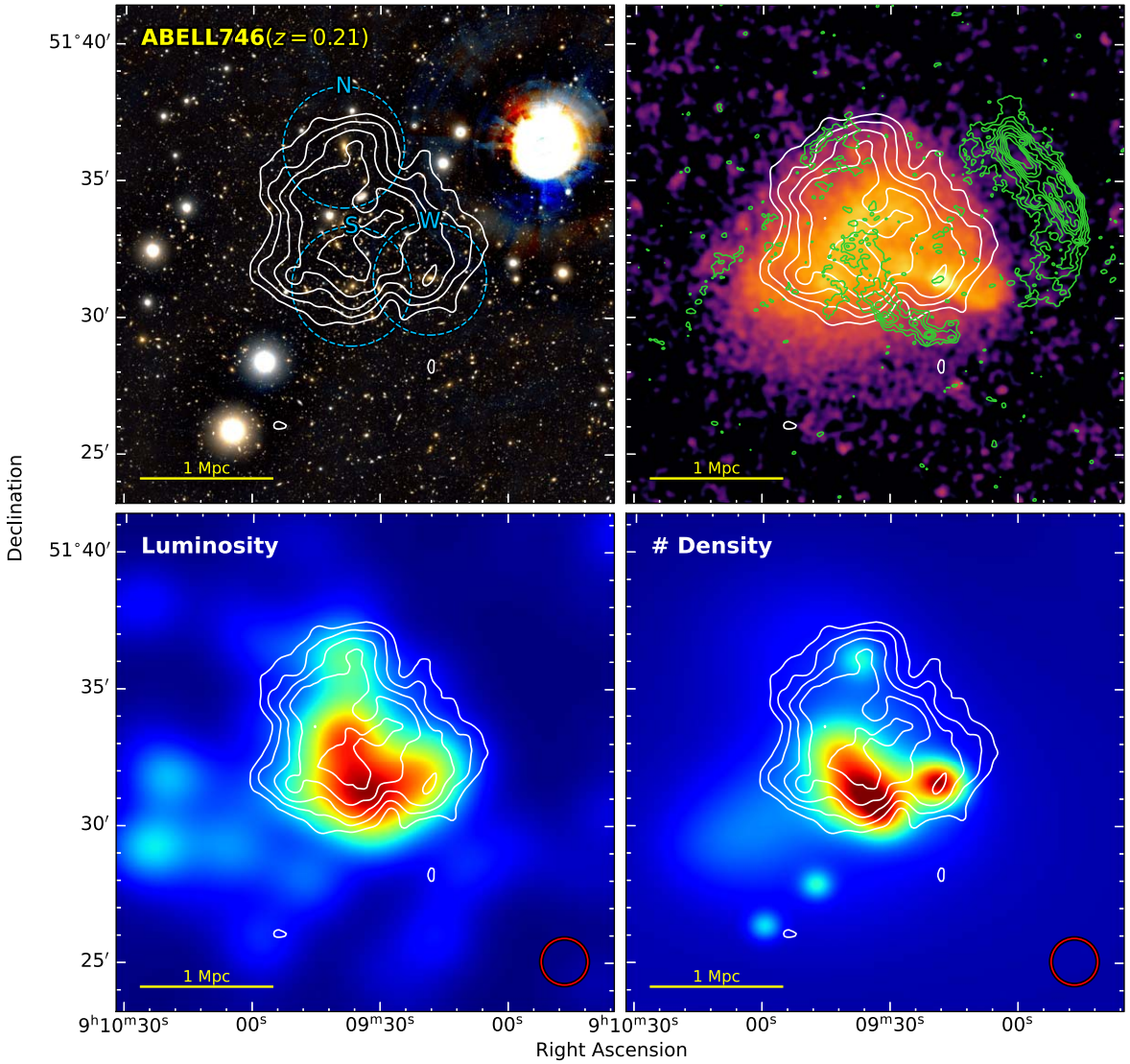

Figure 12. A746. A complex cluster merger with four diffuse radio sources. WL contours increase in steps of 0.5σ.

$M_{200,\mathrm{East}} = 3.3 \pm 0.8 \times 10^{14}\, M_{\odot}$, and $M_{200,\mathrm{North}} = 1.7 \pm 0.6 \times 10^{14}\, M_{\odot}$. These mass estimates are consistent with past studies (N. Sehgal et al. 2008; A. Abate et al. 2009) and only show a slight departure from the Main cluster estimates of D. Wittman et al. (2014) and S. Miyazaki et al. (2015).

Merger insight. The location of the candidate radio relic and the X-ray emission hint that the merger-induced shock originated within the Main cluster. The elongation of the X-ray emission and the mass map agrees with this scenario. However, the resolution that is achievable with ground-based WL is insufficient to discern substructures in the Main subcluster and prevents us from constraining the mass of the collision that may have formed the relic.

4.7. A1240 (z = 0.195)

A1240 is a double-relic cluster with relics situated at opposing ends of the ICM distribution (A. Bonafede et al. 2009; D. N. Hoang et al. 2018). From the radio spectral indices, D. N. Hoang et al. (2018) derived Mach numbers of 2.4 and 2.3 for the north and south shocks, respectively. The X-ray emission spans the region between the radio relics and shows gas dissociation. R. Barrena et al. (2009) detected two X-ray emission peaks in the Chandra observation and estimated the global temperature of the ICM to be 6 keV. A. Sarkar et al. (2024) measured X-ray shocks ($M_{\mathrm{S}} = 1.5$ and $M_{\mathrm{N}} = 1.4$) at the locations of both radio relics. G19 found that a two-halo model for the galaxy distribution was favored with a 1:1 mass ratio. A second cluster, A1237 ($z = 0.194$), is located about 1.5 Mpc to the south of A1240.

WL result. This WL analysis was presented in H. Cho et al. (2022). The WL signal of A1240 (Figure 14) shows the characteristic two peaks that are expected in bimodal mergers. The mass distribution is elongated along the merger axis that is signified by the X-ray and radio emission. The mass peak in the south is directly on the BCG. The northern mass peak shows an offset but is statistically consistent with the BCG based on our bootstrapping. The signal from A1237 is also detected. We determine the masses to be approximately equal for the A1240 merger with $M_{200,\mathrm{N}} = 2.6 \pm 0.6 \times 10^{14} M_{\odot}$ and $M_{200,\mathrm{S}} = 1.1 \pm 0.4 \times 10^{14} M_{\odot}$ for the northern and southern subclusters, respectively. A bridge in the WL signal is found that runs between the A1240 and A1237 but at low significance.

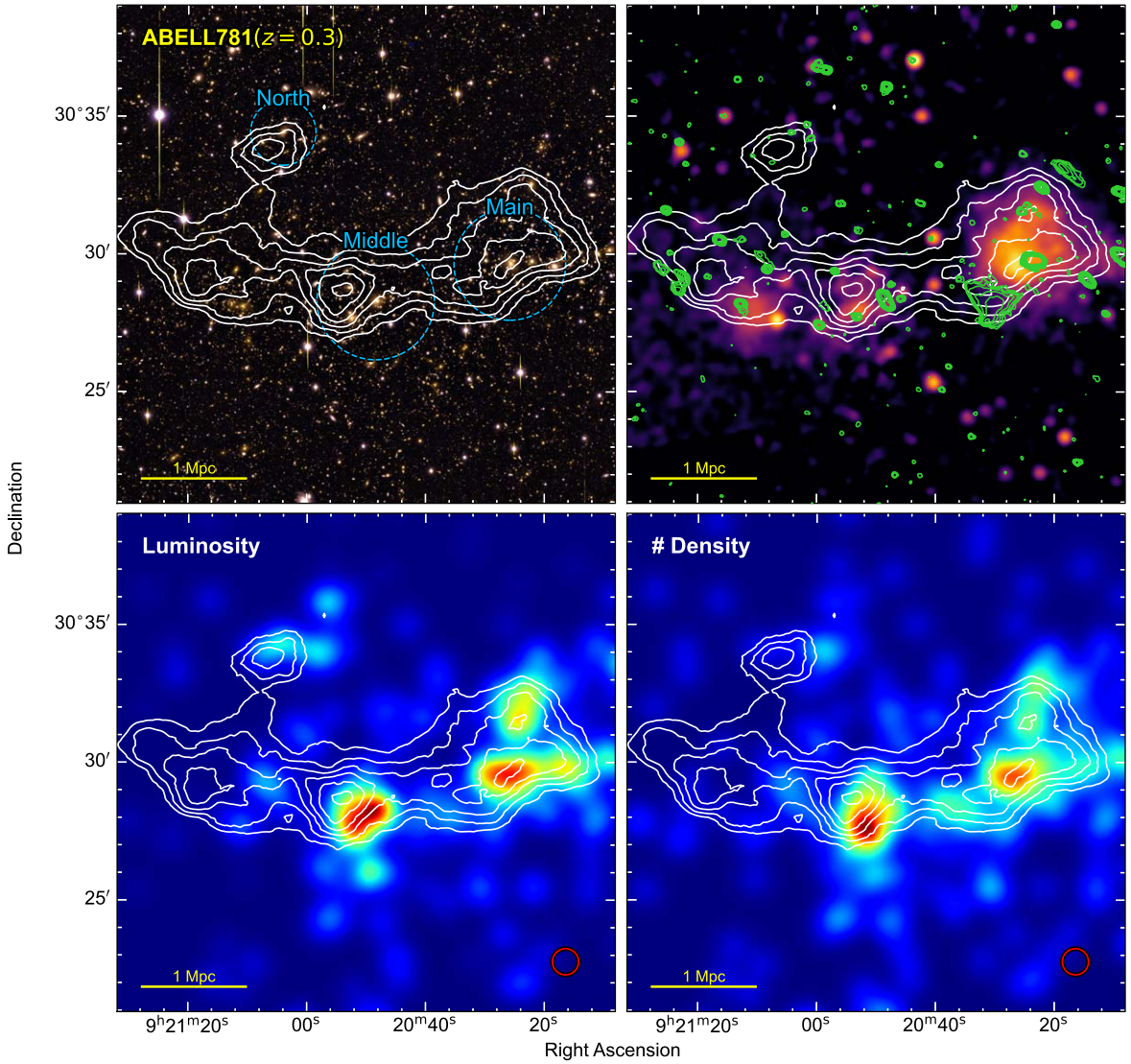

Figure 13. A781. A large-scale structure of clusters comprised of Main, Middle, and North. East is at a higher redshift. WL contours increase in steps of 0.5σ.

Merger insight. A1240 is a bimodal merger with a 2:1 mass ratio. H. Cho et al. (2022) utilized the projected separation of the radio relics and the Monte Carlo Merger Analysis Code (W. A. Dawson 2013) to find that a merger phase that is returning from apocenter is favored with a time since collision of 1.7 ± 0.2 Gyr. H. Cho et al. (2022) showed that the A1240/1237 system is embedded in a $\sim$80 Mpc long filament as defined from SDSS galaxy positions. Further investigation of the connection of the merger to the filament would be interesting. The extreme dissociation of the gas for A1240 makes it a great candidate for further study of the nature of dark matter.

4.8. A1300 (z = 0.306)

A. D. Reid et al. (1999) detected two diffuse radio sources in A1300, a radio halo and relic (both confirmed by S. Giacintucci 2011). M. Pierre et al. (1997) performed a dynamical analysis and found that the velocity dispersion of the cluster galaxies had no significant departure from a Gaussian distribution. However, L. Lemonon et al. (1997) highlighted the merging nature of A1300 from the structures seen in X-ray emission. F. Ziparo et al. (2012) analyzed XMM-Newton X-ray observations and showed that there are three primary ICM features: a bright peak in the south that elongates toward the southeast, a fainter peak about 250 kpc to the north, and an extension, possibly a filament, farther north. The BCG lies directly on top of the bright X-ray peak in the south and has a semimajor axis along the same direction as the elongation of the X-ray emission. B. Terni de Gregory et al. (2021) presented the radio relic in the 1.3 GHz MeerKAT observation and noted that it has the morphology expected for radio emission from merger-induced shocks. G19 were unable to separate the cluster galaxies into multiple structures.

WL result. The WL map of A1300 (Figure 15) does not follow our expectations based on the X-ray emission. Three features of the mass distribution stand out: a triangular-shaped clump in the center, a subcluster detached to the southeast, and a long extension to the north. The main clump has a primary peak that resides between the BCG and a bright galaxy immediately to its north. This peak is also offset from the X-ray brightness peak. The eastern vertex of the triangle has a nearby bright cluster galaxy and so does the northern vertex. It is likely that the complexity of the cluster is beyond the capabilities of the Subaru imaging. The extension to the north roughly follows

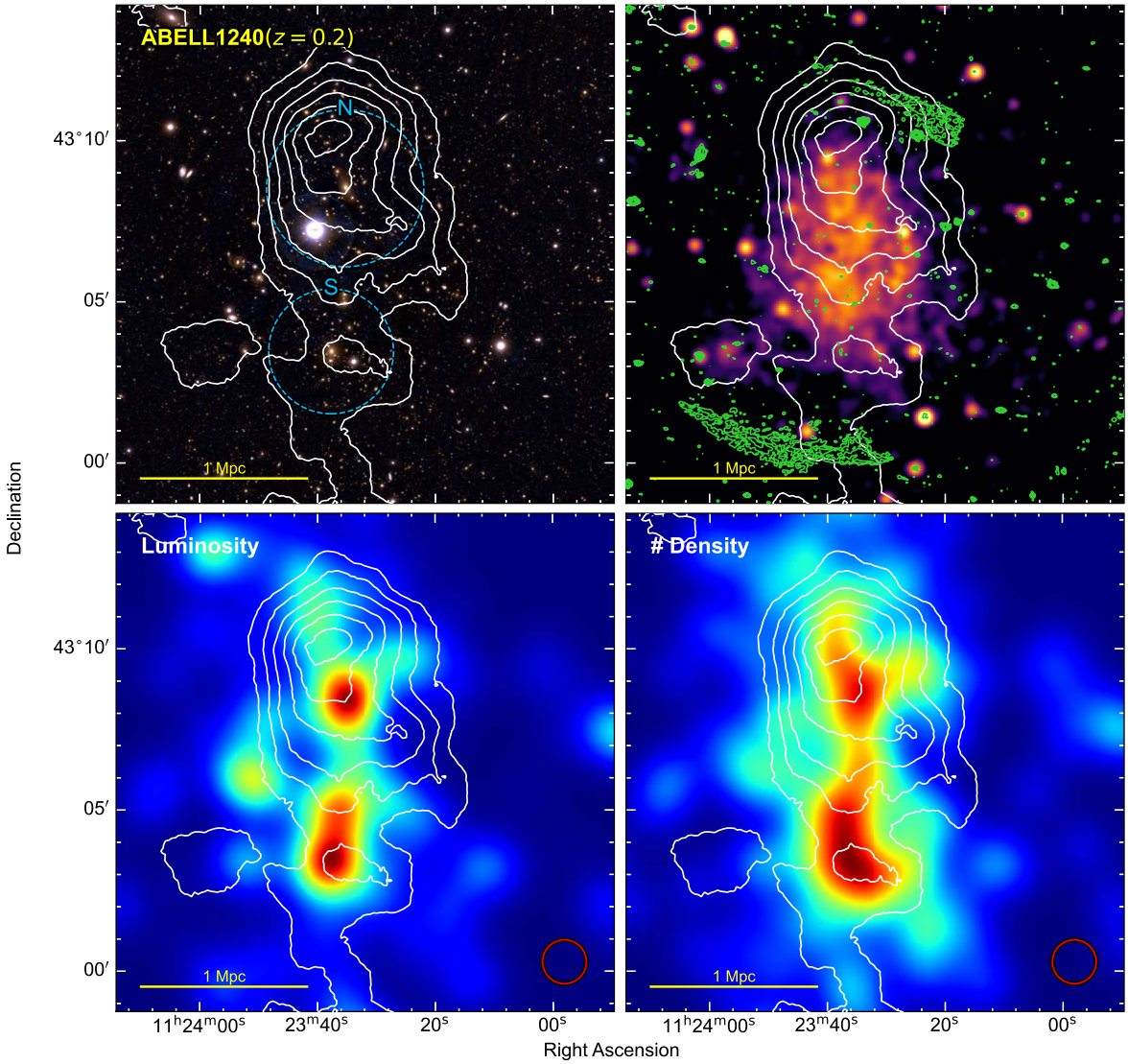

Figure 14. A1240. A head-on collision, dissociative merger with double radio relics. WL contours increase in steps of 1σ.

cluster galaxies, as can be seen in the luminosity and number density panels. It also follows the X-ray emission. The subcluster detected ∼1 Mpc to the southeast coincides with a bright galaxy and a faint X-ray detection. The agreement between the overall mass map and the X-ray emission is mixed. Since there is a lack of consistency between the WL substructures and the luminous tracers, we fit a single halo NFW model centered at the BCG and find the mass of the cluster to be $M_{200} = 1.1 \pm 0.2 \times 10^{15} M_{\odot}$.

Merger insight. The X-ray morphology is complicated and does not provide a clear feature that matches the position of the radio relic. The core of the X-ray emission has a bullet shape, which is sometimes a good indicator of the merger axis. However, like A115, it is hard to reconcile the bullet and the position of the radio relic. Perhaps, this is another case of a large impact parameter merger. The WL result seems to further complicate the interpretation because it is offset from the X-ray peak. However, the elongation of the core of the WL result does align with the radio relic. Similar to A746, the complexity of the merger seems to be beyond the ground-based Subaru imaging and may require higher resolution to discern the merging subclusters.

4.9. A1612 (z = 0.182)

A1612 has a single radio relic (R. J. van Weeren et al. 2011b) in the southeast that is offset from the axis defined by the elongated X-ray emission and the BCG positions. The X-ray emission does not show significant features, mostly because of the lack of X-ray photon counts, but it does span the region between the east and west BCGs. G19 found two subclusters of galaxies that are each centered on the two BCGs.

WL result. The WL signal from A1612 shows two peaks separated by ∼1 Mpc (Figure 16). The east mass peak is coincident with the BCG and has a weaker S/N companion mass peak that is centered on the equally bright galaxy to its immediate south. The western peak is near the third BCG. The peaks are found at the ends of the elongated X-ray distribution. The *i*-band observations are shallow for this cluster, and the WL signal is poor, even though the subclusters are resolved. A two-halo fit centered at the east and west BCGs finds masses of $M_{200,\mathrm{E}} = 4.0 \pm 1.0 \times 10^{14} M_{\odot}$ and $M_{200,\mathrm{W}} = 1.8 \pm 0.7 \times 10^{14} M_{\odot}$.

Merger insight. A1612 is a good candidate for a simple merger with a nearly equal mass ratio. However, the cluster has not garnered enough attention and lacks sufficient

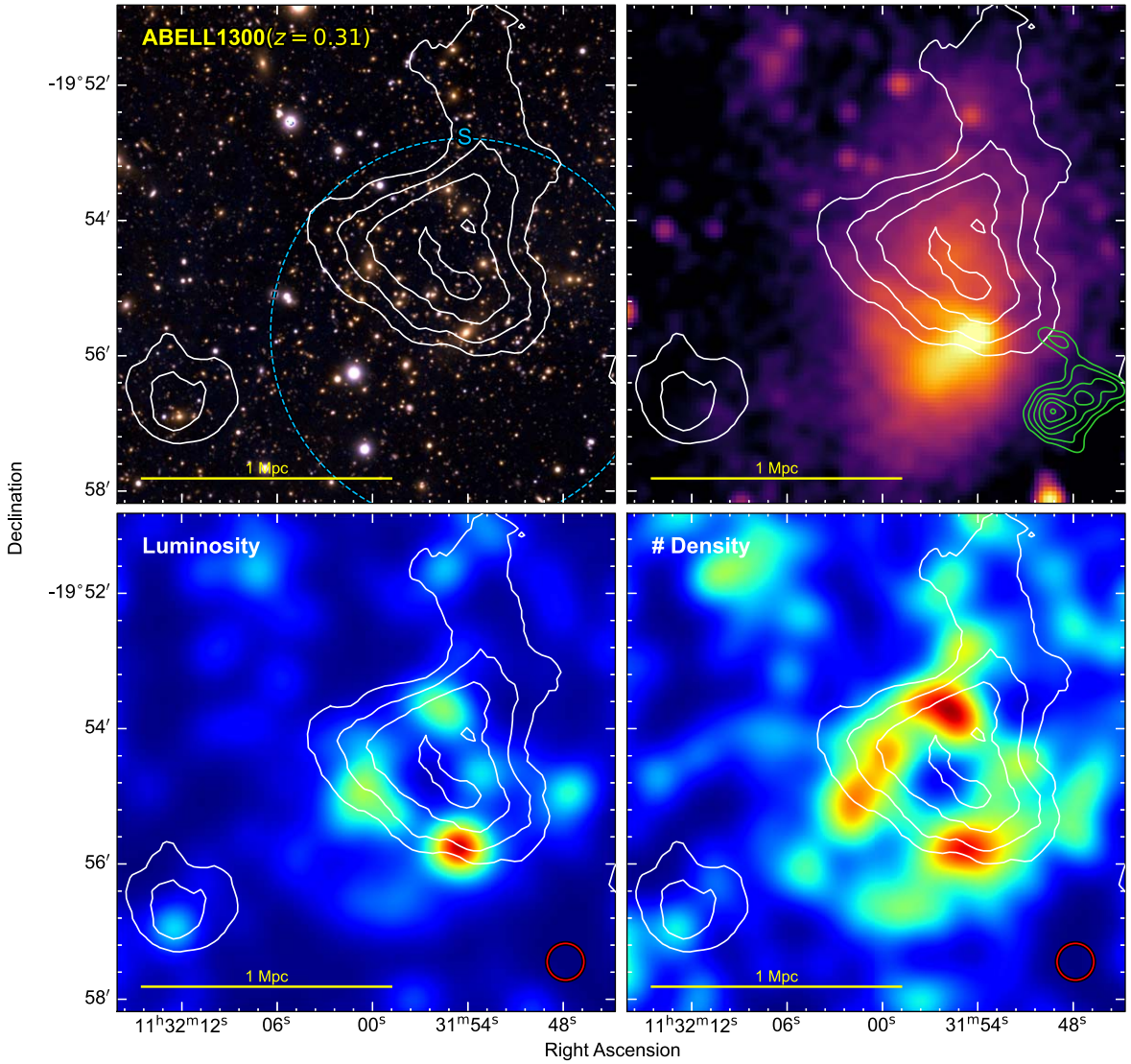

Figure 15. A1300. A complex cluster with an offset of the mass peak from the X-ray emission peak. An extension in the mass map traces an extension in the X-ray map to the north. WL contours increase in steps of 1σ.

multiwavelength observations to make strong conclusions about the collision. The radio relic is not in line with the elongation of the X-ray emission or the mass distribution, which may indicate a nonzero impact parameter of the collision. The eastern mass peak and its BCG do not have bright X-ray emission, and thus A1612 may be a case of a dissociative merger.

4.10. A2034 (z = 0.114)

A2034 is a dissociative merger with a bullet-shaped morphology in the X-ray emission. A cold front was found in the Chandra observation and a candidate radio relic (J. C. Kempner & C. L. Sarazin 2001; J. C. Kempner et al. 2003). A shock ahead of the northern cold front was detected in M. S. Owers et al. (2014) with a Mach number of 1.6 ± 0.1. For an in-depth discussion of the radio emission, see the LOFAR work by T. W. Shimwell et al. (2016), which presents two additional radio relic candidates.

N. Okabe & K. Umetsu (2008) performed a WL analysis of the cluster and detected six significant peaks, of which three are slightly background to the cluster redshift. They suggested that these peaks may comprise a large-scale filament. R. Monteiro-Oliveira et al. (2018) also presented a WL analysis of the cluster. Their mass map detected two significant peaks (with additional subpeaks) that are considered the counterparts to the BCGs. In their work, the southern and strongest peak is situated to the south of the BCG, and the northern peak is slightly offset to the east of the northern BCG. They estimate the masses of the subclusters to be $2.4 \pm 1.0 \times 10^{14} M_{\odot}$ and $1.1 \pm 0.6 \times 10^{14} M_{\odot}$ for the south and north.

G19 found three galaxy overdensities that are centered in the north, south, and southwest regions. Their velocity dispersion measurements show that the northern and southern subclusters are comparable in mass, and the southwest subcluster is minor. M. T. Moura et al. (2021) simulated the cluster with *N*-body hydrodynamical simulations using the measured properties from R. Monteiro-Oliveira et al. (2018) as initial conditions. They concluded that the merger is near the plane of the sky with a low impact parameter and about 0.26 Gyr after collision.

WL result. Our mass map (Figure 17) portrays a binary merger between the northern and southern subclusters with a

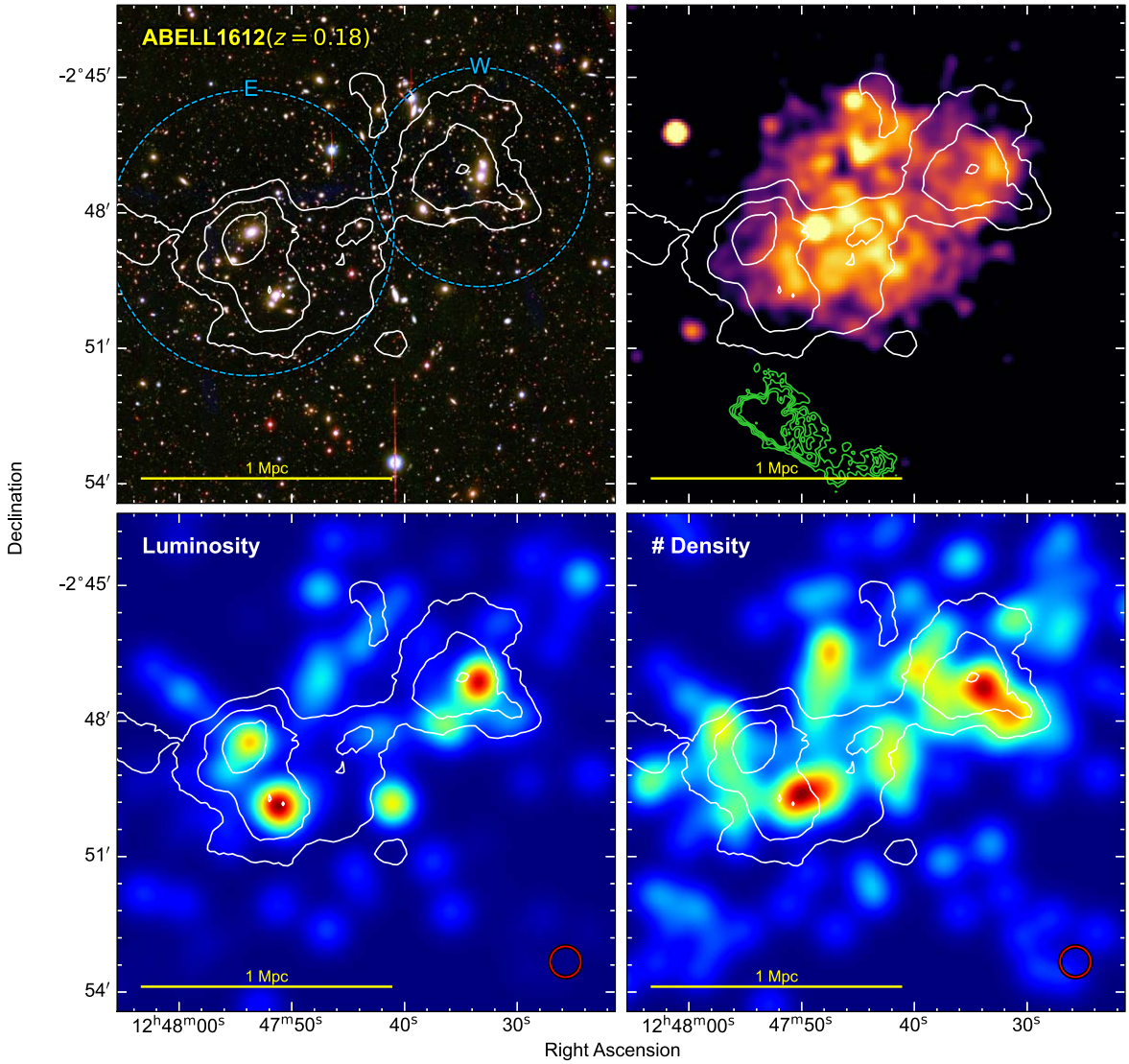

Figure 16. A1612. A merger between two equal-mass subclusters with a radio relic that is misaligned with the WL and X-ray elongated distributions. WL contours increase in steps of 0.5σ.

third mass clump found to the southwest. This is in agreement with the two previous WL studies of N. Okabe & K. Umetsu (2008) and R. Monteiro-Oliveira et al. (2018) and the dynamical analysis of G19. The mass peak in the south is coincident with the BCG. The mass peak in the north is offset to the east of its BCG but within the WL statistical uncertainty. The extension to the southwest lies on top of the third BCG with a weakly detected peak nearby. Our mass estimates are $M_{200,\mathrm{S}} = 2.6 \pm 0.7 \times 10^{14}\,M_{\odot}$, $M_{200,\mathrm{N}} = 1.1 \pm 0.4 \times 10^{14}\,M_{\odot}$, and $M_{200,\mathrm{SW}} = 0.6 \pm 0.3 \times 10^{14}\,M_{\odot}$.

Merger insight. A2034 appears to be the most head-on merger in the sample. It has a large gas dissociation and thus is an ideal cluster for studying dark matter properties. There are some interesting features of this cluster that may warrant further investigation. The published WL analyses of this cluster show a consistent offset of the northern mass peak to the east of its BCG. Is this a systematic of the data or an offset caused by the collision? The southern BCG is highly elongated along the merger axis. Is this a signature of the recent pericenter passage?

4.11. A2061 (z = 0.078)

A2061 is the lowest-redshift cluster in the sample. It is part of the Corona Borealis supercluster (M. Postman et al. 1988; D. W. Pearson et al. 2014). The X-ray emission peaks between the two BCGs suggesting that it is also a dissociative merger. Northeast of the cluster is a blob of X-ray emitting gas that may have been ejected from the main cluster (C. Sarazin et al. 2014). The radio relic is approximately 2 Mpc southwest of the X-ray emission peak of the cluster (J. C. Kempner & C. L. Sarazin 2001; R. J. van Weeren et al. 2011b). G19 found that the cluster galaxies follow a single-Gaussian distribution with mass from velocity dispersion being $5.5 \pm 0.2 \times 10^{14}\,M_{\odot}$.

WL result. The WL map of A2061 shows a bimodal distribution with mass peaks that lie directly on top of the BCGs (Figure 18). The elongation of the mass map is slightly rotated from the elongation of the X-ray emission. Our two-halo fit estimates masses of $M_{200,\mathrm{S}} = 1.6 \pm 0.5 \times 10^{14}\,M_{\odot}$ and $M_{200,\mathrm{N}} = 2.0 \pm 0.6 \times 10^{14}\,M_{\odot}$, which suggests a 1:1 mass ratio

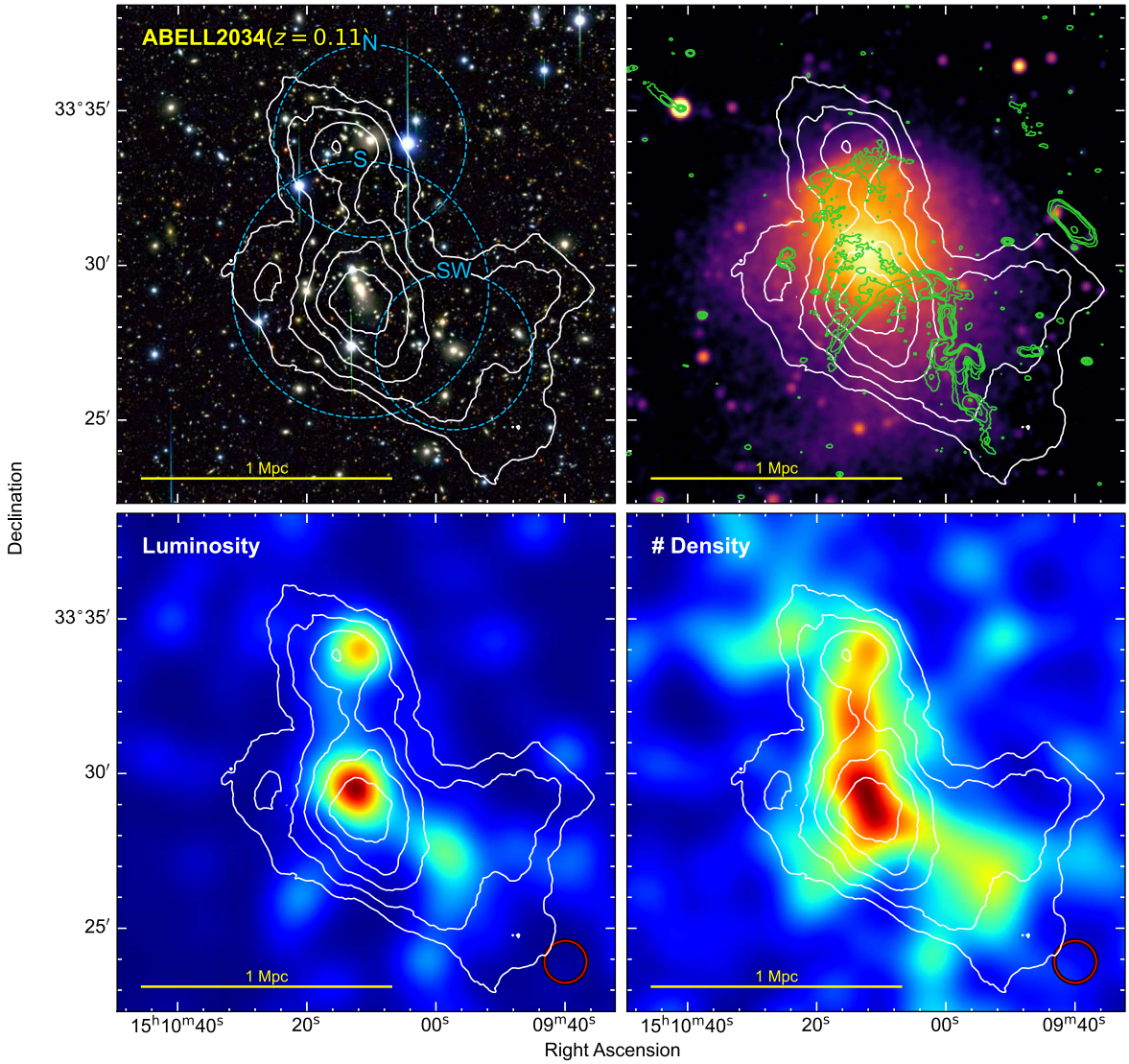

Figure 17. A2034. A dissociative merger with a bullet shape. WL contours increase in steps of 1σ.

merger of low total mass. The total mass found from lensing is in agreement with that of velocity dispersion.

Merger insight. The different orientations of elongation for the mass map and the X-ray emission are a possible signature of the impact parameter of the collision. The radio relic of A2061 is one of the farthest from the cluster when compared to the rest of this radio relic sample. The distance of the radio relic could be a hint that A2061 is an old merger. The galaxy distributions of A2061 show a group to the northeast, and the WL signal has a slight elongation toward the direction of the group. It is unclear if this group was involved in the merger or is currently falling into the primary cluster. A2061 is a cluster that warrants further investigation to understand its dissociative nature and extreme distance to its radio relic.

4.12. A2163 (z = 0.201)

With a global temperature of $T = 15$ keV (M. Arnaud et al. 1992), A2163 is one of the hottest clusters in the sample. It is listed as the most massive cluster in the Planck Collaboration et al. (2016) catalog. The X-ray emission from A2163 is very extended, spanning approximately 2 Mpc in diameter in the south with an additional X-ray emitting subcluster in the north. A dynamical analysis by S. Maurogordato et al. (2008) showed that the southern cluster is elongated in the east–west direction. G19 found that A2163 is composed of three structures with two located in the southern X-ray emission and one in the north. Based on their velocity dispersion estimates, the southeastern BCG is in the dominant subcluster and the southwestern one is subordinate. The radio relic candidate in A2163 (L. Feretti et al. 2004) is found to the northeast. A. Shweta et al. (2020) provided evidence for a radio relic found in the center of the cluster. S. Thölken et al. (2018) detected three shocks in Suzaku observations. One of the shocks is to the northeast and coincides with the radio relic, and the other two are found in the southwest.

Previous WL analyses have been consistent in detecting two mass peaks in the south and one in the north (M. Radovich et al. 2008; N. Okabe et al. 2011; G. Soucail 2012). G. Soucail (2012) estimated the mass of each subcluster but not within a standard overdensity radius. N. Okabe et al. (2011) found the mass of the subclusters to be $M_{200} = 16.46^{+3.69}_{-5.90} \times 10^{14}\,M_{\odot}$, $M_{200} = 2.08^{+0.96}_{-0.97} \times 10^{14}\,M_{\odot}$, and $M_{200} = 2.43^{+0.90}_{-1.15} \times 10^{14}\,M_{\odot}$ for the East, West, and North subclusters, respectively.

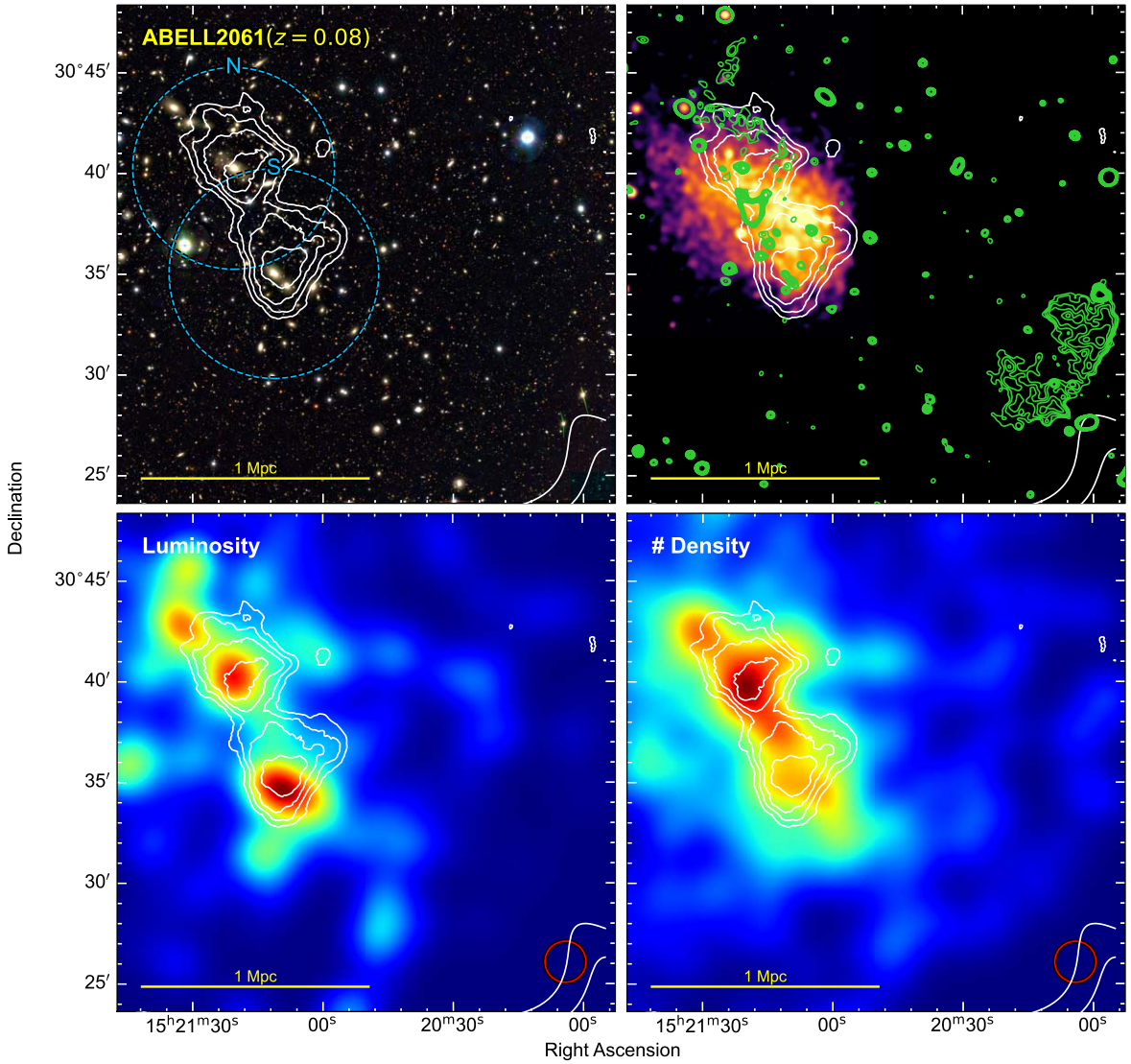

Figure 18. A2061. A dissociative merger with a radio relic that is very distant from the X-ray brightness peak. WL contours increase in steps of 0.5σ.

WL result. Our WL analysis (Figure 19) detects the signal from both the northern and the southern clusters. The mass distribution of the southern cluster has a peak directly on the BCG (labeled as the E halo in Figure 19). From the E peak, the mass distribution stretches to the west where it has a subordinate peak near the W BCG. We assign the extension to the west to the W BCG. The spatial offset of the WL signal in the west from the W BCG is also apparent in other WL studies (N. Okabe et al. 2011; G. Soucail 2012). The second extension of the mass distribution from the E BCG stretches to the south and loosely follows the galaxy luminosity distribution (bottom-left panel). The northern cluster is detected with the mass peak slightly offset from the X-ray emission and the galaxy distributions. This offset is likely from noise. We fit a three-halo model and found that the masses are $M_{200,\mathrm{E}} = 9.2 \pm 1.8 \times 10^{14}\,M_{\odot}$, $M_{200,\mathrm{W}} = 0.8 \pm 0.6 \times 10^{14}\,M_{\odot}$, and $M_{200,\mathrm{N}} = 1.1 \pm 0.7 \times 10^{14}\,M_{\odot}$. These mass estimates are in statistical agreement with the WL mass estimates of G. Soucail (2012) and N. Okabe et al. (2011).

Merger insight. A2163 is a complex cluster with many substructures. S. Maurogordato et al. (2008) described the many substructures of the cluster of A2613 found in galaxy overdensities. The detection of the mass distribution can provide support to some of the substructures. The cluster appears to be elongated east–west, which does not exactly agree with the position of the radio relic. However, the galaxy luminosity distribution shows an elongation extending from the BCG along the northeast–southwest axis that aligns with the position of the radio relic. The WL mass map also extends from the BCG along this axis but at low significance. A past collision between the main cluster and a subcluster directly to its southwest may be the cause of the radio relic, but we are unable to distinguish this in our WL analysis.

4.13. A2255 (z = 0.08)

A2255 has an X-ray morphology that is slightly elliptical with the major axis running east–west. The BCG is located near the western X-ray peak, and there are bright galaxies related to the eastern X-ray emission. G19 was unable to resolve two subclusters in their dynamical analysis but did find a $\sim$2000 km s^{-1} difference in LOS velocity for the two BCGs in the west. A. Botteon et al. (2020b) described the "beautiful mess" of radio sources in A2255 and highlighted the northeast radio relic. Two additional radio relics and an extended radio

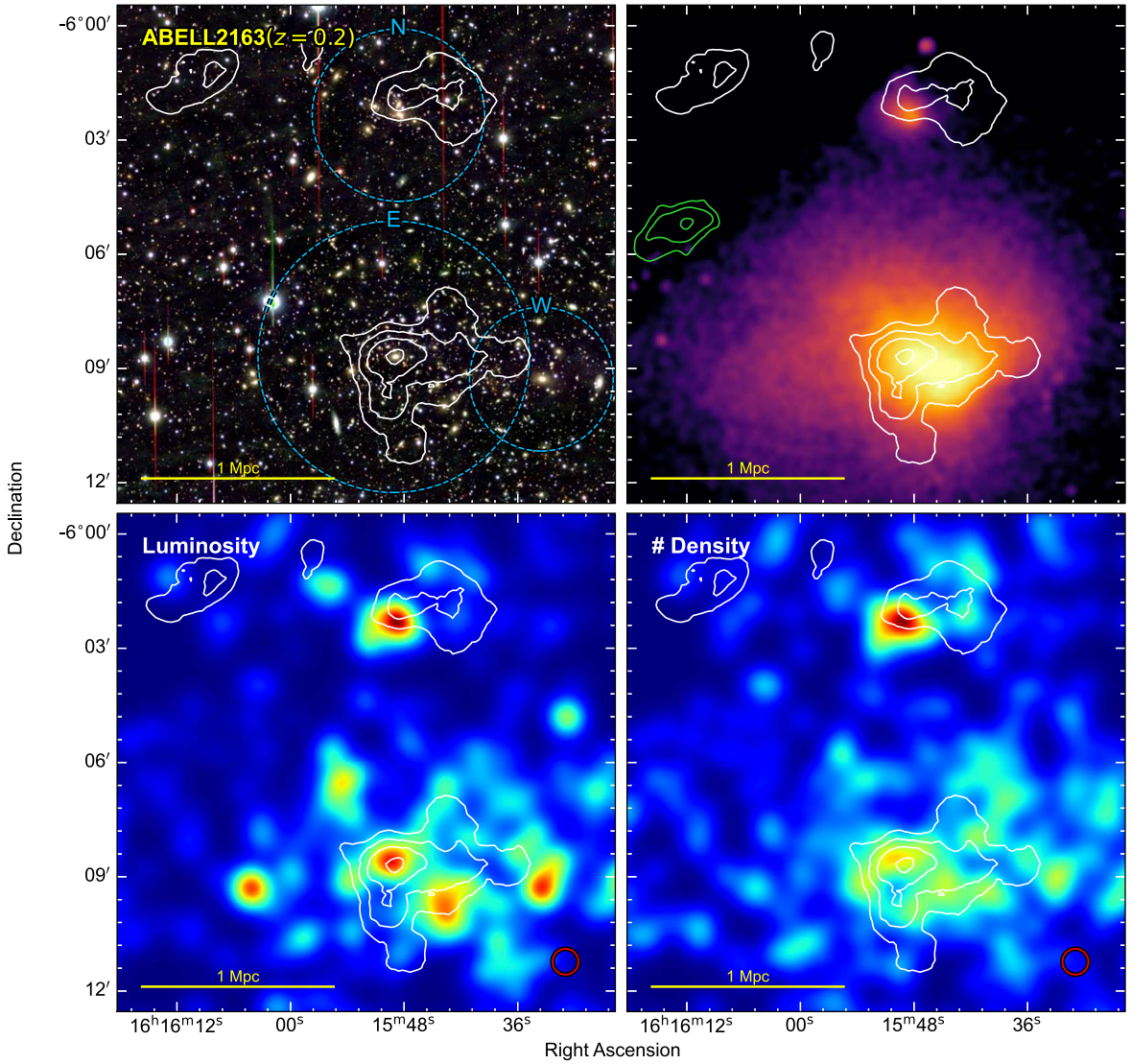

Figure 19. A2163. A low-mass subcluster (W) colliding with a massive primary cluster (E). WL contours increase in steps of 1σ.

emission that covers a significant portion of the cluster were described in A. Botteon et al. (2022b). H. Akamatsu et al. (2017) detected an X-ray shock at the location of the northeast radio relic.

WL result. The WL map provides far more context to the merging system than the X-ray emission (Figure 20). The mass distribution traces the bright cluster galaxies and is elongated along the east–west axis. A mass peak is coincident with the western BCG, and an equally significant mass peak is detected about 100 kpc to its southwest. The WL signal extends to the east and is coincident with the eastern BCG. The proximity of the two western peaks prevents a three-halo model from being robustly fit. Our two-halo model gives masses of $M_{200,\mathrm{W}} = 4.7 \pm 1.1 \times 10^{14}\,M_{\odot}$ and $M_{200,\mathrm{E}} = 1.3 \pm 0.6 \times 10^{14}\,M_{\odot}$.

Merger insight. There is great agreement between the WL mass map and the galaxy positions in A2255. The X-ray brightness peak is offset from the BCG and the mass peak, which makes this cluster a dissociative merger candidate. The mass map provides critical information that can explain the location of the northeast radio relic. Rather than a merger between the eastern and western subclusters, it is more likely that a collision between the two substructures in the west led to the formation of the radio relic. Extending a line from the two substructures in the west bisects the radio relic. If these are the two subclusters that collided to form the radio relic, then their very small projected separation (∼200 kpc) relative to the distance to the radio relic (∼1 Mpc) is intriguing. This could indicate that the subclusters have had time to reach apocenter and begin their return to a second pericenter passage. Also, the large LOS velocity difference of the two BCGs in the west may indicate that projection may be important. This is an interesting case for the potential of a merger with an LOS component to the merger and a radio relic.

4.14. A2345 (z = 0.179)

A2345 is a rare double-relic cluster (A. Bonafede et al. 2009). C. Stuardi et al. (2021) described additional merger features in the X-ray and radio emission. The eastern relic is greater than 1 Mpc in size and has the standard arc shape of a shock. The BCG is located in the east and is coincident with the X-ray brightness peak. The second brightest galaxy is 2 Mpc to the west of the BCG. The X-ray emission spans about 2 Mpc by 2 Mpc in projection, which includes a subcluster that is located to the northwest of the second brightest galaxy. G19

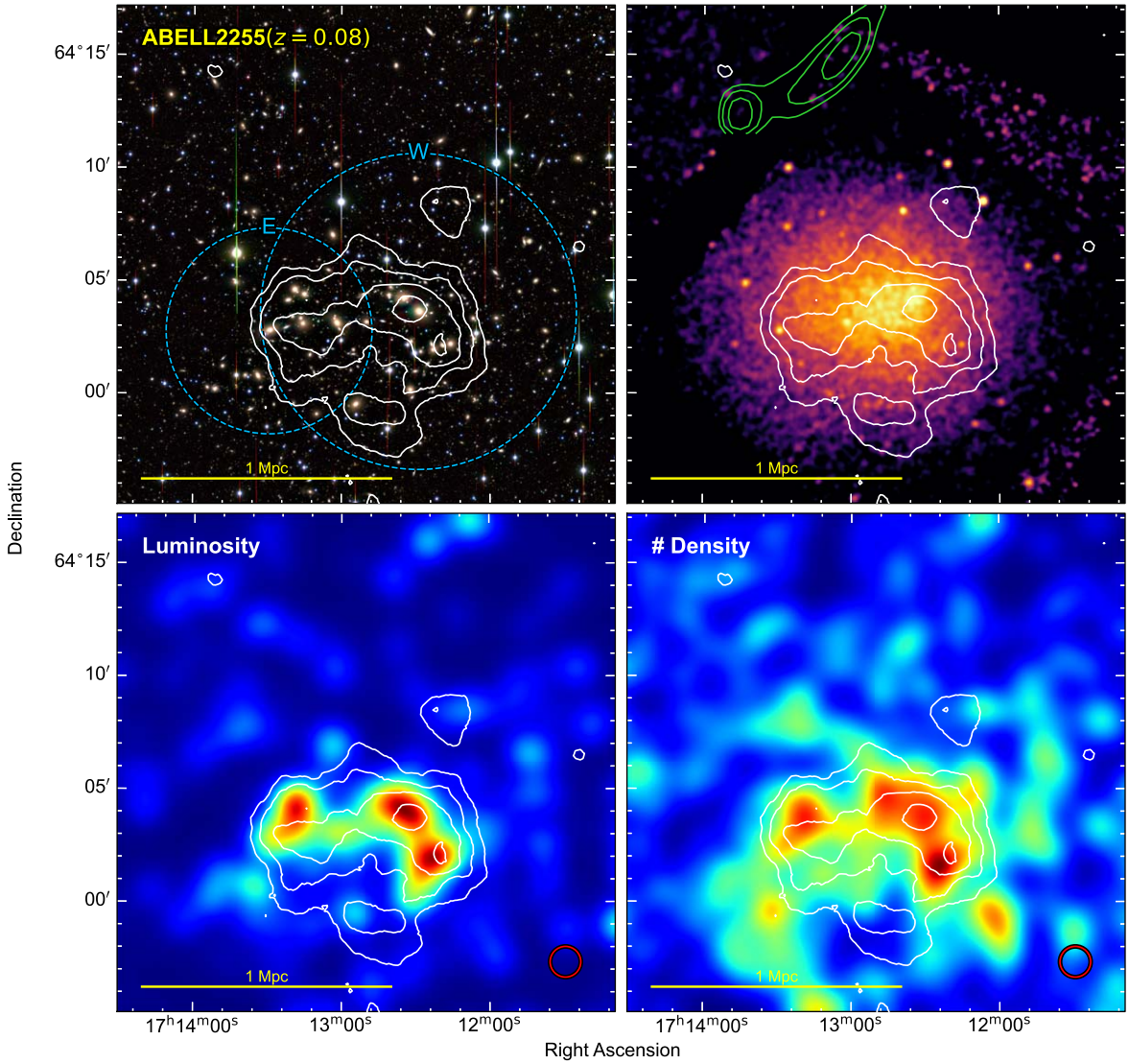

Figure 20. A2255. A relaxed-appearing X-ray emission with WL substructures. WL contours increase in steps of 1σ.

were unable to separate subclusters in their analysis, but they did present three peaks in the galaxy light distribution.

H. Dahle et al. (2002) presented a WL result of A2345 with three peaks that are distributed in an east–west axis. One peak is located $\sim$1.″5 to the east of the BCG, a second is found near the BCG, and a third peak is near a smaller galaxy overdensity (the location of our central BCG). The WL analysis of N. Okabe et al. (2010) also found an east–west elongated mass distribution with two clear peaks that are located at the eastern BCG and $\sim$500 kpc east of the eastern BCG. They also found a long extension in their mass map that stretches to the northwest and a separate subcluster in the west.

WL result. Our WL distribution of A2345 (Figure 21) is tri-peaked in a chain that aligns with the axis connecting the radio relics. The distances between the central peak and the two other peaks are similar. As in H. Dahle et al. (2002) and N. Okabe et al. (2010), the eastern mass peak is offset from the BCG toward the eastern radio relic. The east mass peak is also detached from the bright X-ray emission, indicating a potential dissociative merger. The central peak is located in a region without bright cluster galaxies, but it is a region with many galaxies (see number density map). This detection is reminiscent of the dark core in A520, the Trainwreck cluster (A. Mahdavi et al. 2007; M. J. Jee et al. 2012). However, it is worth noting that N. Okabe et al. (2010) did not detect this region as a strong peak, but as a north–south elongated distribution. The western peak is centered on the second BCG and the X-ray emission. N. Okabe et al. (2010) detected a mass peak in the same region. Mass estimates for the three subclusters are $M_{200,\mathrm{E}} = 4.7 \pm 1.1 \times 10^{14}\,M_{\odot}$, $M_{200,\mathrm{C}} = 3.2 \pm 1.0 \times 10^{14}\,M_{\odot}$, and $M_{200,\mathrm{W}} = 2.1 \pm 0.8 \times 10^{14}\,M_{\odot}$.

Merger insight. Utilizing the information from the mass map, it is likely that the radio relics were formed by a merger between the east and central subclusters. These two mass peaks are approximately equal distance from the respective radio relics. The western mass peak is external to the radio relic. However, C. Stuardi et al. (2021) described a bullet feature that is coincident with this WL peak and has a tail to the east. This evidence would suggest that the western subcluster is moving westward, further complicating the merging scenario. For this subcluster to have formed the western relic and be positioned farther westward, it would have to overrun it. Assuming a collision between the eastern and central subclusters formed the

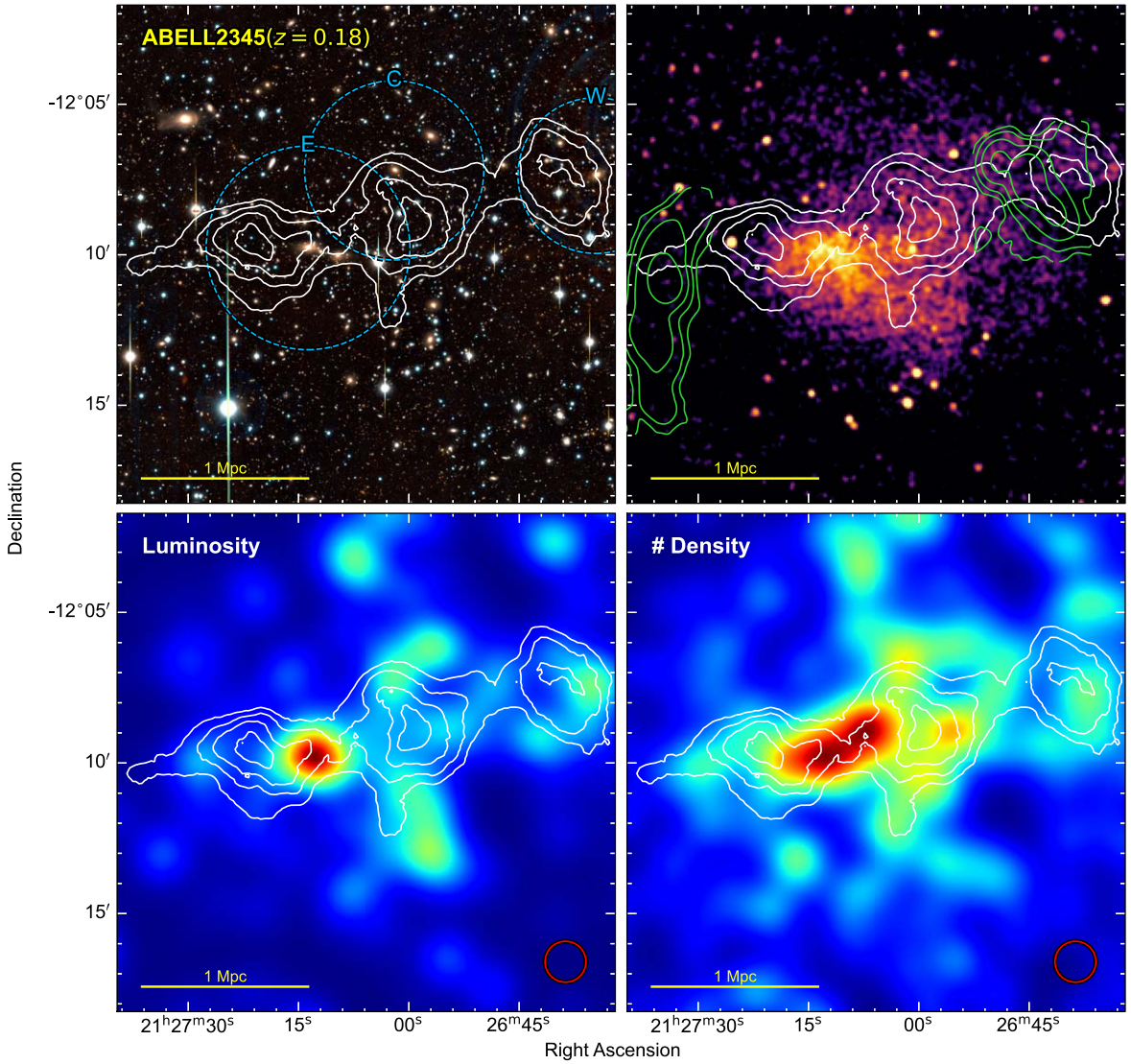

Figure 21. A2345. A chain of three subclusters in a merging system with two relics. WL contours increase in steps of 0.5σ.

radio relics, the remaining issue is understanding the central mass peak and its lack of BCG.

4.15. A2744 (z = 0.306)

A2744 (Pandora's cluster) is one of the most studied clusters in the sample. The X-ray emission from A2744 has two peaks with the brighter near the BCG and the fainter to the northwest. G. Giovannini et al. (1999) detected a radio halo and the northeastern radio relic in the NRAO VLA Sky Survey. C. J. J. Pearce et al. (2017) identified three more radio relics in VLA observations. The radio features have been further analyzed by K. Rajpurohit et al. (2021) and K. Knowles et al. (2022).

Many WL and SL analyses have been accomplished for this cluster. J. Merten et al. (2011) mapped the mass distribution of A2744 and resolved four distinct subclusters. The joint SL–WL analysis (M. Jauzac et al. 2016a) traced the substructure of the cluster at high precision and discerned the substructures in the core. E. Medezinski et al. (2016) performed a WL analysis of the Subaru observations that are used in this paper. They detected four mass peaks at high significance, but three of the peaks are at different positions than the J. Merten et al. (2011) peaks. More recently, the joint SL–WL analysis of S. Cha et al. (2024) used JWST to provide tight constraints on mass peaks that agree with their respective BCGs (see D. R. Harvey & R. Massey 2024, for another JWST WL analysis). D. Abriola et al. (2024) performed a WL analysis with Magellan observations and detected three significant mass peaks.

WL result. Our WL analysis detects four peaks (Figure 22). The most significant peak is found on the E BCG. The second most significant peak is at the location of the W BCG. The W peak and its BCG are offset eastward from the western X-ray emission peak. The two other mass-peak detections are in the north and south and are coincident with cluster galaxy populations. Our four-halo model results in mass estimates of $M_{200,\mathrm{E}} = 7.2 \pm 1.8 \times 10^{14}\,M_{\odot}$, $M_{200,\mathrm{W}} = 6.6 \pm 2.3 \times 10^{14}\,M_{\odot}$, $M_{200,\mathrm{N}} = 1.0 \pm 0.8 \times 10^{14}\,M_{\odot}$, and $M_{200,\mathrm{S}} = 0.6 \pm 0.6 \times 10^{14}\,M_{\odot}$. It is difficult to match our WL detected subclusters with those of E. Medezinski et al. (2016), but it is clear that our eastern subcluster matches their southern subcluster, and our mass estimate is in agreement with theirs. The positions of the mass peaks in J. Merten et al. (2011) and M. Jauzac et al. (2016a) are in better agreement with ours. Converting our mass estimates to the mass within an aperture of

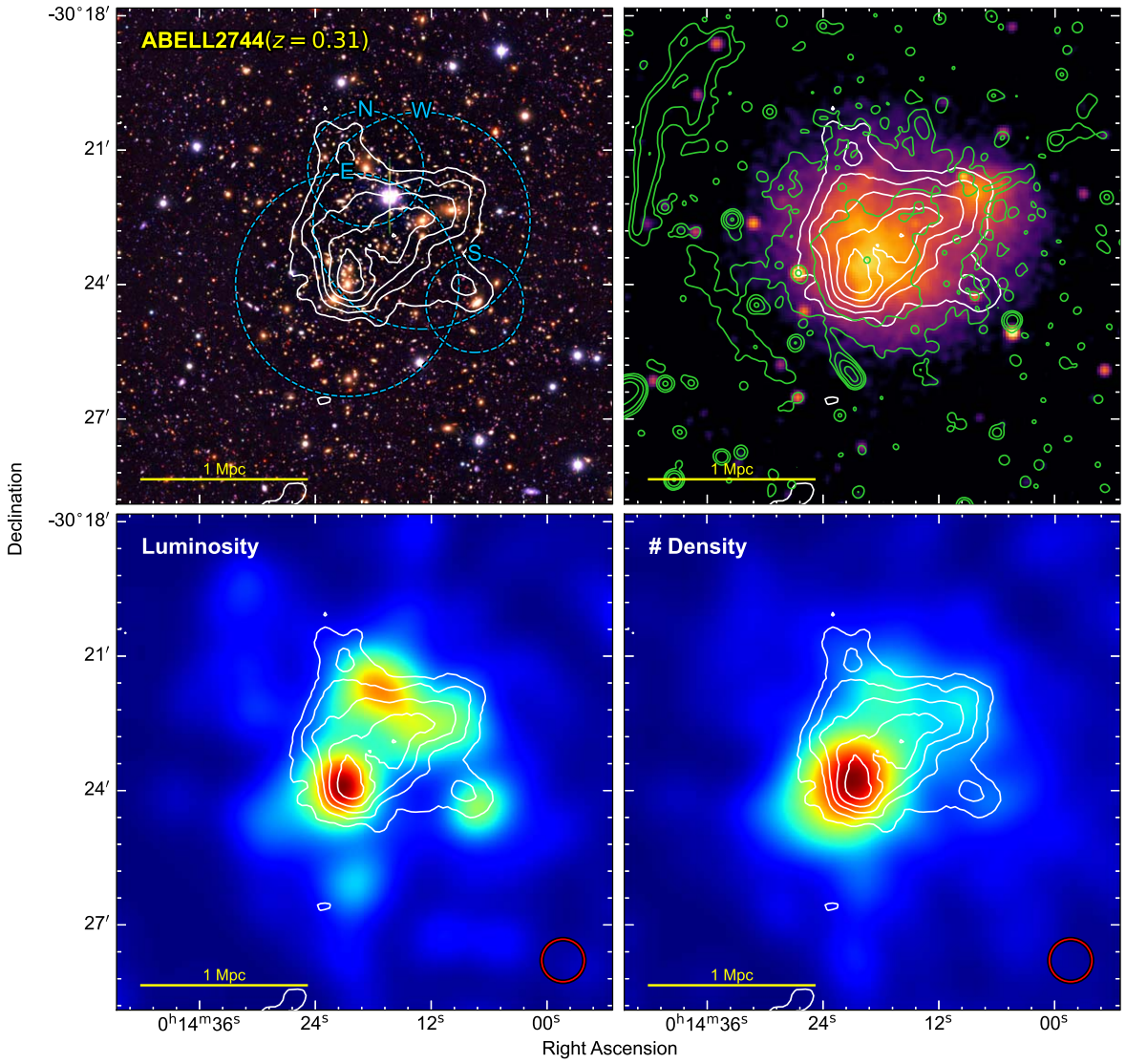

Figure 22. A2744. A well-studied, complex system of four subclusters. WL contours increase in steps of 1σ.

250 kpc, as done in J. Merten et al. (2011) and M. Jauzac et al. (2016a), shows that our western and northern subcluster mass estimates are consistent with theirs. However, our mass estimates for the eastern and southern subclusters are about half the J. Merten et al. (2011) and M. Jauzac et al. (2016a) results.

Merger insight. The position of the southeastern radio relic is easy to relate to the two bright X-ray peaks and the significant WL peaks of the east and west. However, the northeastern and brighter relic is harder to reconcile with the detected substructures. It may be that one of the less significant subclusters passed through the system to form the northeastern radio relic. Both north and south mass peaks have better agreement with the morphology and position of the radio relic. Another scenario for the formation of the northeastern radio relic (but not the southeastern radio relic) could be that the more-massive subclusters merged with a large impact parameter. The location of the BCG and the western mass peak inside the west X-ray brightness peak is perplexing and goes against the expectation of ram pressure stripping for a dissociative merger. This configuration may occur at a later stage of merging while the subcluster is returning from apocenter. J. Merten et al. (2011) discussed a scenario in which a "ram pressure slingshot" effect has lead to the observed configuration of the X-ray emission and dark matter halo.

4.16. A3411 (z = 0.163)

A3411 has a notable radio relic that was first detected in G. Giovannini et al. (2013) and R. J. van Weeren et al. (2013). The relic is notable because it is connected by a radio bridge to a nearby radio galaxy (R. J. van Weeren et al. 2017). The bridge has a spectral index that steepens away from the radio galaxy and then flattens along the radio relic, which they suggest is evidence for shock reacceleration of the nonthermal population of charged particles that are seeded by the radio jet. F. Andrade-Santos et al. (2019) detected the shock at the relic location in deep Chandra observations and calculated a Mach number of $\lesssim$1.15. They estimated the mass of the cluster from X-ray observations to be $M_{500} = 7.1 \pm 0.7 \times 10^{14} M_{\odot}$. X. Zhang et al. (2020) analyzed deep XMM-Newton and Suzaku X-ray imaging and detected shocks in the southern edge and across the radio relic. Their X-ray temperature measurement of $T \sim 5$ keV gives a mass of

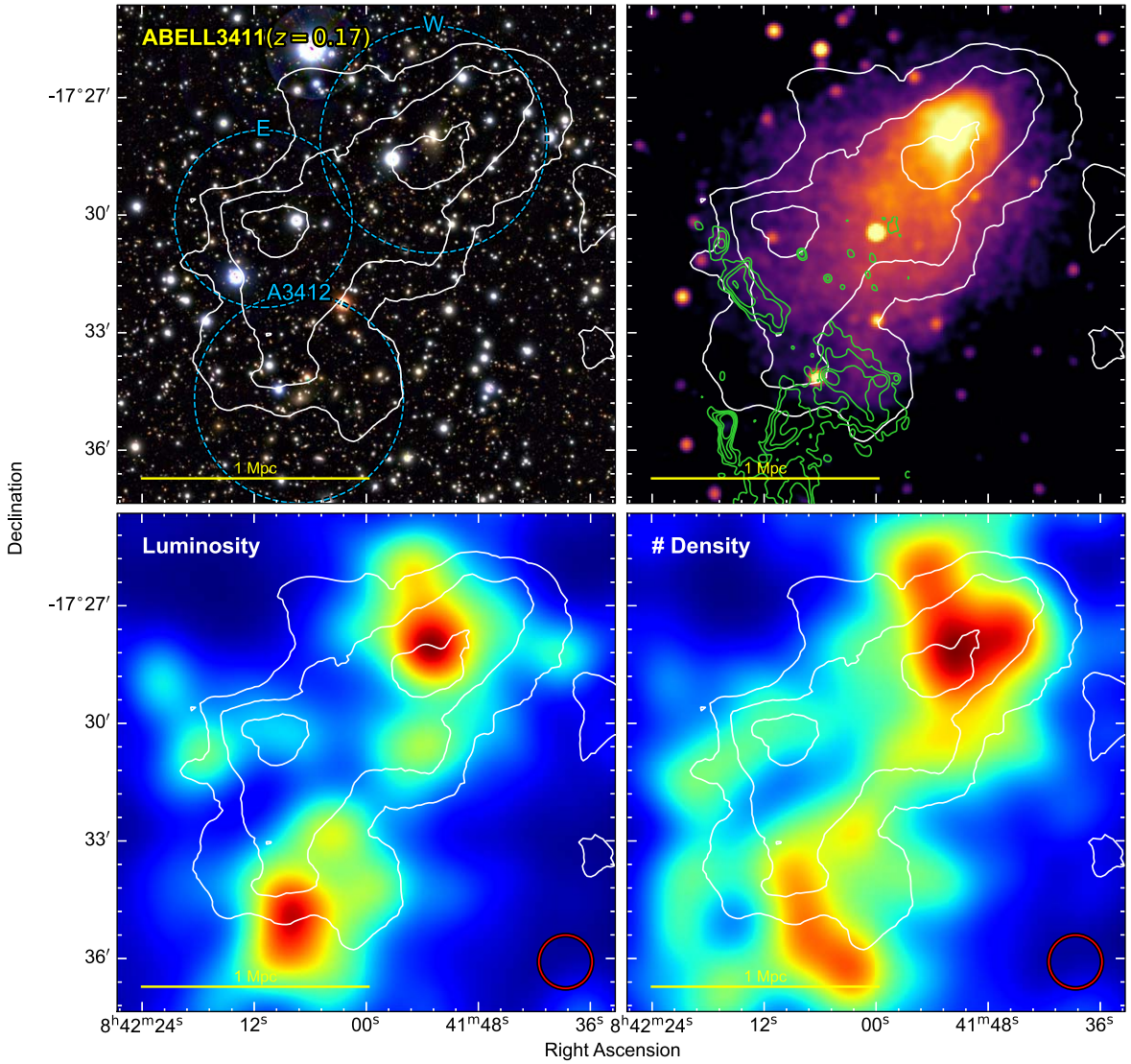

Figure 23. A3411. A merging system with a cool core and a connection between a radio galaxy and radio relic. WL contours increase in steps of 0.5σ. A3412 is detected at the 2.8σ level.

$M_{500} = 5.1 \times 10^{14} M_{\odot}$. G19 found that the galaxy distribution shows two populations with one centered on the BCG in the northwest and the other at A3412. The subclusters were found to have an equally high velocity dispersion of $\sim$1200 km s^{-1}.

WL result. The mass distribution of A3411 is marginally detected with S/N $\sim$ 3 (Figure 23). The mass distribution in the north peaks at the BCG and is elongated in the same direction as the X-ray distribution and toward the radio relic. Our WL analysis also detects A3412 but with low significance (peak S/N = 2.8). The A3412 WL detection is offset from the position that G19 detected the galaxy overdensity, but the offset is not statistically significant. Our mass estimates show that the western, eastern, and A3412 subclusters are $M_{200,\mathrm{W}} = 2.3 \pm 1.0 \times 10^{14}\, M_{\odot}$, $M_{200,\mathrm{E}} = 1.8 \pm 1.0 \times 10^{14}\, M_{\odot}$, and $M_{200,\mathrm{A3412}} = 1.1 \pm 0.8 \times 10^{14}\, M_{\odot}$, respectively.

Merger insight. The WL result presented in this work provides weak evidence for the subclusters that collided to create the shock presented in R. J. van Weeren et al. (2017). A merger between the eastern and western subclusters is the likely culprit. We do not expect A3412 to be the cause of the radio relic because of its position. New HSC observations (PI: H. Cho) have recently been completed and may provide an updated WL view of the massive structures in this galaxy cluster.

4.17. CIZA J2242.8+5301 (z = 0.189)

CIZAJ2242 (The Sausage Cluster) contains the textbook example of a radio relic (R. J. van Weeren et al. 2010) as well as radio relics to the south and east (see R. J. van Weeren et al. 2011a; A. Stroe et al. 2013, 2014a, 2014b, 2016; D. N. Hoang et al. 2017; F. Loi et al. 2017; G. Di Gennaro et al. 2018). The X-ray emission is elongated in the north–south direction with two peaks and an extension that stretches to the north. Shocks have been detected in X-rays at the location of the northern and southern radio relics as well as to the east (G. A. Ogrean et al. 2013a, 2014b; H. Akamatsu et al. 2015). The archetypal relic in the north has spurred many simulations to attempt to recreate its properties as well as other ICM properties and features (S. Matsukiyo et al. 2011; R. J. van Weeren et al. 2011a; H. Kang et al. 2012; Y. Fujita et al. 2015; H. Kang & D. Ryu 2015; H. Kang 2016b; Y. Fujita et al. 2016; J. M. F. Donnert et al. 2016; J. M. F. Donnert et al. 2017;

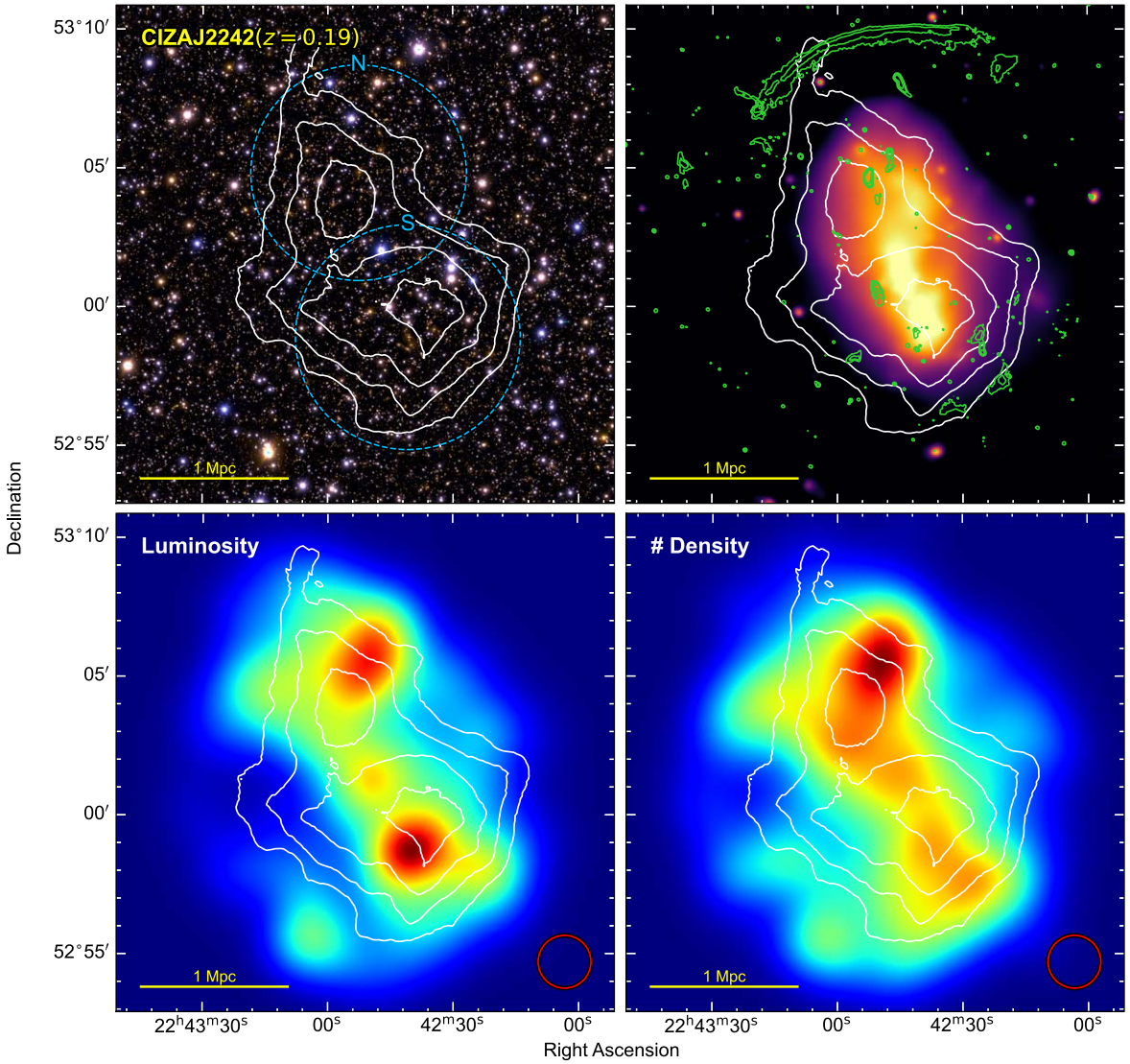

Figure 24. CIZAJ2242 (The Sausage Cluster). A system with a textbook, arc-shaped radio relic, complex X-ray emission, and a bimodal mass distribution. WL contours increase in steps of 1σ.

S. M. Molnar & T. Broadhurst 2017). In addition, from SZ observations, C. Rumsey et al. (2017) found a high-pressure region that stretches perpendicular to the elongated X-ray emission. W. A. Dawson et al. (2015) found the cluster galaxies to follow a bimodal distribution with close to equal velocity dispersion, which suggests equal-mass subclusters.

Two previous WL analyses have been performed on CIZA2242. N. Okabe et al. (2015) and M. J. Jee et al. (2015) both mapped the WL signal of the Sausage cluster and found it to be bimodal. Both authors found nearly equal mass ratios for the merger when simultaneously fitting the subclusters with A. R. Duffy et al. (2008) *c*–*M* models. M. J. Jee et al. (2015) determined the masses of the northern and southern subclusters to be $M_{200} = 11.0^{+3.7}_{-3.2} \times 10^{14}\,M_{\odot}$ and $M_{200} = 9.8^{+3.8}_{-2.5} \times 10^{14}\,M_{\odot}$, respectively. N. Okabe et al. (2015) found the subclusters to have masses of $M_{200} = 5.51^{+6.39}_{-3.43} \times 10^{14}\,M_{\odot}$ and $M_{200} = 10.69^{+9.82}_{-5.67} \times 10^{14}\,M_{\odot}$ for the northern and southern subclusters, respectively.

WL result. We utilize the M. J. Jee et al. (2015) shape catalog for our analysis, which unsurprisingly results in a similar mass map (Figure 24) to M. J. Jee et al. (2015). Fitting two NFW halos, we estimate a mass of $M_{200,\mathrm{N}} = 8.2 \pm 1.8 \times 10^{14}\,M_{\odot}$ and $M_{200,\mathrm{S}} = 9.3 \pm 1.8 \times 10^{14}\,M_{\odot}$, which are consistent with M. J. Jee et al. (2015) and N. Okabe et al. (2015).

Merger insight. The morphology and features of the X-ray emission from CIZA2242 are not as expected for a 1:1 mass ratio merger of two massive clusters, as pointed out by G. A. Ogrean et al. (2013a). The brightest X-ray emission is located near the BCG in the south. A second brightness peak is located approximately 0.5 Mpc to the north, and then an extension snakes 1 Mpc farther to the north. The complexity of the features suggests that additional subclusters are likely to exist. CIZAJ2242 is a dissociative merger with similarity to MACSJ1752 and ZwCl1856. An additional mystery is that the mass peaks in the north and south show offsets from their respective BCGs. The mystery may arise because ground-based WL cannot resolve such substructures and provide a poor constraint on the mass peaks because of the high extinction and stellar density of the zone of avoidance. High-resolution imaging is required to achieve the number density of source galaxies that is needed to constrain the mass peak positions and to resolve substructures.

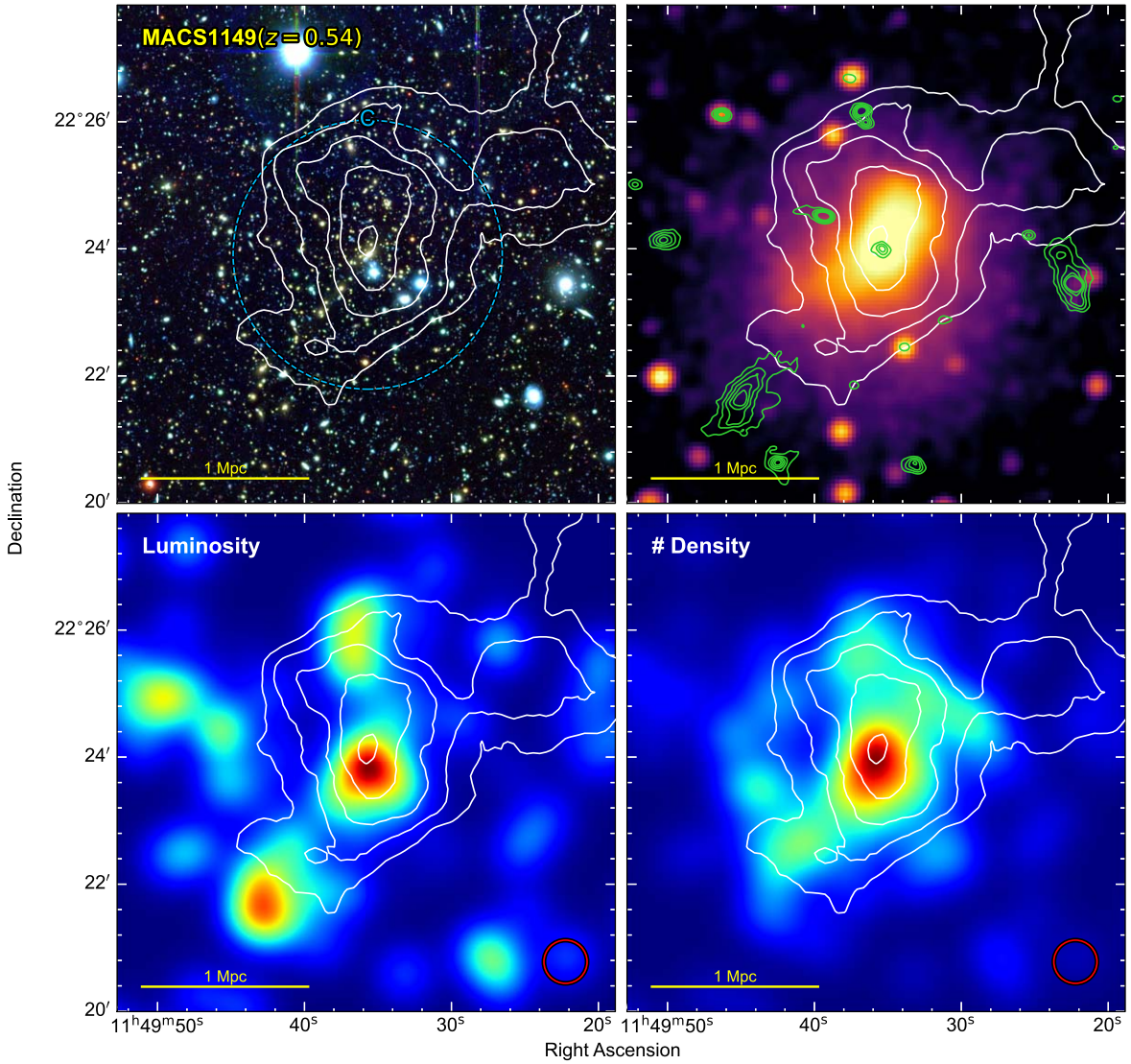

Figure 25. MACSJ1149. A high-z cluster with a north–south elongation in the mass and X-ray distributions. WL contours increase in steps of 0.5σ.

4.18. MACS J1149.5+2223 (z = 0.544)

MACSJ1149 is the highest-redshift cluster in the sample. A. Bonafede et al. (2012) pointed out two radio relic candidates in the system, but one was shown to be a radio galaxy (G. Giovannini et al. 2020; L. Bruno et al. 2021). It is one of the most X-ray luminous and hottest ($T = 10.73^{+0.62}_{-0.43}$ keV) clusters known (G. A. Ogrean et al. 2016). G19 found the cluster to have an extreme velocity dispersion of $1668 \pm 76\,\mathrm{km\,s^{-1}}$. G19 separated the cluster galaxies into three subclusters with a primary cluster at the BCG location, a subcluster to the southeast, and a smaller subcluster directly north of the BCG. Their GMM analysis found that the north subcluster is at $z = 0.56$, which may suggest significant line-of-sight motion.

The WL analysis of Subaru observations (K. Umetsu et al. 2014) detected the primary cluster and an elongated WL signal that stretches southeast from the BCG. A joint SL–WL analysis on HST images (E. Q. Finney et al. 2018) presented an elongated distribution that runs from the BCG to the north and to the southeast. K. Umetsu et al. (2014) estimated the total mass of the cluster to be $25.4 \pm 5.2 \times 10^{14}\,M_{\odot}$.

WL result. Our WL mass reconstruction (Figure 25) has a peak directly on the BCG. The mass distribution is elongated to the north of the BCG and encompasses the second BCG in similar fashion to the WL–SL analysis of E. Q. Finney et al. (2018). As was found in K. Umetsu et al. (2014), the mass extends southeast from the BCG, but no clear peak is detected. Our mass map also detects an extension to the northwest of the cluster that has a weak agreement with galaxy luminosity. Since no clear subclusters are detected, we fit a single NFW halo and find the mass to be $M_{200} = 16.4 \pm 3.1 \times 10^{14}\,M_{\odot}$, which is marginally lower than the mass estimate from K. Umetsu et al. (2014).

Merger insight. The low-significance substructures that are detected in our WL analysis do not provide additional evidence to the origin of the radio relic. As L. Bruno et al. (2021) pointed out, the orientation of the relic and the mass distribution is difficult to reconcile.

4.19. MACS J1752.0+4440 (z = 0.365)

A multiwavelength analysis of MACSJ1752 is presented in K. Finner et al. (2021). MACSJ1752 contains two bright and extended radio relics (A. Bonafede et al. 2012; R. J. van Weeren et al. 2012a). The radio relics are arc shaped and on opposing ends of the elongated X-ray distribution.

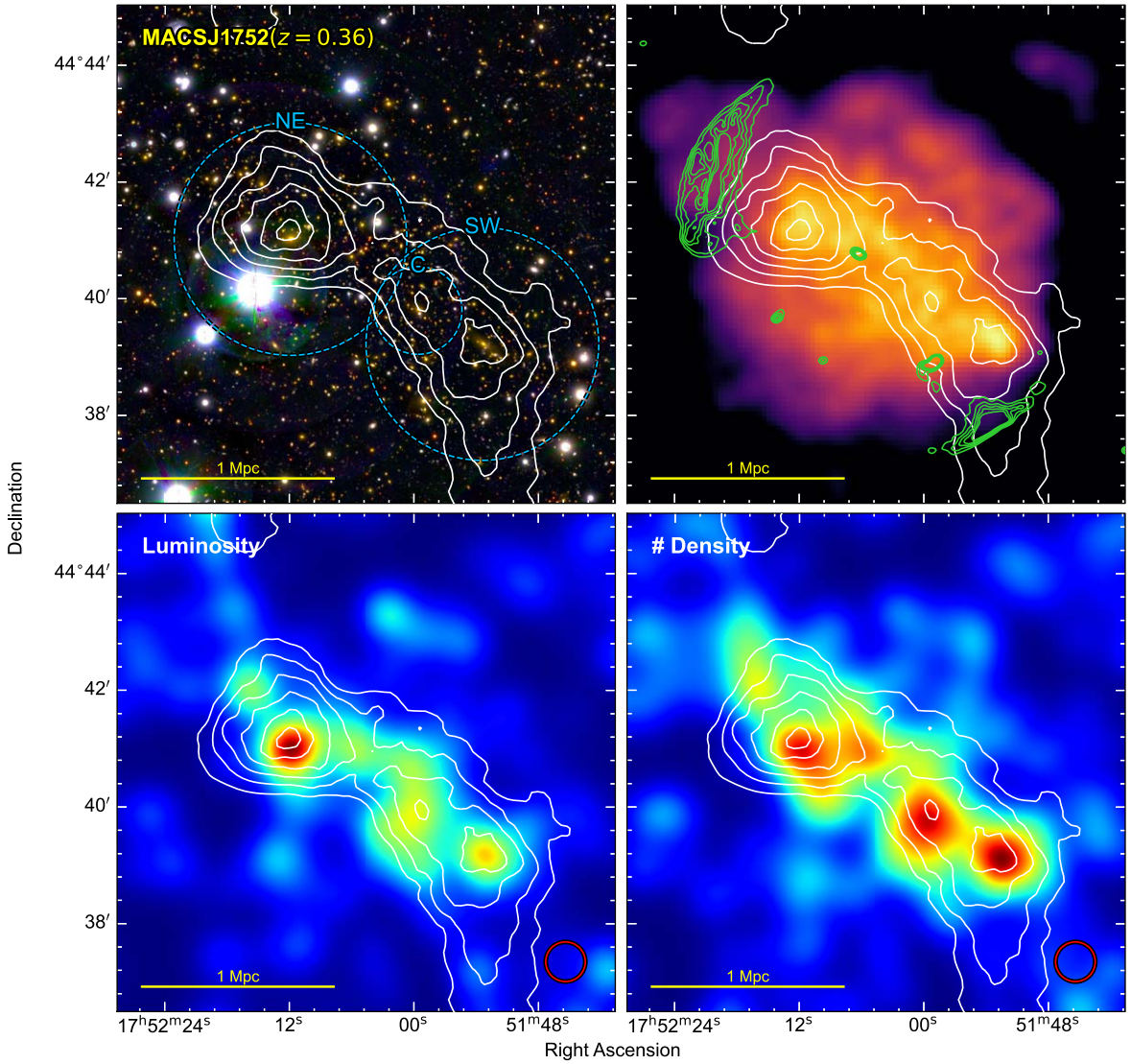

Figure 26. MACSJ1752. An equal-mass merger with ram-pressure-stripped tails in the X-ray emission and double radio relics. WL contours increase in steps of 1σ.

F. de Gasperin et al. (2015) pointed out the extreme luminosity of the radio relics in MACSJ1752. The X-ray emission is double peaked with a bridge running between the peaks. K. Finner et al. (2021) showed that these two X-ray brightness peaks are the sites of cold fronts. The elongated shape of the X-ray distribution resembles an "S" and is evidence of a small impact parameter collision. As a textbook example of a galaxy cluster merger, the cluster has been utilized in simulations to test the mass bias of WL (W. Lee et al. 2023) and cosmic-ray acceleration (F. Vazza et al. 2016).

WL result. In K. Finner et al. (2021), our WL detection (Figure 26) revealed two mass peaks that coincide with the BCGs and X-ray peaks. In addition, we found a third substructure between the peaks that coincides with the third brightest galaxy and an X-ray peak. Our mass estimates show that the northeastern and southwestern subclusters have masses of $M_{200,\mathrm{NW}} = 5.6 \pm 1.8 \times 10^{14}\,M_{\odot}$ and $M_{200,\mathrm{SE}} = 5.6 \pm 1.7 \times 10^{14}\,M_{\odot}$. The central substructure is low mass with $M_{200,\mathrm{C}} = 0.3^{+0.4}_{-0.1} \times 10^{14}\,M_{\odot}$.

Merger scenario. The merger scenario of MACSJ1752 appears to be straightforward. MACSJ1752 is among the most-massive binary mergers in the sample. As shown in many idealized cluster simulations, a low impact parameter merger between equal-mass subclusters can recreate the observed X-ray morphology features such as the "S" shape and cold fronts. The radio relics are not perfectly symmetric but are among the cleanest example of double relics. An intriguing connection between a galaxy and the southern radio relic is noted in the WSRT observation in K. Finner et al. (2021), but further spectral analysis is needed to see if it supports the reacceleration mechanism.

4.20. PLCK G287.0+32.9 (z = 0.385)

PLCKG287 is one of the more unusual clusters in the sample. The cluster has an X-ray distribution that contains only a single peak and is somewhat relaxed in appearance with a hint of an extension toward the southeast. The global temperature of the cluster is 13 keV, and it is the second most massive cluster ($26 \pm 1 \times 10^{14}\,M_{\odot}$) in the Planck catalog (Planck Collaboration et al. 2016). There are a few tens of strong-lensing arcs found around the BCG, and the cluster is one of the largest strong lenses in the Universe that has been detected to date. G19 found the velocity dispersion of the cluster to be $1756 \pm 74\,\mathrm{km\,s^{-1}}$, the highest in this radio relic

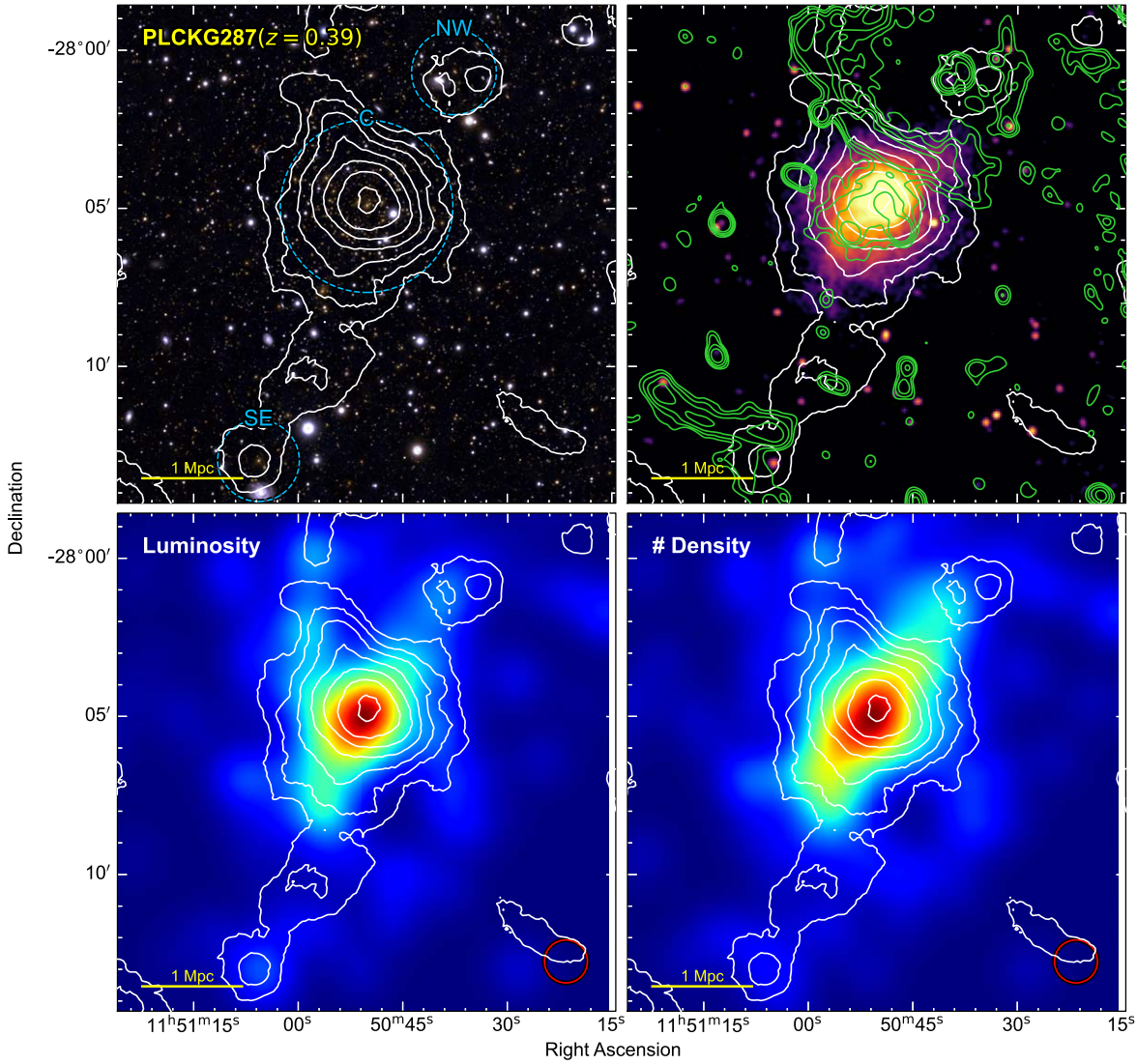

Figure 27. PLCKG287. A centrally dominant, massive cluster with low-mass subclusters and double radio relics at asymmetric projected separation. WL contours increase in steps of 1σ.

sample. Their analysis of the cluster galaxies separated the cluster into a massive primary with a secondary ∼2.5 Mpc to the south. It has two radio relics that are vastly different distances from the X-ray peak (J. Bagchi et al. 2011; A. Bonafede et al. 2014) and separated by about 3 Mpc. A. Bonafede et al. (2014) showed that the galaxy distribution follows a northwest–southeast layout and is likely a filament that is feeding the massive cluster.

D. Gruen et al. (2014) mapped the cluster with the MPG/ESO telescope Wide-Field Imager and detected the WL signal near the BCG. They fit an NFW model and determined the cluster to have a mass of $M_{200,C} = 3.0 \pm 0.8 \times 10^{15}\,M_{\odot}$.

WL result. Published in K. Finner et al. (2017), the WL signal of PLCKG287 is dominated by a central cluster with a mass peak that has excellent agreement with the BCG and the X-ray brightness peak (Figure 27). Two additional subclusters are detected that lie along a northwest–southeast axis. A three-halo fit to the mass distribution finds $M_{200,C} = 20.4 \pm 1.9 \times 10^{14}\,M_{\odot}$, $M_{200,SE} = 1.7 \pm 0.7 \times 10^{14}\,M_{\odot}$, and $M_{200,NW} = 1.4 \pm 0.7 \times 10^{14}\,M_{\odot}$. The mass from our three-halo fit is consistent with the total mass measured in D. Gruen et al. (2014).

Merger insight. It is expected that either one of the substructures merged to form both relics on two passages or that each of the two substructures were responsible for a relic. A. Bonafede et al. (2014) estimated the time since collision (pericenter) for each of the relics to be approximately 0.7 and 0.1 Gyr for the south and north radio relics, respectively. The BCG in the cluster has a nearly equally bright, nearby companion that may be valuable in interpreting the merger. It is also worth noting that the third BCG, which is ∼1 Mpc southeast of the BCG, does not have a WL peak.

4.21. PSZ1 G108.2-11.53 (z = 0.335)

PSZG108 is a double radio relic cluster with a very large relic separation (∼3.5 Mpc). G19 identified two galaxy populations that are near the central point between the relics. However, only 40 galaxies had available redshifts, and their GMM did not separate the galaxies into two subclusters. The X-ray emission in PSZG108 peaks near the BCG and is elongated along the axis that connects the radio relics. The second brightest galaxy is ∼1.5 Mpc to the northeast of the BCG and is coincident with the northern radio relic. The radio

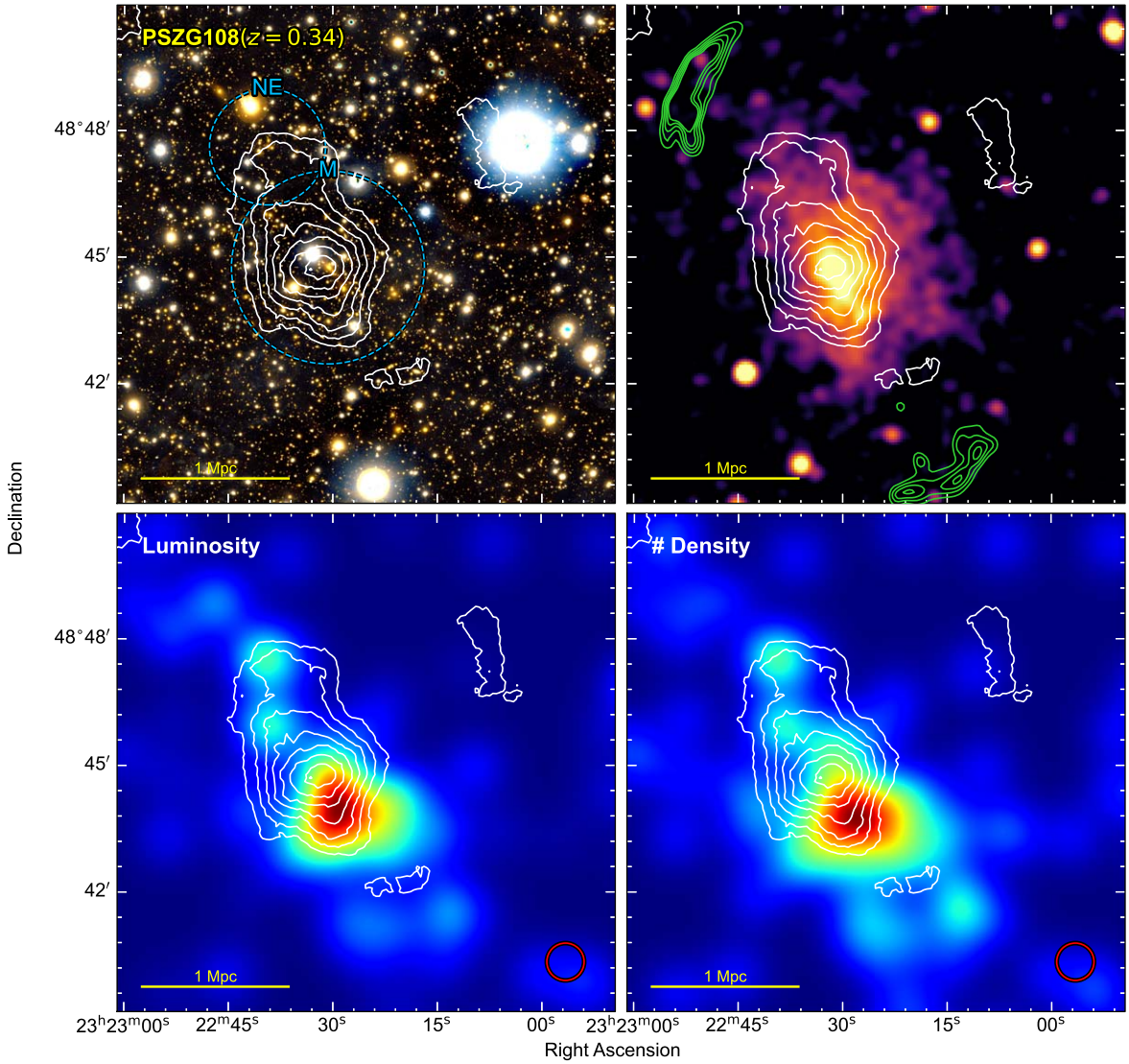

Figure 28. PSZ1G108. A centrally dominant cluster with large separation double radio relics. WL contours increase in steps of 0.5σ.

relics of PSZG108 are two of the most powerful found to date (F. de Gasperin et al. 2015).

WL result. We analyzed the Subaru HSC observations of PSZG108. Our WL mass reconstruction (Figure 28) detects the signal with a main peak that is coincident with the BCG. The WL signal elongates toward the northeast, following a similar distribution to the X-ray emission. The significant WL signal terminates at a galaxy overdensity that we consider the northeastern subcluster. We note that the second BCG is farther to the northeast. The WL signal also extends slightly to the southwest where many of the bright cluster galaxies reside. We fit a two-halo NFW model and find the subcluster masses to be $M_{200,\mathrm{C}} = 6.9 \pm 2.1 \times 10^{14}\,M_{\odot}$ and $M_{200,\mathrm{NE}} = 1.5 \pm 1.2 \times 10^{14}\,M_{\odot}$.

Merger insight. The double-relic nature of PSZG108 can be used to constrain the merger axis to be approximately northeast to southwest. The X-ray emission and WL signal are elongated in the same direction. One scenario for the formation of the radio relics is a collision between the two subclusters that are detected in WL, which would have a mass ratio $\gtrsim$1:4. The large separation of the radio relics suggests a long time has passed since the collision if the shocks propagate at a constant velocity (J.-H. Ha et al. 2018). Close analysis of the HSC observations reveals that the BCG has many bright companion cluster galaxies (as is apparent from the luminosity and number density maps). An alternative scenario is that the collision that formed the radio relics occurred far enough in the past that the two subclusters are both situated in the BCG region. WL analysis would require a higher number density of galaxies to resolve subclusters in this region. Follow-up observations with the HST or JWST would be valuable for SL–WL analysis of the cluster. There are large blue arcs at the core of the cluster that are likely strong-lensing images.

4.22. RXC J1314.4–2515 (z = 0.247)

RXCJ1314 is the second example of a two radio relic cluster that has a distinct difference in the distance of the radio relics from the barycenter of the subclusters (like PLCKG287). The imbalanced radio relic distribution could be caused by two merging events or it could also be a projection effect (for recent radio work, see C. Stuardi et al. 2019). A shock was detected in XMM-Newton observations at the location of the western relic (P. Mazzotta et al. 2011). G19 concluded that the member galaxies follow two

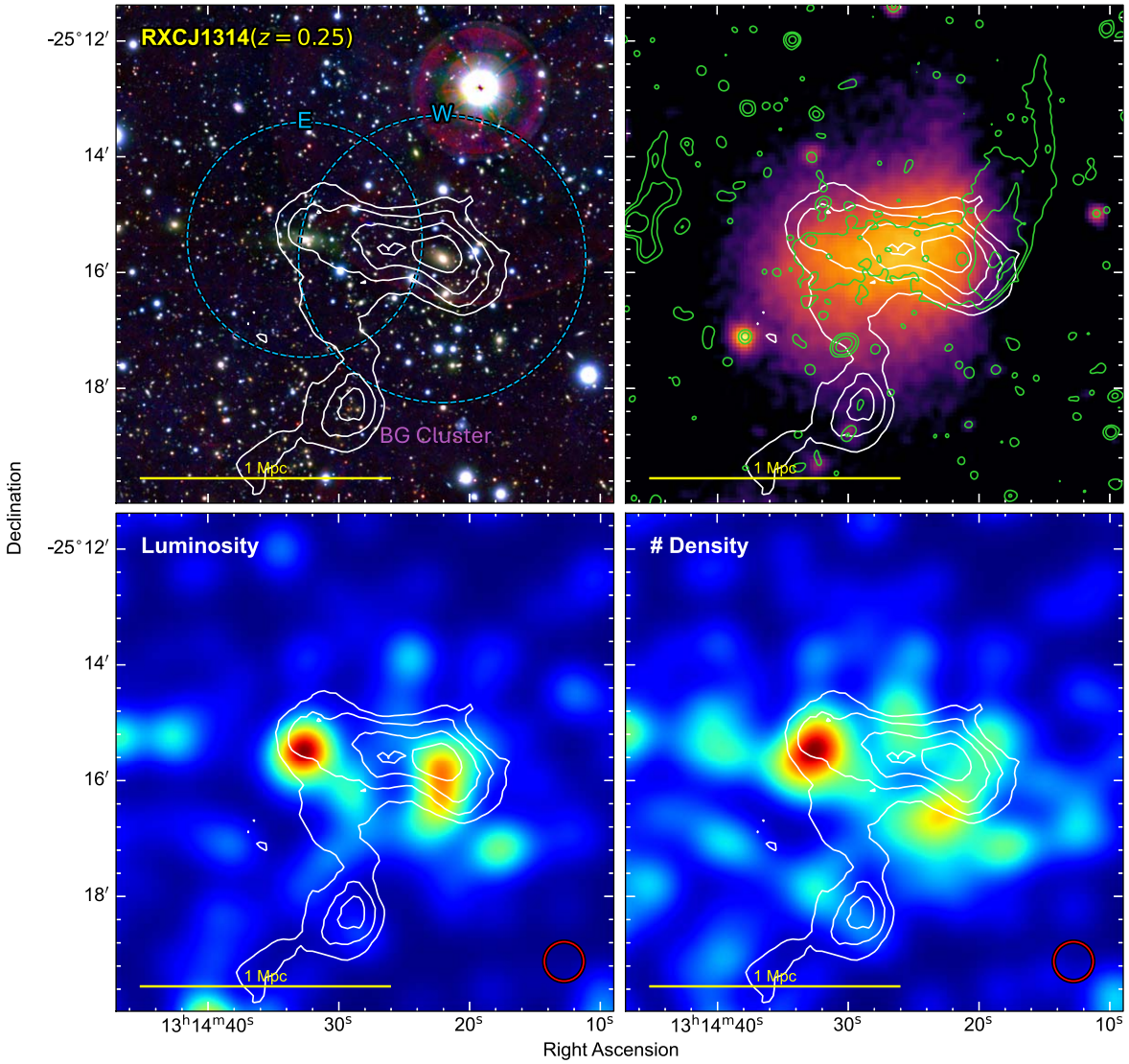

Figure 29. RXCJ1314. A merging system with a possibly large viewing angle and radio relics at asymmetric projected separation. WL contours start at 3σ and increase in steps of 0.5σ. A candidate background cluster (BG Cluster) is detected in the south with a spectroscopically confirmed $z = 0.47$ galaxy in the center of the mass contours.

Gaussian distributions with a $\sim$1500 km s^{-1} LOS velocity difference. Therefore, projection effects are important to consider for RXCJ1314. C. Stuardi et al. (2019) came to a similar conclusion from vastly different rotation measures from the two radio relics and found that simulations suggest a 70° departure from the plane of sky. Nevertheless, the axis connecting the radio relics agrees with the elongated X-ray emission and defines a probable merging axis. The cluster was also recently observed with MeerKAT (K. Knowles et al. 2022), which is presented in Figure 29.

WL result. The WL mass map (Figure 29) is elongated along the projected merger axis. The W mass peak is dominant and coincides with the BCG. The eastern mass peak is spatially consistent with the second BCG, and a third mass clump is detected to the south. It is unclear whether this third mass peak is at the redshift of the cluster or is background. In the center of the third mass peak is a galaxy that was measured to have a spectroscopic redshift of 0.47 (N. Golovich et al. 2019a). A two-halo fit to the western and eastern subclusters finds a 2:1 mass ratio with masses of $M_{200,\mathrm{W}} = 4.2 \pm 1.3\ M_{\odot}$ and $M_{200,\mathrm{E}} = 2.3 \pm 1.0 \times 10^{14}\ M_{\odot}$. If we include the third mass clump ($z = 0.47$) in the fit, the masses change to $M_{200,\mathrm{W}} = 3.0 \pm 1.2 \times 10^{14}\ M_{\odot}$, $M_{200,\mathrm{E}} = 1.8 \pm 0.9 \times 10^{14}\ M_{\odot}$, and $M_{200,\mathrm{BG}} = 1.9 \pm 0.8 \times 10^{14}\ M_{\odot}$.

Merger insight. The X-ray emission, galaxies, and WL signal offer a simple merger geometry between the eastern and western subclusters. Similar to PLCKG287, the two radio relics that are at different distances are difficult to explain. One possibility is that the relics formed through a first and second passage of two subclusters. However, the timescale for two passes is long. Another possibility is that the relics formed from three subclusters. Our WL analysis does not detect a third subcluster at the relevant redshift. Therefore, it becomes more difficult to invoke the three-subcluster scenario to explain the relic distances.

4.23. ZwCl 0008.9+5215 (z = 0.104)

ZwCl0008 is another merging cluster with double radio relics (R. J. van Weeren et al. 2011c). The double relics are quite different from each other, with the largest linear size of the east relic 3 times bigger than the west. A similar discrepancy is found in the Sausage relics. ZwCl0008 exhibits

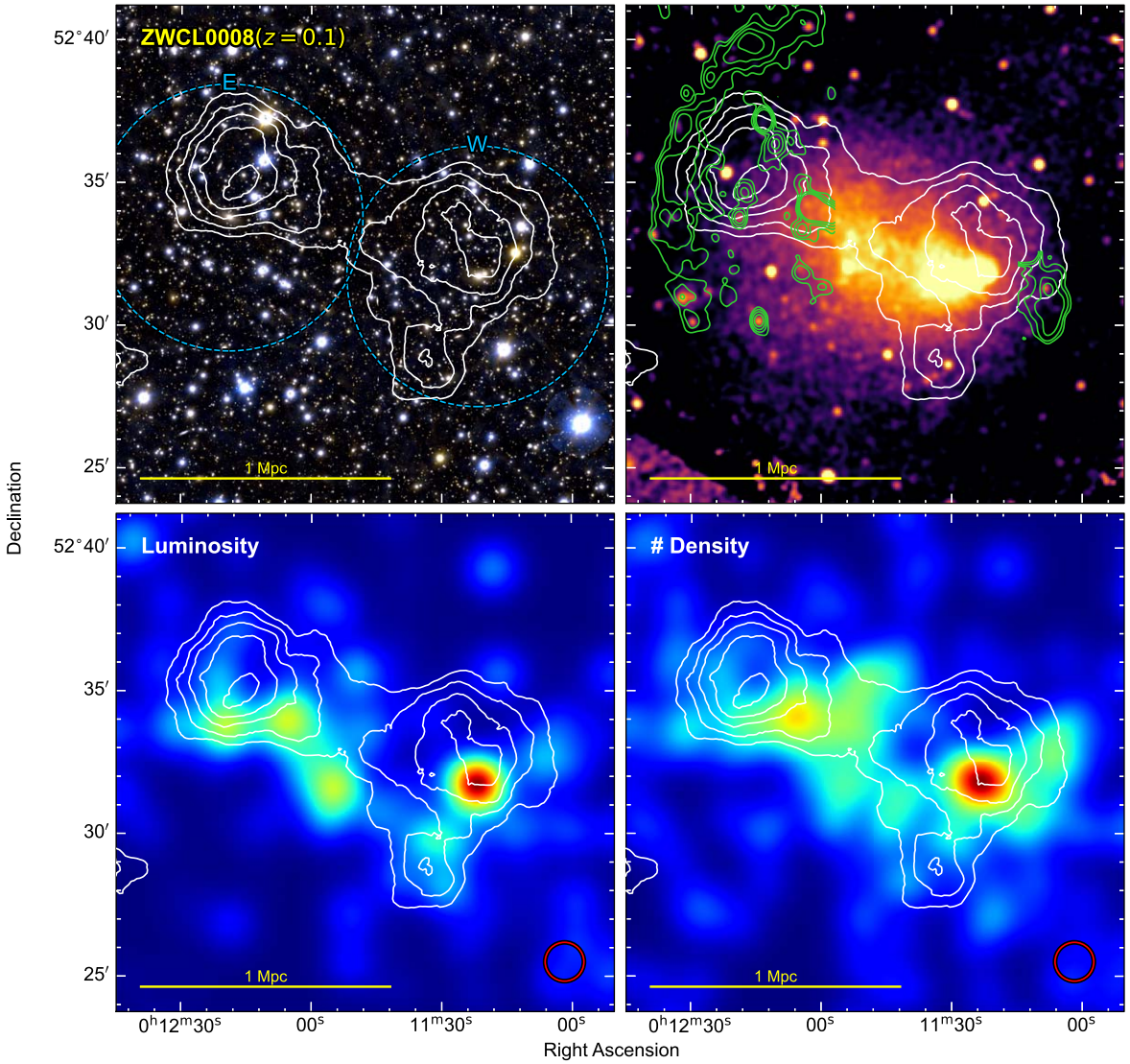

Figure 30. ZwCl0008. A dissociative merger of equal-mass subclusters. WL contours increase in steps of 0.5σ.

a bullet-shaped morphology in the ICM (N. Golovich et al. 2017). It also has a very short radio relic standoff distance (for a discussion of the standoff distance, see C. Zhang et al. 2019). These two features are signs of a recent merger. The spectroscopic observations of G19 suggest a cluster merger closer to a 1:1 mass ratio. From Chandra and Suzaku observations, G. Di Gennaro et al. (2019) detected a shock at the western radio relic and measured a Mach number of 1.5 ± 0.5. They found no shock at the location of the eastern relic. H. Kang et al. (2012) simulated the collision and showed that the radio relic agrees with the combination of DSA and reacceleration. S. M. Molnar & T. Broadhurst (2018) predicted that the cluster merger is an off-axis binary merger that is viewed shortly after first core passage.

A WL analysis of the cluster was done with HST and Subaru imaging in N. Golovich et al. (2017), finding that the eastern subcluster is four times more massive than the western subcluster. Their mass estimates are $5.7^{+2.8}_{-1.8} \times 10^{14}\,M_{\odot}$ and $1.2^{+1.4}_{-0.6} \times 10^{14}\,M_{\odot}$ for the eastern and western subclusters, respectively.

WL result. Our WL analysis on solely the Subaru imaging detects the two subclusters (Figure 30). Using our multiple NFW halo fitting technique, we find that the mass ratio is close to 1:1 with the eastern and western subcluster masses being $M_{200,\mathrm{E}} = 2.9 \pm 0.8 \times 10^{14}\,M_{\odot}$ and $M_{200,\mathrm{W}} = 2.7 \pm 0.8 \times 10^{14}\,M_{\odot}$, both of which are in statistical agreement with N. Golovich et al. (2017). In addition to the detection of the two subclusters, an elongation of the WL signal from the western subcluster toward the south is found. This detection is coincident with another bright cluster galaxy. Comparing the WL signal to the galaxy luminosity and number density distributions shows that there is likely another substructure.

Merger insight. The merger scenario for ZwCl0008 is straightforward with a collision between two subclusters. The X-ray emission shows morphological features that suggest a small impact parameter. The short standoff distance of the radio relics is expected for a system that is observed shortly after collision. ZwCl0008 is a great candidate for constraining the properties of dark matter.

4.24. ZwCl 1447+2619 (z = 0.376)

ZwCl1447 is an H. R. Butcher & A. J. Oemler (1984) galaxy cluster that has a poorly defined red sequence. Recent Chandra observations revealed a double clump ICM distribution with a

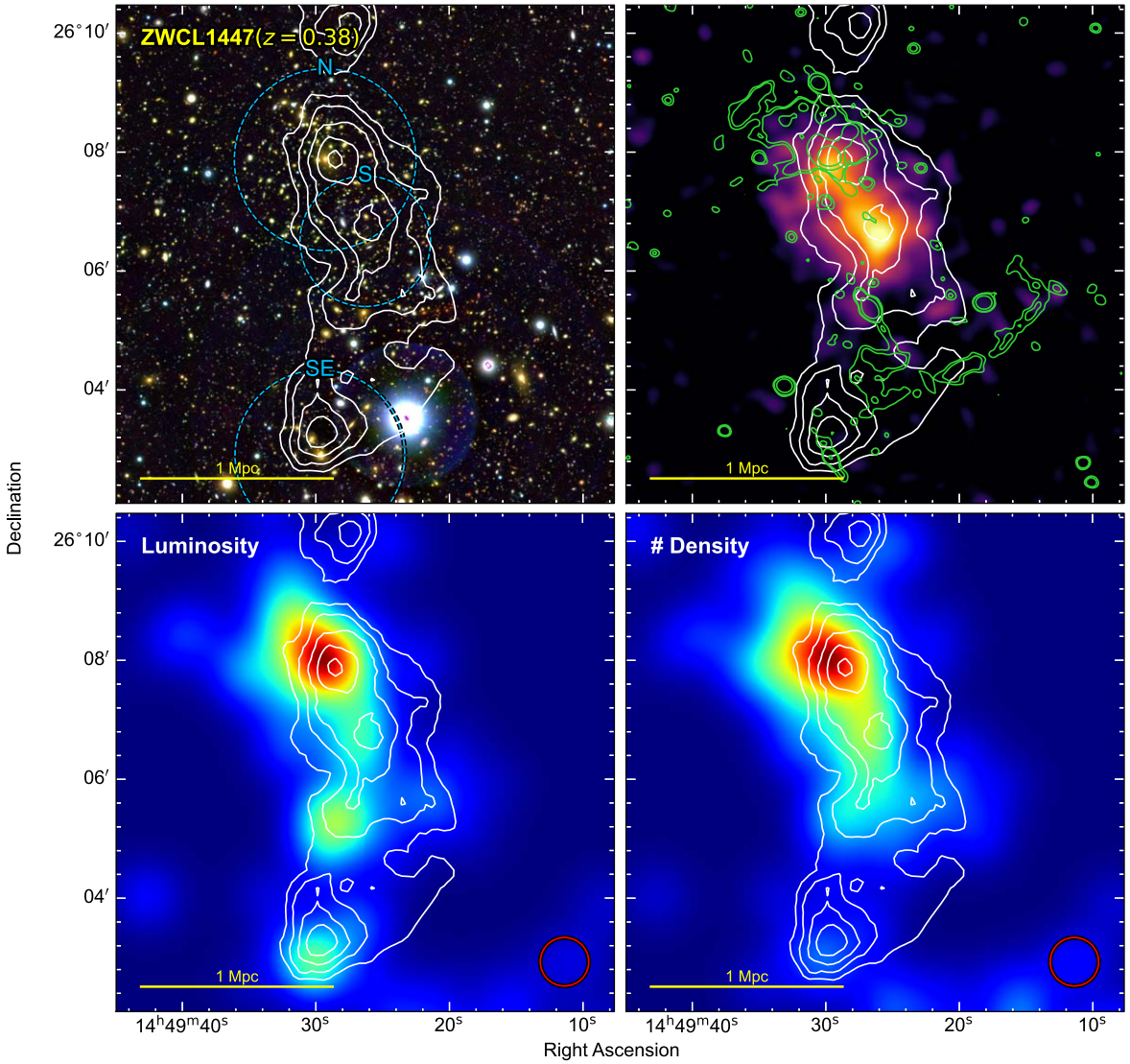

Figure 31. ZwCl1447. A merging system with double radio relics. WL contours start at 3σ and increase in steps of 0.5σ.

small (∼500 kpc) separation between the subclusters (W. Lee et al. 2022). G. Giovannini et al. (2009) analyzed VLA 1.4 GHz data and discovered a radio relic to the south of the cluster. They also found a radio relic candidate in the north, but were undecided on whether it is a relic or halo. However, recent GMRT observations by W. Lee et al. (2022) have highlighted that the diffuse radio emission in the north is indeed a radio relic. They showed that the relic in the south is a textbook example of a bow shock (like the Sausage relic). In addition, they ruled out radio halo emission. G19 were unable to divide the spectroscopically confirmed cluster member galaxies into multiple distributions.

WL result. The WL analysis (Figure 31) for this cluster was first presented in W. Lee et al. (2022). We find that the WL signal consists of three distinct peaks. Two of the peaks are coincident with the X-ray brightness peaks. A third peak is located about 1 Mpc to the southeast of the BCG and is associated with the second brightest galaxy in the region. As shown in Figure 31, there is good agreement between galaxies and mass distribution in this cluster. The southeastern mass peak that is coincident with the second brightest galaxy in the field has no X-ray detection. One reason may be from the chip gap of the Chandra detector. A second reason may be that the gas has been stripped from a past merger with the primary cluster. Better planned X-ray observations would be useful for understanding the nature of the southeastern substructure. There is also a fourth WL peak to the north of the northern subcluster, but there is no evidence of a subcluster in X-ray or galaxy light. We choose to fit a three-halo model and find masses of $M_{200,\mathrm{N}} = 2.7 \pm 0.8 \times 10^{14}\,M_{\odot}$, $M_{200,\mathrm{S}} = 1.0 \pm 0.5 \times 10^{14}\,M_{\odot}$, and $M_{200,\mathrm{SE}} = 2.2 \pm 0.7 \times 10^{14}\,M_{\odot}$.

Merger scenario. The alignment of the two subclusters in the north is in great agreement with the radio relics. We suggest that these are the subclusters that merged to form the shocks. Furthermore, the radio relic in the south has a very uniform arc shape that may be indicating a head-on collision. The location of the southeastern mass peak suggests that it has not been involved in the merger, especially since it lies ahead of the radio relic. However, it is peculiar to not detect any X-ray emission from it. For detailed simulations of the cluster merger, see W. Lee et al. (2022).

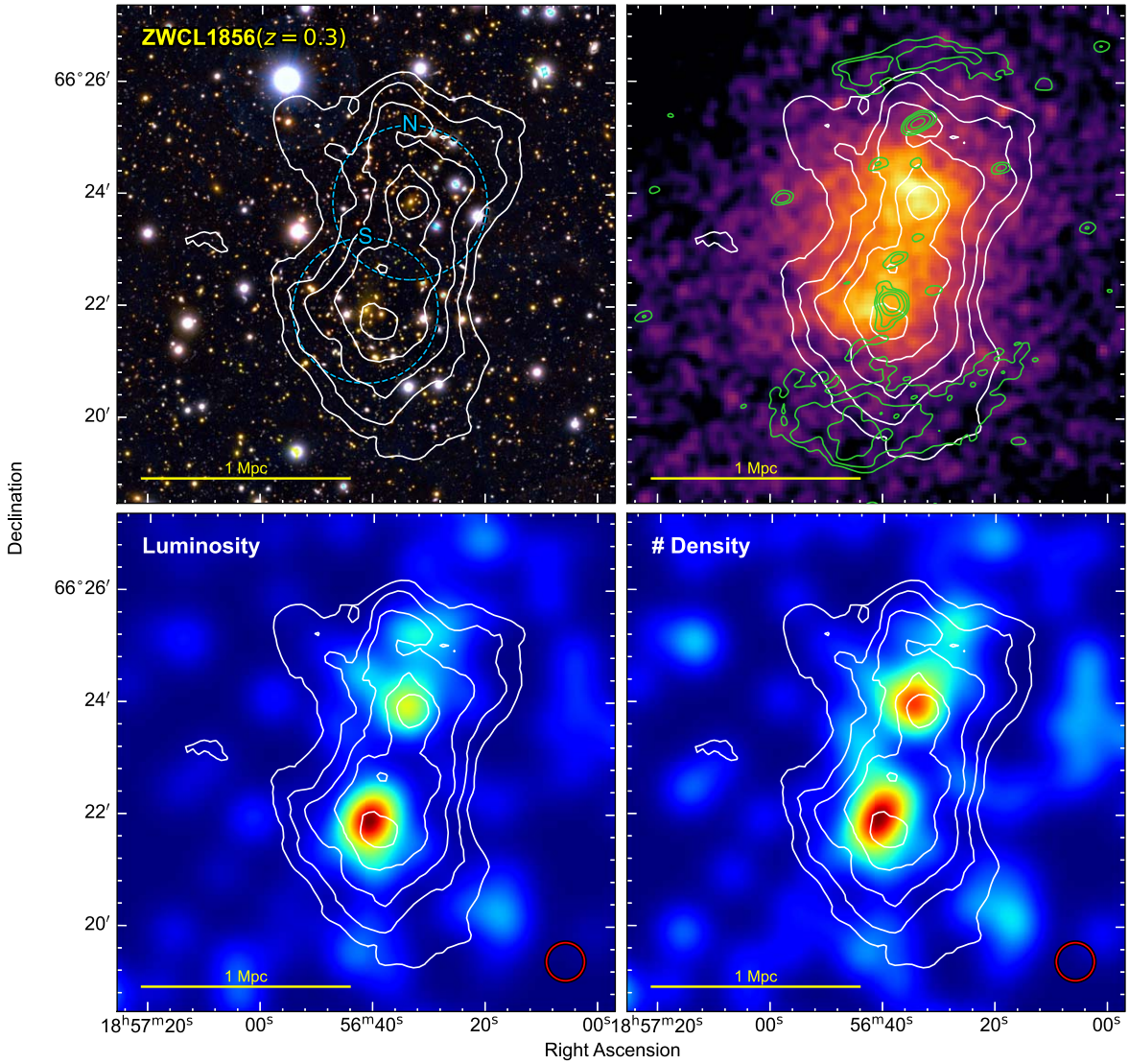

Figure 32. ZwCl1856. An equal-mass merger with low total mass and double radio relics. WL contours increase in steps of 0.5σ.

4.25. ZwCl 1856.8+6616 (z = 0.334)

ZwCl1856 is a pristine example of double radio relics that are nearly equal in shape, size, distance from the center, and orientation. The relics were first presented in F. de Gasperin et al. (2014) and further analyzed in A. Jones et al. (2021). Similar to MACSJ1752, the radio relics are found at opposing ends of an S-shaped X-ray morphology. However, in comparison to MACSJ1752, the location of the relics is in better agreement with the merger axis, being directly in line with the elongated X-ray. A. Jones et al. (2021) also detected a radio bridge (connection) between the southern radio relic and the southern BCG. G19 were able to separate the cluster galaxies into two populations of nearly equal velocity dispersion and suggested an equal-mass merger.

WL result. The WL analysis (Figure 32) of ZwCl1856 is presented in K. Finner et al. (2021). The mass distribution is dominated by two mass peaks that agree with their respective BCGs and align along the merger axis that is defined by the radio relics. A signature of a third, lower significance peak is found to the north, which is located near the northern radio relic. We found the northern and southern subclusters to have masses of $M_{200,\mathrm{N}} = 1.6 \pm 0.8 \times 10^{14}\,M_{\odot}$ and $M_{200,\mathrm{S}} = 1.5 \pm 0.7 \times 10^{14} M_{\odot}$, respectively. Intriguingly, ZwCl1856 is a low-mass binary merger that hosts bright radio relics. The low mass is in agreement with the expected mass from our XMM-Newton temperature estimate of $3.6^{+0.6}_{-0.5}$ keV (K. Finner et al. 2021).

Merger insight. The S-shaped X-ray morphology suggests a merger with a small impact parameter. The mass peaks in both the north and south are slightly inside the X-ray brightness peaks, which could indicate that the cluster is near apocenter and the ICM has been slingshot through the potential. However, this interpretation, which is based on poor X-ray observations, should be remedied soon, with upcoming deeper Chandra observations. MACSJ1752 and ZwCl1856 provide two examples of simple cluster mergers that have much different masses but host bright radio relics.

4.26. ZwCl 2341+0000 (z = 0.27)

The ICM of ZwCl2341 is rich in merging features. R. J. van Weeren et al. (2009) found double radio relics, which were verified in G. Giovannini et al. (2010) and V. Parekh et al. (2022). The polarization properties of the radio relics of ZwCl2341 were also studied in C. Stuardi et al. (2022). The

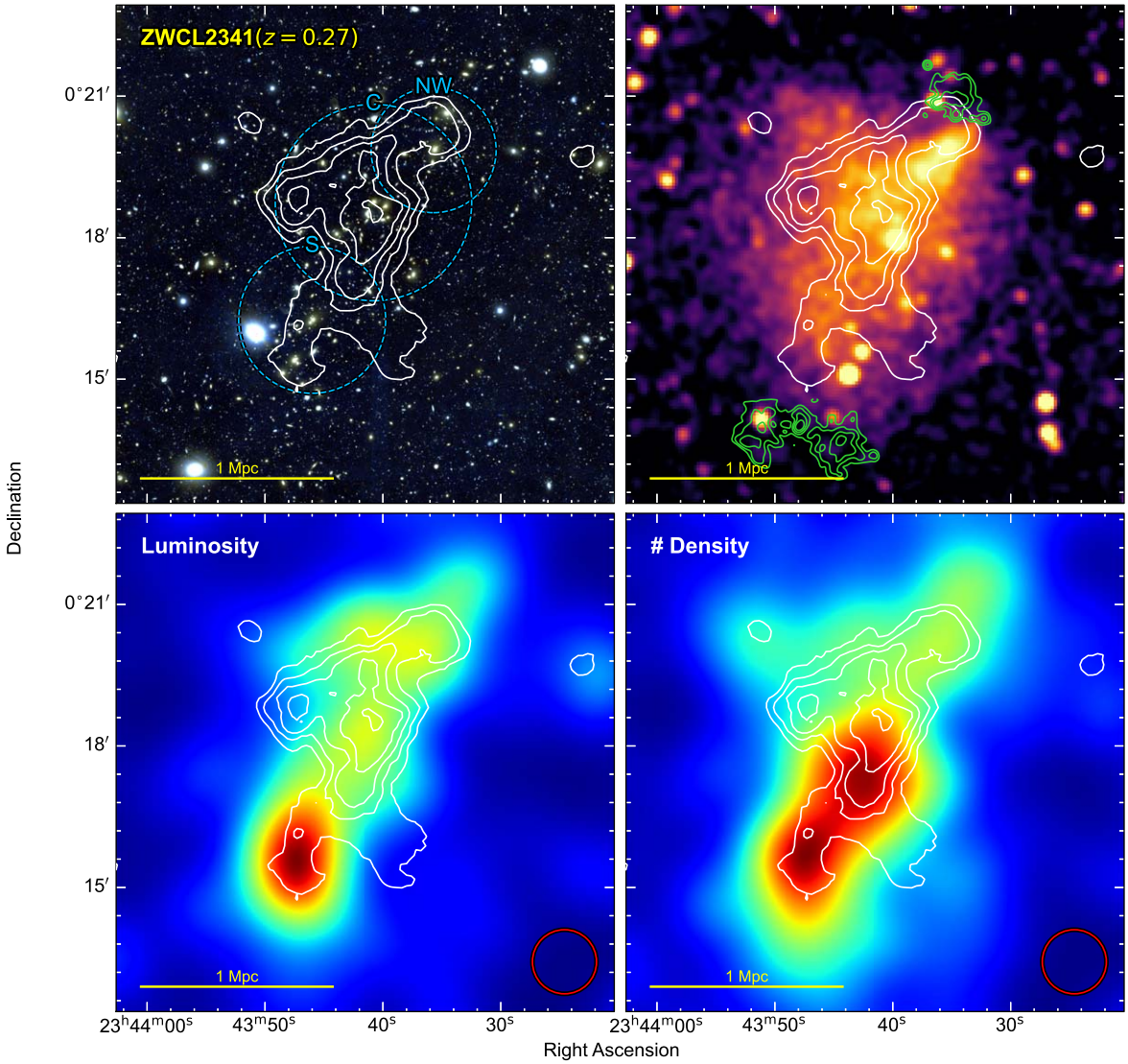

Figure 33. ZwCl2341. A complex cluster merger with a bullet-shaped X-ray emission. WL contours increase in steps of 0.5σ.

radio relics are roughly aligned with each other and separated by about 2 Mpc. In the northwest, a bullet is apparent in X-ray emission. In front of the bullet shape is the northern radio relic with an X-ray shock detected in G. A. Ogrean et al. (2014a). The X-ray emission extends to the northeast and south. A similar X-ray distribution is seen in A3411. The southern ICM contains an X-ray shock and the southern radio relic. X. Zhang et al. (2021) go into detail about many of the merging features that are found in the Chandra observation. Cluster galaxies were identified in W. Boschin et al. (2013) and used to show the southeast–northwest elongation of the cluster. B. Benson et al. (2017) performed a multiwavelength analysis of ZwCl2341. Their modeling of the cluster galaxies determined that the cluster is composed of three subclusters. G19 also detected three subclusters with two in the northwest and one in the southeast.

B. Benson et al. (2017) also provided a WL analysis of the galaxy cluster. Their WL analysis on the available Subaru *r*-band imaging shows a single peak with a broad distribution that covers the brightest galaxies in the cluster. They fit a single NFW model and found the mass to be $4.9 \pm 2.1 \times 10^{14}\,M_{\odot}$.

WL result. Our WL analysis (Figure 33) shows a peak in the center that traces an overdensity of cluster member galaxies. From the central peak, there are extensions to the south, east, and north. The southern extension overlaps the brightest and densest galaxy region, but is only detected at the 2.8σ level in WL. The northern extension contains the bullet X-ray emission and more bright cluster galaxies. The eastern extension is the most peculiar. It seems to not trace many cluster galaxies. The peak of the eastern extension lies on top of a deep yellow elliptical galaxy. It may be possible that there is a background cluster in the east of the X-ray emission that is contaminating the WL signal. The histogram of spectroscopic redshifts in Figure 4 of B. Benson et al. (2017) shows a possible background structure at $z = 0.31$, but more spectroscopy would be needed to confirm it. We fit a three-halo model to the northwestern, central, and southern subclusters and find masses of $M_{200,\mathrm{NW}} = 0.8 \pm 0.6 \times 10^{14}\,M_{\odot}$, $M_{200,\mathrm{C}} = 3.1 \pm 1.2 \times 10^{14}\,M_{\odot}$, and $M_{200,\mathrm{S}} = 1.3 \pm 0.7 \times 10^{14}\,M_{\odot}$.

Merger insight. ZwCl2341 is another example of a very complex cluster merger. The formation of the radio relics likely resulted from a collision between the central and southern subclusters, the central and northern clusters, or both collisions.

The complexity of ZwCl2341 makes it a difficult cluster to simulate. A better approach may be to search for analogs from cosmological simulations.

4.27. Nondetections

For three of the clusters that are analyzed in G19, we are unable to provide WL results. Our WL analyses of A3365 ($z = 0.093$) and RXC J1053.7+5452 ($z = 0.072$) result in no detection. Further analysis of the imaging will be required to understand the failure. For RXCJ1053, bright stars in the Subaru imaging are the probable cause of no detection. Bright stars can be removed by careful subtraction of a 2D model from the stacked image. For example, observations with the HSC targeting A746 were planned to fix a bright star at the center of the focal plane, which allowed for an easier subtraction of a symmetric model (K. HyeongHan et al. 2024a). Future imaging of RXCJ1053 could use this technique to alleviate the issue of the bright star. At the time of this analysis, A2443 ($z = 0.110$) had no WL-quality imaging. However, the cluster was recently observed with the HSC (PI: H. Cho), and the observations are starting to be analyzed. The WL result will be presented in H. Cho et al. (2025, in preparation).

5. Discussion

5.1. WL Mass Estimate Comparison

The c–M relation is typically derived from simulations that have a fixed volume and, in some cases, a fixed cosmology (e.g., A. R. Duffy et al. 2008; A. A. Dutton & A. V. Macciò 2014); although, some are valid for any cosmology (e.g., B. Diemer & M. Joyce 2019; T. Ishiyama et al. 2021). Under these constraints, the c and M of clusters in the simulation are limited and may not represent the full range of observed clusters. This may be particularly true for the merging cluster sample where recent, powerful gravitational interactions have taken place that could have a significant impact on the concentration of the dark matter distribution. To test whether the c–M relation holds for merging clusters, it would be ideal to compare a measured concentration from the merging cluster sample to the expected concentration of the c–M relation. However, concentrations are poorly constrained for most individual clusters (see K. Umetsu et al. 2020, for stacked WL constraints on concentration). An alternative is to test the effect of a merger on the concentration by comparing the mass derived from a c–M relation to that of an independent method such as our two-parameter fitting method (2PNFW).

Figure 34 compares the subcluster mass estimates from the A. R. Duffy et al. (2008) c–M relation to the 2PNFW method. We perform a linear regression to the mass estimates using the `kmpfit` Python package. The fuchsia line is the result of the linear regression with the filled blue region representing the 95% confidence interval. The slope of the best-fit line appears to be steeper than the 1:1 ratio (black dashed line) with more massive subclusters having a higher mass from the 2PNFW method than the A. R. Duffy et al. (2008) c–M relation. We perform a Wald test with a null hypothesis that the best-fit line does not follow the 1:1 relation. The Wald test returns a p-value of 0.11, and thus, we cannot rule out that they follow the same relation.

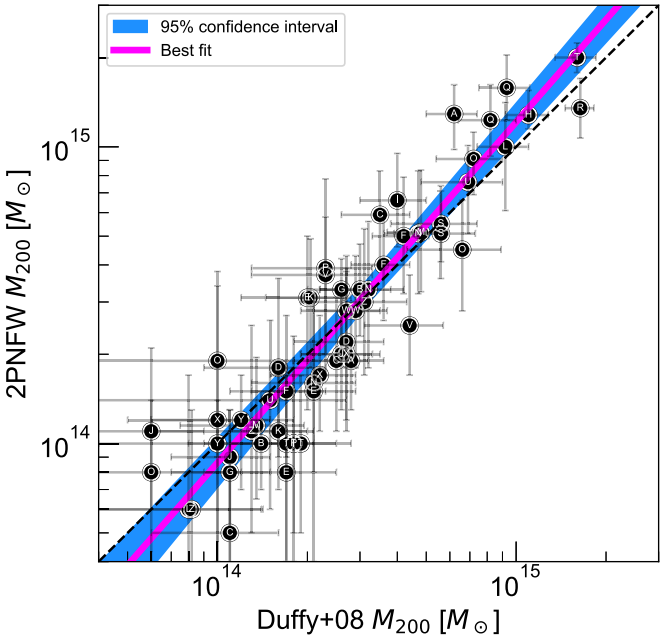

Figure 34. Comparison of the mass derived from the A. R. Duffy et al. (2008) c–M relation to the mass derived from the two-parameter fit (values from Table 4). The black dashed line represents the 1:1 relation. The fuchsia line is the best-fit linear regression. Uncertainties are considered on both axes.

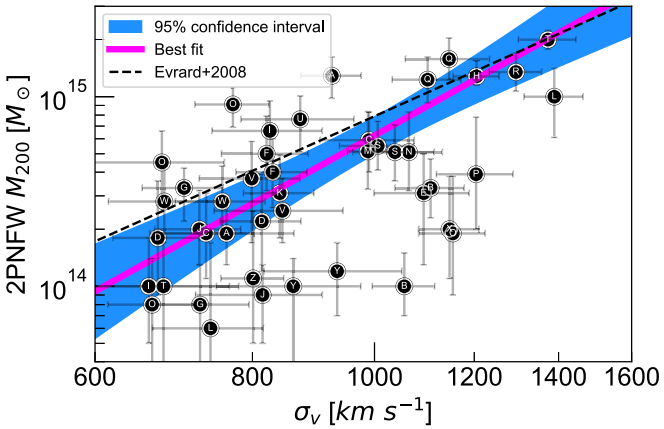

Figure 35. WL mass–σ_v scaling relation for subclusters of merging systems that exhibit radio relics. Masses and system index letters are from Table 4. The black dashed line is the A. E. Evrard et al. (2008) scaling relation. WL mass estimates are preferentially lower than the A. E. Evrard et al. (2008) relation, especially at the low-mass end. ZWCL2341–NW and A2034–SW have very low velocity dispersions (359 ± 39 and 366 ± 55 km s^{-1}, respectively) and are not shown here but are included in the analysis.

5.2. WL Mass–Velocity Dispersion Scaling Relation

Merging galaxy clusters are the most energetic events since the Big Bang (C. L. Sarazin 2002). This energy is dissipated into the cluster and heats up the ICM. In addition, the increase in gravitational potential caused by the introduction of another cluster will in turn boost the velocity dispersion of galaxies and dark matter for a limited time (e.g., J. Pinkney et al. 1996; M. Takizawa et al. 2010). Therefore, in merging clusters that are observed shortly after collision, it is expected that the mass derived from the velocity dispersion of galaxies would be biased high.

In Figure 35, we plot our WL-derived masses from the 2PNFW method against the velocity dispersion of galaxies that

are reported in G19. The black dashed line is the A. E. Evrard et al. (2008) scaling relation. The best-fit line sits below the scaling relation, which is in agreement with the expectation that velocity dispersion is boosted by the recent merger. It is also interesting that the best-fit line is steeper than the A. E. Evrard et al. (2008) scaling relation. Again, we perform a Wald test, with the hypothesis that our measurements do not follow the A. E. Evrard et al. (2008) scaling relation, and we find a p-value of 0.003. Thus, we find that our relation is statistically different than the A. E. Evrard et al. (2008) relation. However, including the intrinsic scatter in the A. E. Evrard et al. (2008) relation (∼10%) loosens the p-value to 0.09 and prevents a conclusion on the hypothesis. The scaling relation based on the best-fit line is

$$M_{200} = \left(\frac{\sigma_v}{1156 \pm 381 \text{ km s}^{-1}}\right)^{3.8\pm0.4} 10^{15}\, M_\odot. \quad (19)$$

One cause of a steeper relation may be the merging nature of the systems. It is possible that the low-mass subclusters that we are analyzing are more affected by the merging event than the high-mass counterparts, since the former have recently undergone a gravitational interaction with a subcluster of similar or greater mass. For example, if a high-mass and a low-mass subcluster both gain the same amount of kinetic energy, the low-mass subcluster will have a larger relative boost to its velocity dispersion. An alternative explanation for the steeper slope could be systematics. Measuring the velocity dispersion relies on the assignment of galaxies into groups. In the crowded environment of a merging galaxy cluster, it is difficult to perform this assignment. G19 used a GMM technique to perform the assignment. Naturally, it is more likely that a galaxy in the cluster system belongs to a high-mass halo than a low-mass halo. During the assignment of galaxies to halos, there is a greater chance that a galaxy that belonged to the more massive halo would be falsely assigned to the low-mass halo. The false assignment would, on average, increase the low-mass halo's velocity dispersion measurements. Conversely, the improper assignment of a galaxy from a low-mass halo to a high-mass halo would have a smaller impact on the velocity dispersion measurement.

5.3. Mass Ratio

The energy required to create Mpc-scale merger shocks is expected to be high and is dependent on cluster mass (e.g., F. de Gasperin et al. 2014). To better understand the types of mergers that are occurring that lead to the creation of radio relics, we plot the mass ratio of the merging subclusters.

Figure 36 compares the WL mass of the primary and secondary subclusters. These were selected from the substructures of each merging cluster by their alignment with the X-ray- and radio-defined merger axes, their agreement with BCG locations, and their WL S/N. In total, we were able to identify primary and secondary subclusters in 22 of the systems (omitting A746, A781, A1300, and MACSJ1149). Figure 36 shows that many of the mergers are close to 1:1 mass ratio, independent of the mass scale. Furthermore, most of the clusters (∼70%) are in major mergers with mass ratio <4:1. The few outliers tend to be clusters with very massive primaries, such as PLCKG287 and A2163. Perhaps this is an indication that very massive major mergers are rare. However, there may be a selection effect because low-mass primaries ($\lesssim 10^{14} M_\odot$) would require very low-mass secondaries ($<10^{14} M_\odot$), which are below the detection threshold of this Subaru WL data set.

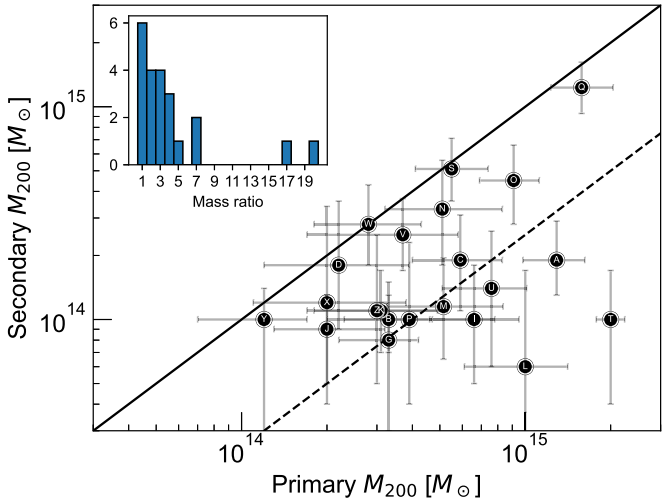

Figure 36. Mass ratio of merging clusters that exhibit radio relics. Masses are from the 2PNFW method. Masses and system index letters are from Table 4. The solid (dashed) black line represents the 1:1 (1:4) mass ratio. Most of the radio relic systems are in major mergers (ratio < 4). Twenty-two of the systems are shown here (omitting A746, A781, A1300, and MACSJ1149).

5.4. Peak Separation

Given the large number of subclusters analyzed in this work, we can compare the separation of various tracers of the dark matter potential, which may provide insight into the physics of the collision (e.g., S. Y. Kim et al. 2017). In Section 3.7, we identified WL peaks by correlating them with nearby galaxies and/or X-ray brightness peaks. Therefore, this comparison is done knowing that the luminous tracer was initially used in identification of the WL peaks. In addition, we make the assumption that the WL peak is also the mass peak. Systematic effects, such as miscentering, may alter the accuracy of using the WL peak as the mass peak.

Figure 37 shows the projected separation of the WL peak from the nearest BCG, luminosity peak, and number density peak for each subcluster. For each system, the uncertainty on the location of the mass peak for each subcluster was estimated by collecting the mass peak location in the 1000 bootstrapped mass maps. The peaks were then processed with a k-means clustering algorithm with the number of clusters fixed to the expected value (i.e., two for a merging cluster that has two subclusters). The distribution of each of the k-means-defined subclusters was then used to derive the error ellipse that contained 68% of the peaks. For the uncertainty of the galaxy luminosity and number density peaks, we use the standard deviation of the smoothing kernel that was applied to the maps in Section 4.

For the majority of subclusters, the uncertainty on the mass peak has a 1σ overlap with the positions of the luminous tracer. We find that the BCG is closer than the luminosity (number density) peak to the mass peak in 72% (68%) of the subclusters. The median values (vertical lines in Figure 37) show that the BCG is the best tracer of the mass peak. The median projected separation of the BCG, the luminosity peak, and the number density peak from their respective WL peak is 79 ± 14, 90 ± 15, and 119 ± 15 kpc, respectively. Our median projected separation of the BCG from the mass peak agrees

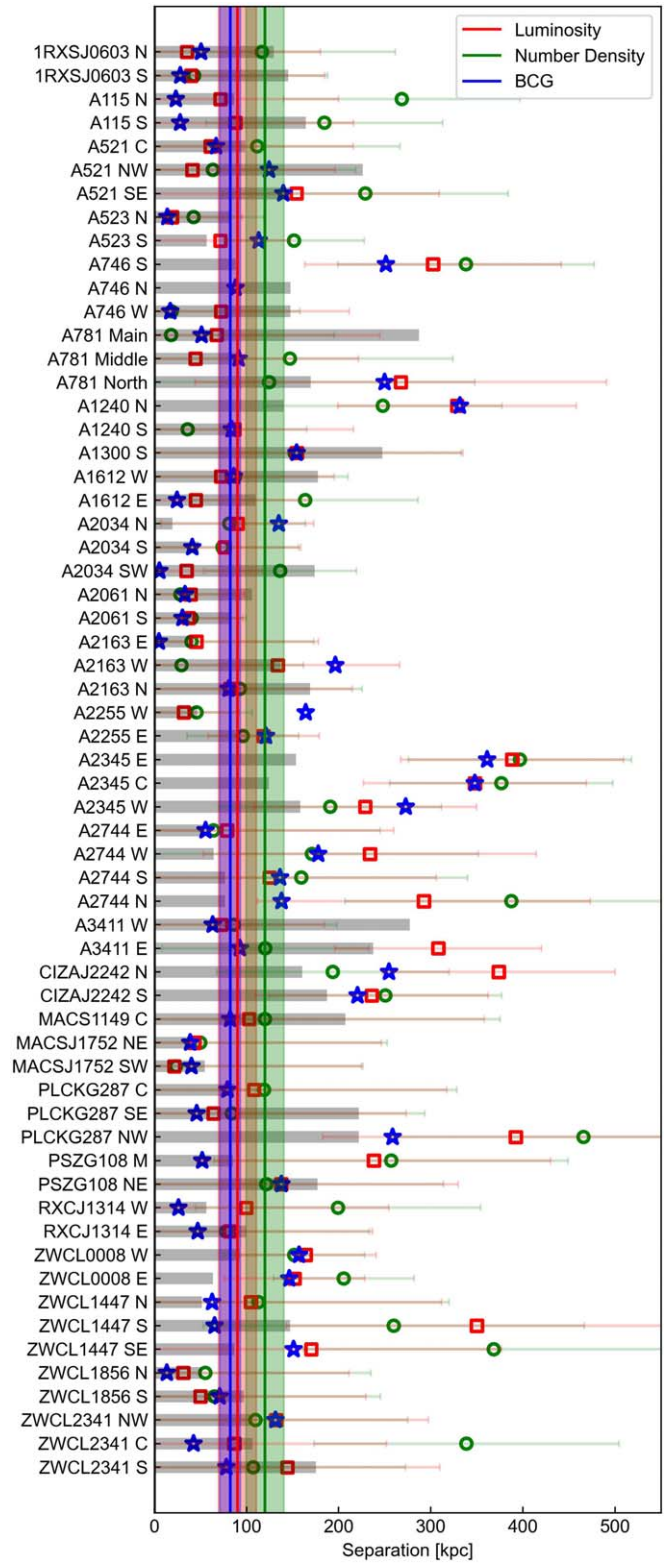

Figure 37. Projected separation of the BCGs (blue stars), luminosity peaks (red squares), and number density peaks (green) from the WL peak. The horizontal gray bars represent the uncertainty on the mass peak position. The vertical colored lines show the median separations of each luminous tracer from the mass peak and their 68% uncertainty.

with M. Oguri et al. (2010), who found that the separation follows a Gaussian distribution with $\sigma = 90$ kpc. M. R. George et al. (2012) compared the WL mass peaks to BCGs in X-ray detected galaxy groups and found the average projected separation to be <75 kpc. Using the large sample of 10,000 SDSS clusters, A. Zitrin et al. (2012) studied the offset of the BCG from the DM peak and found that the average offset is ∼13 kpc. For our sample, only one of the 58 subclusters has a BCG within 13 kpc of the mass peak. However, the uncertainties on the mass peak are on average ∼100 kpc. Therefore, these results are not statistically conclusive.

An additional tracer of the DM potential that is beyond the scope of this work is the intracluster light (ICL). J. Yoo et al. (2022, 2024) showed in simulations that the ICL is a good tracer of the DM potential. We will explore the possibility of using the ICL as a tracer of the DM potential in future work.

5.5. The Golden Sample

Dissociation of the ICM from the cluster potential by ram pressure during a cluster merger is a powerful feature that can be used to understand the merger scenario and constrain the physics of mergers (for an example, see C. Zhang et al. 2019). However, the variety of gas dissociation in merging clusters is diverse. Clusters such as A115 have broad V-shaped X-ray emission tails that are as wide as they are long. In contrast, the tails behind the subclusters of MACSJ1752 extend approximately 0.5 Mpc but are only ∼100 kpc at their greatest width. The relation of X-ray brightness peaks and WL peaks also vary. In some dissociative mergers, like A115, the X-ray brightness peaks are retained in the WL peak. Conversely, in A2034, the X-ray brightness peaks trail behind the WL peaks. As demonstrated in simulations by J. A. ZuHone et al. (2018), the differences may be caused by impact parameter, premerger concentration of the ICM, total mass, concentration of the DM, or projection.

Achieving a sound understanding of cluster mergers relies on carefully recreating the collision on a computer. Cases like A2744 and A746 have multiple subclusters that are merging along many axes, which makes them difficult to reproduce. For constraining the properties of merging clusters, it is best to start with the simplest cases. G19 defined a "gold sample" of cluster mergers that have simple geometry. Having completed WL analyses of the systems, we provide an updated gold sample. These systems have distinct merger features and mostly bimodal mass distributions. Our updated gold sample is A1240, A2034, MACSJ1752, RXCJ1314, ZwCl0008, ZwCl1447, and ZwCl1856. CIZAJ2242 is also a strong candidate, but, at this point, the existing optical/IR observations of the cluster cannot support a WL analysis of the precision that is needed to fully understand the complexity of the mass distribution. Aside from A2034, these systems all contain double radio relics, which provide critical constraints on the merger timescale and viewing angle. There are additional candidate systems that may be valuable, such as A1612, but the current multiwavelength data do not support a robust analysis.

6. Conclusions

We present WL analyses of 29 merging galaxy clusters that exhibit Mpc-sized radio relics. The WL analyses are performed on Subaru Suprime-Cam and HSC observations. Of the 29 systems, WL analyses are successfully achieved for 26 clusters, and three clusters are unsuccessful.

Our WL analysis technique uses a PCA to create PSF models for each galaxy and a Gaussian model to fit the galaxy shape. Source galaxies are selected from CMDs utilizing the spectroscopically confirmed red-sequence galaxies as a guide. The source galaxies are used to generated high-resolution mass maps with the FIATMAP code. Comparing the mass maps with the vast multiwavelength supplementary data, significant (WL $S/N \gtrsim 3$) subclusters are identified. Mass estimates for each subcluster of a system are determined by simultaneously fitting multiple NFW halos to the source galaxies. The mass estimates are performed by both fitting a c–M relation (A. R. Duffy et al. 2008) and by MCMC sampling the c and M parameter space. With subclusters identified and masses estimated, an in-depth discussion of each merging system is presented. From the analysis of each system and the analysis of the radio relic sample as a whole, the following conclusions are made:

1. We combine our WL results with the multiwavelength observations from literature to develop a better understanding of each merging system. We show that WL analysis is critical to detecting and quantifying the substructures in merging clusters and in some cases discover subclusters that were previously undetected. Utilizing the new information provided through WL analysis, we update the merging scenarios for each system and give new insight into the past collisions. In addition, we highlight peculiar systems that warrant further investigation, such as the dissociative nature of Abell 2061 and its large radio relic distance.
2. We compare WL mass maps to the X-ray emission from the ICM. In cases such as MACSJ1752 and ZWCL1856, we find that the X-ray emission, WL mass maps, and radio relics paint a clear picture of the past merger. In others, the complexity of the system and the positions of the radio relics are less straightforward. Gas dissociation is clearly visible in many of the clusters. In general, the overall distribution of the mass maps is elongated in the same manner as the X-ray emission.
3. We compare the mass distributions to the galaxy light and galaxy number density distributions. A strong correlation between mass peaks and galaxies are obvious. In most cases, the most massive subcluster is cospatial with the global luminosity and number density peaks of the system. This finding is not surprising if more massive halos are expected to have more galaxies. However, in clusters such as A1240 and A1612, the more-massive subcluster is not associated with the global luminosity and number density peaks. The galaxy distributions in general show the same elongation as the X-ray and WL signals and in some cases stretch further along the axis of elongation.
4. We investigate the influence of method on the mass estimation by comparing the use of a c–M relation to a mass estimate that samples both c and M. Our best-fit line shows a steeper slope than the 1:1 relation, but the statistical power of the data do not rule out that they follow the 1:1 relation.
5. The WL-derived masses are compared to the velocity dispersion measurements, a proxy for mass, of each subcluster. We find that the scatter of the velocity dispersion with respect to the WL mass is large. Lower mass subclusters tend to have more inflated velocity dispersions than higher mass subclusters when compared to the scaling relation from A. E. Evrard et al. (2008). We suggest that this could be caused by the increased gravitational effect that low-mass subclusters feel during pericenter passage, which inflates the velocity dispersion and leads to the large scatter in comparison to WL mass.
6. For each system, primary and secondary subclusters that are responsible for the generation of the radio relics are distinguished by their mass and alignment to the radio relics. Comparing the mass of the primary to secondary subclusters, we find that most merging clusters that exhibit radio relics are major mergers with a mass ratio <4.
7. We analyze the separation of the peak of the dark matter distribution from other luminous peaks. On average, the BCG most closely traces the dark matter peak followed by the luminosity and then the number density peak. The average offset of the BCG from its mass peak is found to be 75 ± 14 kpc.
8. An updated sample of eight ideal merging clusters were defined (a Golden sample). The ideal cases have clear X-ray features, such as bullet morphology that highlight the merger path, and have verified merger-induced radio relics. Additional important selection criteria come from the WL signal: robust detection of the WL signal, dominant bimodal distribution, and dissociation of the gas from the dark matter density peaks. This sample of merging clusters represents the ideal cases that can be reproduced through simulations. Furthermore, the large separation of the mass peaks from the gas peaks makes this sample idea for studying the nature of dark matter.

From this analysis, we have provided an in-depth view of the dark matter in merging systems that exhibit radio relics. The sample of radio relic clusters has been increasing quickly with new detections from telescopes such as LOFAR and MeerKAT. New observations with ground-based optical telescopes would be valuable for studying these new systems, and it would be particularly useful to gather observations for WL on the southern hemisphere systems. Finally, with radio telescopes detecting more distant radio relics, IR imaging with the Nancy Grace Roman Telescope will be extremely valuable for mapping out the dark matter in high-z clusters.

Acknowledgments

We thank the anonymous reviewer for providing an in-depth review of the manuscript and valuable comments. This work was authored by employees of Caltech/IPAC under contract No. 80GSFC21R0032 with the National Aeronautics and Space Administration. M.J.J. acknowledges support for the current research from the National Research Foundation (NRF) of Korea under the programs 2022R1A2C1003130 and RS2023-00219959. W.L. acknowledges support from the National Research Foundation of Korea (NRF) grant funded by the Korea government (MSIT) (RS-2024-00340949). R.J.v.W. acknowledges support from the ERC Starting grant ClusterWeb 804208. D.W. was supported by NSF grant 2308383. M.Y. acknowledges funding from the European Research Council (ERC) under the European Union's Horizon 2020 research and innovation program (grant agreement No. 101053992). This research is based on data collected at the Subaru Telescope, which is operated by the National Astronomical Observatory of

Japan. We are honored and grateful for the opportunity of observing the Universe from Maunakea, which has the cultural, historical, and natural significance in Hawaii. MGCLS data products were provided by the South African Radio Astronomy Observatory and the MGCLS team and were derived from observations with the MeerKAT radio telescope. The MeerKAT telescope is operated by the South African Radio Astronomy Observatory, which is a facility of the National Research Foundation, an agency of the Department of Science and Innovation. Based on observations obtained with XMM-Newton, an ESA science mission with instruments and contributions directly funded by ESA Member States and NASA. This research has made use of data obtained from the Chandra Data Archive and the Chandra Source Catalog, and software provided by the Chandra X-ray Center (CXC) in the application packages CIAO and Sherpa. This paper makes use of LSST Science Pipelines software developed by the Vera C. Rubin Observatory. We thank the Rubin Observatory for making their code available as free software at https://pipelines.lsst.io.

Software: Astropy (Astropy Collaboration et al. 2022), Matplotlib (J. D. Hunter 2007), Scikit-learn (F. Pedregosa et al. 2011), IRAF (D. Tody 1986), SDFRED1 (M. Yagi et al. 2002), SDFRED2 (M. Ouchi et al. 2004), SExtractor (E. Bertin & S. Arnouts 1996), SCAMP (E. Bertin 2006), SWarp (E. Bertin et al. 2002), CIAO (A. Fruscione et al. 2006).

ORCID iDs

Kyle Finner https://orcid.org/0000-0002-4462-0709
M. James Jee https://orcid.org/0000-0002-5751-3697
Hyejeon Cho https://orcid.org/0000-0001-5966-5072
Kim HyeongHan https://orcid.org/0000-0002-2550-5545
Wonki Lee https://orcid.org/0000-0002-1566-5094
Reinout J. van Weeren https://orcid.org/0000-0002-0587-1660
David Wittman https://orcid.org/0000-0002-0813-5888
Mijin Yoon https://orcid.org/0000-0002-3683-9559

References

Abate, A., Wittman, D., Margoniner, V. E., et al. 2009, ApJ, 702, 603
Abriola, D., Della Pergola, D., Lombardi, M., et al. 2024, A&A, 684, A193
Akamatsu, H., Mizuno, M., Ota, N., et al. 2017, A&A, 600, A100
Akamatsu, H., van Weeren, R. J., Ogrean, G. A., et al. 2015, A&A, 582, A87
Andrade-Santos, F., van Weeren, R. J., Di Gennaro, G., et al. 2019, ApJ, 887, 31
Arnaud, M., Hughes, J. P., Forman, W., et al. 1992, ApJ, 390, 345
Arnaud, M., Maurogordato, S., Slezak, E., & Rho, J. 2000, A&A, 355, 461
Astropy Collaboration, Price-Whelan, A. M., Lim, P. L., et al. 2022, ApJ, 935, 167
Bagchi, J., Sirothia, S. K., Werner, N., et al. 2011, ApJL, 736, L8
Barrena, R., Boschin, W., Girardi, M., & Spolaor, M. 2007, A&A, 469, 861
Barrena, R., Girardi, M., Boschin, W., & Dasì, M. 2009, A&A, 503, 357
Bartelmann, M., & Schneider, P. 2001, PhR, 340, 291
Becker, M. R., & Kravtsov, A. V. 2011, ApJ, 740, 25
Beers, T. C., Huchra, J. P., & Geller, M. J. 1983, ApJ, 264, 356
Benson, B., Wittman, D. M., Golovich, N., et al. 2017, ApJ, 841, 7
Bertin, E. 2006, in ASP Conf. Ser. 351, Astronomical Data Analysis Software and Systems XV, ed. C. Gabriel et al. (San Francisco, CA: ASP), 112
Bertin, E., & Arnouts, S. 1996, A&AS, 117, 393
Bertin, E., Mellier, Y., & Radovich, M. 2002, in ASP Conf. Ser. 281, Astronomical Data Analysis Software and Systems XI, ed. D. A. Bohlender, D. Durand, & T. H. Handley (San Francisco, CA: ASP), 228
Biffi, V., Borgani, S., Murante, G., et al. 2016, ApJ, 827, 112
Bonafede, A., Brüggen, M., van Weeren, R., et al. 2012, MNRAS, 426, 40
Bonafede, A., Giovannini, G., Feretti, L., Govoni, F., & Murgia, M. 2009, A&A, 494, 429
Bonafede, A., Intema, H. T., Brüggen, M., et al. 2014, ApJ, 785, 1
Bond, J. R., Kofman, L., & Pogosyan, D. 1996, Natur, 380, 603
Bosch, J., AlSayyad, Y., Armstrong, R., et al. 2019, in ASP Conf. Ser. 523, Astronomical Data Analysis Software and Systems XXVII, ed. P. J. Teuben et al. (San Francisco, CA: ASP), 521
Bosch, J., Armstrong, R., Bickerton, S., et al. 2018, PASJ, 70, S5
Boschin, W., Girardi, M., & Barrena, R. 2013, MNRAS, 434, 772
Botteon, A., Brunetti, G., Ryu, D., & Roh, S. 2020a, A&A, 634, A64
Botteon, A., Brunetti, G., van Weeren, R. J., et al. 2020b, ApJ, 897, 93
Botteon, A., Gastaldello, F., Brunetti, G., & Dallacasa, D. 2016, MNRAS, 460, L84
Botteon, A., Shimwell, T. W., Bonafede, A., et al. 2019, A&A, 622, A19
Botteon, A., Shimwell, T. W., Cassano, R., et al. 2022a, A&A, 660, A78
Botteon, A., van Weeren, R. J., Brunetti, G., et al. 2022b, SciA, 8, eabq7623
Bourdin, H., Mazzotta, P., Markevitch, M., Giacintucci, S., & Brunetti, G. 2013, ApJ, 764, 82
Broadhurst, T., Takada, M., Umetsu, K., et al. 2005, ApJL, 619, L143
Brüggen, M., van Weeren, R. J., & Röttgering, H. J. A. 2012, MNRAS, 425, L76
Brunetti, G., & Lazarian, A. 2007, MNRAS, 378, 245
Bruno, L., Rajpurohit, K., Brunetti, G., et al. 2021, A&A, 650, A44
Butcher, H. R., & Oemler, A. J. 1984, Natur, 310, 31
Cha, S., HyeongHan, K., Scofield, Z. P., Joo, H., & Jee, M. J. 2024, ApJ, 961, 186
Chambers, K. C., Magnier, E. A., Metcalfe, N., et al. 2016, arXiv:1612.05560
Cho, H., James Jee, M., Smith, R., Finner, K., & Lee, W. 2022, ApJ, 925, 68
Clowe, D., Bradač, M., Gonzalez, A. H., et al. 2006, ApJL, 648, L109
Cohen, A. S., & Clarke, T. E. 2011, AJ, 141, 149
Cook, R. I., & Dell'Antonio, I. P. 2012, ApJ, 750, 153
Cova, F., Gastaldello, F., Wik, D. R., et al. 2019, A&A, 628, A83
Dahle, H., Kaiser, N., Irgens, R. J., Lilje, P. B., & Maddox, S. J. 2002, ApJS, 139, 313
Dahlen, T., Mobasher, B., Dickinson, M., et al. 2010, ApJ, 724, 425
Dallacasa, D., Brunetti, G., Giacintucci, S., et al. 2009, ApJ, 699, 1288
Dawson, W. A. 2013, ApJ, 772, 131
Dawson, W. A., Jee, M. J., Stroe, A., et al. 2015, ApJ, 805, 143
de Gasperin, F., Brunetti, G., Brüggen, M., et al. 2020, A&A, 642, A85
de Gasperin, F., Intema, H. T., van Weeren, R. J., et al. 2015, MNRAS, 453, 3483
de Gasperin, F., van Weeren, R. J., Brüggen, M., et al. 2014, MNRAS, 444, 3130
Di Gennaro, G., van Weeren, R. J., Andrade-Santos, F., et al. 2019, ApJ, 873, 64
Di Gennaro, G., van Weeren, R. J., Hoeft, M., et al. 2018, ApJ, 865, 24
Diemer, B., & Joyce, M. 2019, ApJ, 871, 168
Donnert, J. M. F., Beck, A. M., Dolag, K., & Röttgering, H. J. A. 2017, MNRAS, 471, 4587
Donnert, J. M. F., Stroe, A., Brunetti, G., Hoang, D., & Roettgering, H. 2016, MNRAS, 462, 2014
Dressler, A. 1984, ApJ, 281, 512
Drury, L. O. 1983, RPPh, 46, 973
Duffy, A. R., Schaye, J., Kay, S. T., & Dalla Vecchia, C. 2008, MNRAS, 390, L64
Dutton, A. A., & Macciò, A. V. 2014, MNRAS, 441, 3359
Eckert, D., Jauzac, M., Shan, H., et al. 2015, Natur, 528, 105
Eckert, D., Vazza, F., Ettori, S., et al. 2012, A&A, 541, A57
Evrard, A. E., Bialek, J., Busha, M., et al. 2008, ApJ, 672, 122
Fabricant, D., Fata, R., Roll, J., et al. 2005, PASP, 117, 1411
Feretti, L., Fusco-Femiano, R., Giovannini, G., & Govoni, F. 2001, A&A, 373, 106
Feretti, L., Gioia, I. M., Giovannini, G., Gregorini, L., & Padrielli, L. 1984, A&A, 139, 50
Feretti, L., Giovannini, G., Govoni, F., & Murgia, M. 2012, A&ARv, 20, 54
Feretti, L., Orrù, E., Brunetti, G., et al. 2004, A&A, 423, 111
Ferrari, C., Arnaud, M., Ettori, S., Maurogordato, S., & Rho, J. 2006, A&A, 446, 417
Ferrari, C., Maurogordato, S., Cappi, A., & Benoist, C. 2003, A&A, 399, 813
Finner, K., Faisst, A., Chary, R.-R., & Jee, M. J. 2023a, ApJ, 953, 102
Finner, K., HyeongHan, K., Jee, M. J., et al. 2021, ApJ, 918, 72
Finner, K., James Jee, M., Webb, T., et al. 2020, ApJ, 893, 10
Finner, K., Jee, M. J., Golovich, N., et al. 2017, ApJ, 851, 46
Finner, K., Lee, B., Chary, R.-R., et al. 2023b, ApJ, 958, 33
Finner, K., Randall, S. W., Jee, M. J., et al. 2023c, ApJ, 942, 23
Finney, E. Q., Bradač, M., Huang, K.-H., et al. 2018, ApJ, 859, 58
Fruscione, A., McDowell, J. C., Allen, G. E., et al. 2006, Proc SPIE, 6270, 62701V
Fujita, Y., Akamatsu, H., & Kimura, S. S. 2016, PASJ, 68, 34
Fujita, Y., Takizawa, M., Yamazaki, R., Akamatsu, H., & Ohno, H. 2015, ApJ, 815, 116
Furusawa, H., Koike, M., Takata, T., et al. 2018, PASJ, 70, S3

Gabici, S., & Blasi, P. 2003, ApJ, 583, 695
Ge, C., Sun, M., Rozo, E., et al. 2019, MNRAS, 484, 1946
George, M. R., Leauthaud, A., Bundy, K., et al. 2012, ApJ, 757, 2
Giacintucci, S. 2011, MmSAI, 82, 541
Giacintucci, S., Venturi, T., Bardelli, S., et al. 2006, NewA, 11, 437
Giovannini, G., Bonafede, A., Feretti, L., Govoni, F., & Murgia, M. 2010, A&A, 511, L5
Giovannini, G., Bonafede, A., Feretti, L., et al. 2009, A&A, 507, 1257
Giovannini, G., Cau, M., Bonafede, A., et al. 2020, A&A, 640, A108
Giovannini, G., Tordi, M., & Feretti, L. 1999, NewA, 4, 141
Giovannini, G., Vacca, V., Girardi, M., et al. 2013, MNRAS, 435, 518
Girardi, M., Boschin, W., Gastaldello, F., et al. 2016, MNRAS, 456, 2829
Golovich, N., Dawson, W. A., Wittman, D. M., et al. 2019a, ApJ, 882, 69
Golovich, N., Dawson, W. A., Wittman, D. M., et al. 2019b, ApJS, 240, 39
Golovich, N., van Weeren, R. J., Dawson, W. A., Jee, M. J., & Wittman, D. 2017, ApJ, 838, 110
Govoni, F., Murgia, M., Giovannini, G., Vacca, V., & Bonafede, A. 2011, A&A, 529, A69
Gruen, D., Seitz, S., Brimioulle, F., et al. 2014, MNRAS, 442, 1507
Ha, J.-H., Ryu, D., & Kang, H. 2018, ApJ, 857, 26
Hallman, E. J., Alden, B., Rapetti, D., Datta, A., & Burns, J. O. 2018, ApJ, 859, 44
Harvey, D. R., & Massey, R. 2024, MNRAS, 529, 802
Hoang, D. N., Shimwell, T. W., Stroe, A., et al. 2017, MNRAS, 471, 1107
Hoang, D. N., Shimwell, T. W., van Weeren, R. J., et al. 2018, MNRAS, 478, 2218
Hoekstra, H. 2013, arXiv:1312.5981
Hoekstra, H., Franx, M., & Kuijken, K. 2000, ApJ, 532, 88
Hoekstra, H., Mahdavi, A., Babul, A., & Bildfell, C. 2012, MNRAS, 427, 1298
Hugo, B., Bernardi, G., Smirnov, O. M., et al. 2023, MNRAS, 526, 5278
Hunter, J. D. 2007, CSE, 9, 90
HyeongHan, K., Cho, H., Jee, M. J., et al. 2024a, ApJ, 962, 100
HyeongHan, K., Jee, M. J., Cha, S., & Cho, H. 2024b, NatAs, 8, 377
HyeongHan, K., Jee, M. J., Rudnick, L., et al. 2020, ApJ, 900, 127
Ishiyama, T., Prada, F., Klypin, A. A., et al. 2021, MNRAS, 506, 4210
Itahana, M., Takizawa, M., Akamatsu, H., et al. 2015, PASJ, 67, 113
Jauzac, M., Eckert, D., Schwinn, J., et al. 2016a, MNRAS, 463, 3876
Jee, M. J., Blakeslee, J. P., Sirianni, M., et al. 2007, PASP, 119, 1403
Jee, M. J., Dawson, K. S., Hoekstra, H., et al. 2011, ApJ, 737, 59
Jee, M. J., Dawson, W. A., Stroe, A., et al. 2016, ApJ, 817, 179
Jee, M. J., Hughes, J. P., Menanteau, F., et al. 2014, ApJ, 785, 20
Jee, M. J., Ko, J., Perlmutter, S., et al. 2017, ApJ, 847, 117
Jee, M. J., Mahdavi, A., Hoekstra, H., et al. 2012, ApJ, 747, 96
Jee, M. J., Stroe, A., Dawson, W., et al. 2015, ApJ, 802, 46
Jee, M. J., Tyson, J. A., Schneider, M. D., et al. 2013, ApJ, 765, 74
Jenness, T., Bosch, J. F., Salnikov, A., et al. 2022, Proc. SPIE, 12189, 1218911
Johnston, D. E., Sheldon, E. S., Wechsler, R. H., et al. 2007, arXiv:0709.1159
Jones, A., de Gasperin, F., Cuciti, V., et al. 2021, MNRAS, 505, 4762
Kaiser, N., & Squires, G. 1993, ApJ, 404, 441
Kang, H. 2016a, JKAS, 49, 83
Kang, H. 2016b, JKAS, 49, 145
Kang, H., & Ryu, D. 2015, ApJ, 809, 186
Kang, H., Ryu, D., & Jones, T. W. 2012, ApJ, 756, 97
Kang, H., Ryu, D., & Jones, T. W. 2017, ApJ, 840, 42
Kawanomoto, S., Uraguchi, F., Komiyama, Y., et al. 2018, PASJ, 70, 66
Kempner, J. C., & Sarazin, C. L. 2001, ApJ, 548, 639
Kempner, J. C., Sarazin, C. L., & Markevitch, M. 2003, ApJ, 593, 291
Kim, M., Jee, M. J., Finner, K., et al. 2019, ApJ, 874, 143
Kim, S. Y., Peter, A. H. G., & Wittman, D. 2017, MNRAS, 469, 1414
Knowles, K., Cotton, W. D., Rudnick, L., et al. 2022, A&A, 657, A56
Komiyama, Y., Obuchi, Y., Nakaya, H., et al. 2018, PASJ, 70, S2
Kurtz, M. J., & Mink, D. J. 1998, PASP, 110, 934
Lee, B., Chary, R.-R., & Wright, E. L. 2018, ApJ, 866, 157
Lee, B. E., Le Brun, A. M. C., Haq, M. E., et al. 2018, MNRAS, 479, 890
Lee, W., Cha, S., Jee, M. J., et al. 2023, ApJ, 945, 71
Lee, W., James Jee, M., Finner, K., et al. 2022, ApJ, 924, 18
Lee, W., Jee, M. J., Kang, H., et al. 2020, ApJ, 894, 60
Lee, W., Pillepich, A., ZuHone, J., et al. 2024, A&A, 686, A55
Lemonon, L., Pierre, M., Hunstead, R., et al. 1997, A&A, 326, 34
Loi, F., Murgia, M., Govoni, F., et al. 2017, MNRAS, 472, 3605
Mahdavi, A., Hoekstra, H., Babul, A., Balam, D. D., & Capak, P. L. 2007, ApJ, 668, 806
Mandelbaum, R. 2018, ARA&A, 56, 393
Mandelbaum, R., Rowe, B., Armstrong, R., et al. 2015, MNRAS, 450, 2963
Markevitch, M., Gonzalez, A. H., Clowe, D., et al. 2004, ApJ, 606, 819
Markevitch, M., & Vikhlinin, A. 2007, PhR, 443, 1
Matsukiyo, S., Ohira, Y., Yamazaki, R., & Umeda, T. 2011, ApJ, 742, 47
Maurogordato, S., Cappi, A., Ferrari, C., et al. 2008, A&A, 481, 593
Maurogordato, S., Proust, D., Beers, T. C., et al. 2000, A&A, 355, 848
Mazzotta, P., Bourdin, H., Giacintucci, S., Markevitch, M., & Venturi, T. 2011, MmSAI, 82, 495
Medezinski, E., Broadhurst, T., Umetsu, K., et al. 2010, MNRAS, 405, 257
Medezinski, E., Umetsu, K., Okabe, N., et al. 2016, ApJ, 817, 24
Meneghetti, M. 2022, Introduction to Gravitational Lensing: With Python Examples (Cham: Springer)
Merten, J., Coe, D., Dupke, R., et al. 2011, MNRAS, 417, 333
Miyazaki, S., Komiyama, Y., Kawanomoto, S., et al. 2018, PASJ, 70, S1
Miyazaki, S., Komiyama, Y., Sekiguchi, M., et al. 2002, PASJ, 54, 833
Miyazaki, S., Oguri, M., Hamana, T., et al. 2015, ApJ, 807, 22
Molnar, S. M., & Broadhurst, T. 2017, ApJ, 841, 46
Molnar, S. M., & Broadhurst, T. 2018, ApJ, 862, 112
Monteiro-Oliveira, R., Cypriano, E. S., Vitorelli, A. Z., et al. 2018, MNRAS, 481, 1097
Moura, M. T., Machado, R. E. G., & Monteiro-Oliveira, R. 2021, MNRAS, 500, 1858
Murata, R., Oguri, M., Nishimichi, T., et al. 2019, PASJ, 71, 107
Navarro, J. F., Frenk, C. S., & White, S. D. M. 1997, ApJ, 490, 493
Ogrean, G. A., Brüggen, M., Röttgering, H., et al. 2013a, MNRAS, 429, 2617
Ogrean, G. A., Brüggen, M., van Weeren, R. J., Burgmeier, A., & Simionescu, A. 2014a, MNRAS, 443, 2463
Ogrean, G. A., Brüggen, M., van Weeren, R., et al. 2014b, MNRAS, 440, 3416
Ogrean, G. A., Brüggen, M., van Weeren, R. J., et al. 2013b, MNRAS, 433, 812
Ogrean, G. A., van Weeren, R. J., Jones, C., et al. 2016, ApJ, 819, 113
Oguri, M., & Hamana, T. 2011, MNRAS, 414, 1851
Oguri, M., Takada, M., Okabe, N., & Smith, G. P. 2010, MNRAS, 405, 2215
Okabe, N., Akamatsu, H., Kakuwa, J., et al. 2015, PASJ, 67, 114
Okabe, N., Bourdin, H., Mazzotta, P., & Maurogordato, S. 2011, ApJ, 741, 116
Okabe, N., & Smith, G. P. 2016, MNRAS, 461, 3794
Okabe, N., Takada, M., Umetsu, K., Futamase, T., & Smith, G. P. 2010, PASJ, 62, 811
Okabe, N., & Umetsu, K. 2008, PASJ, 60, 345
Ouchi, M., Shimasaku, K., Okamura, S., et al. 2004, ApJ, 611, 660
Owers, M. S., Nulsen, P. E. J., Couch, W. J., et al. 2014, ApJ, 780, 163
Parekh, V., Kincaid, R., Thorat, K., et al. 2022, MNRAS, 509, 3086
Pearce, C. J. J., van Weeren, R. J., Andrade-Santos, F., et al. 2017, ApJ, 845, 81
Pearson, D. W., Batiste, M., & Batuski, D. J. 2014, MNRAS, 441, 1601
Pedregosa, F., Varoquaux, G., Gramfort, A., et al. 2011, JMLR, 12, 2825
Peebles, P. J. E. 1980, The Large-scale Structure of the Universe (Princeton, NJ: Princeton Univ. Press)
Pierre, M., Oukbir, J., Dubreuil, D., et al. 1997, A&AS, 124, 283
Pinkney, J., Roettiger, K., Burns, J. O., & Bird, C. M. 1996, ApJS, 104, 1
Pizzo, R. F., & de Bruyn, A. G. 2009, A&A, 507, 639
Planck Collaboration, Ade, P. A. R., Aghanim, N., et al. 2016, A&A, 594, A27
Postman, M., Geller, M. J., & Huchra, J. P. 1988, AJ, 95, 267
Radovich, M., Puddu, E., Romano, A., Grado, A., & Getman, F. 2008, A&A, 487, 55
Rajpurohit, K., Hoeft, M., van Weeren, R. J., et al. 2018, ApJ, 852, 65
Rajpurohit, K., Lovisari, L., Botteon, A., et al. 2024, ApJ, 966, 38
Rajpurohit, K., Vazza, F., Hoeft, M., et al. 2020, A&A, 642, L13
Rajpurohit, K., Vazza, F., van Weeren, R. J., et al. 2021, A&A, 654, A41
Randall, S. W., Markevitch, M., Clowe, D., Gonzalez, A. H., & Bradač, A. H. 2008, ApJ, 679, 1173
Reid, A. D., Hunstead, R. W., Lemonon, L., & Pierre, M. M. 1999, MNRAS, 302, 571
Rumsey, C., Perrott, Y. C., Olamaie, M., et al. 2017, MNRAS, 470, 4638
Santra, R., Kale, R., Giacintucci, S., et al. 2024, ApJ, 962, 40
Sarazin, C., Hogge, T., Chatzikos, M., et al. 2014, The X-ray Universe 2014, ed. J.-U. Ness, (ESA), 181
Sarazin, C. L. 2002, in Merging Processes in Galaxy Clusters, ed. L. Feretti, I. M. Gioia, & G. Giovannini (Dordrecht: Kluwer Academic), 1
Sarkar, A., Andrade-Santos, F., van Weeren, R. J., et al. 2024, ApJ, 962, 161
Schrabback, T., Applegate, D., Dietrich, J. P., et al. 2018, MNRAS, 474, 2635
Sehgal, N., Hughes, J. P., Wittman, D., et al. 2008, ApJ, 673, 163
Seitz, C., & Schneider, P. 1997, A&A, 318, 687
Shibata, R., Honda, H., Ishida, M., Ohashi, T., & Yamashita, K. 1999, ApJ, 524, 603
Shimwell, T. W., Luckin, J., Brüggen, M., et al. 2016, MNRAS, 459, 277
Shweta, A., Athreya, R., & Sekhar, S. 2020, ApJ, 897, 115
Sirianni, M., Jee, M. J., Benìtez, N., et al. 2005, PASP, 117, 1049
Skillman, S. W., Xu, H., Hallman, E. J., et al. 2013, ApJ, 765, 21

Sommer, M. W., Schrabback, T., Applegate, D. E., et al. 2022, MNRAS, 509, 1127
Sommer, M. W., Schrabback, T., Ragagnin, A., & Rockenfeller, R. 2024, MNRAS, 532, 3359
Soucail, G. 2012, A&A, 540, A61
Stancioli, R., Wittman, D., Finner, K., & Bouhrik, F. 2024, ApJ, 966, 49
Stroe, A., Harwood, J. J., Hardcastle, M. J., & Röttgering, H. J. A. 2014a, MNRAS, 445, 1213
Stroe, A., Rumsey, C., Harwood, J. J., et al. 2014b, MNRAS, 441, L41
Stroe, A., Shimwell, T., Rumsey, C., et al. 2016, MNRAS, 455, 2402
Stroe, A., van Weeren, R. J., Intema, H. T., et al. 2013, A&A, 555, A110
Stuardi, C., Bonafede, A., Lovisari, L., et al. 2021, MNRAS, 502, 2518
Stuardi, C., Bonafede, A., Rajpurohit, K., et al. 2022, A&A, 666, A8
Stuardi, C., Bonafede, A., Wittor, D., et al. 2019, MNRAS, 489, 3905
Sunyaev, R. A., & Zeldovich, Y. B. 1972, CoASP, 4, 173
Suto, D., Kawahara, H., Kitayama, T., et al. 2013, ApJ, 767, 79
Takizawa, M., Nagino, R., & Matsushita, K. 2010, PASJ, 62, 951
Terni de Gregory, B., Hugo, B., Venturi, T., et al. 2021, MNRAS, 504, 2924
Thölken, S., Reiprich, T. H., Sommer, M. W., & Ota, N. 2018, A&A, 619, A68
Tody, D. 1986, Proc. SPIE, 627, 733
Umetsu, K., Medezinski, E., Nonino, M., et al. 2014, ApJ, 795, 163
Umetsu, K., Sereno, M., Lieu, M., et al. 2020, ApJ, 890, 148
Vacca, V., Govoni, F., Murgia, M., et al. 2022a, MNRAS, 514, 4969
Vacca, V., Shimwell, T., Perley, R. A., et al. 2022b, MNRAS, 511, 3389
van Weeren, R. J., Andrade-Santos, F., Dawson, W. A., et al. 2017, NatAs, 1, 0005
van Weeren, R. J., Bonafede, A., Ebeling, H., et al. 2012a, MNRAS, 425, L36
van Weeren, R. J., Brüggen, M., Röttgering, H. J. A., & Hoeft, M. 2011a, JApA, 32, 505
van Weeren, R. J., Brüggen, M., Röttgering, H. J. A., et al. 2011b, A&A, 533, A35
van Weeren, R. J., Brunetti, G., Brüggen, M., et al. 2016, ApJ, 818, 204
van Weeren, R. J., de Gasperin, F., Akamatsu, H., et al. 2019, SSRv, 215, 16
van Weeren, R. J., Fogarty, K., Jones, C., et al. 2013, ApJ, 769, 101
van Weeren, R. J., Hoeft, M., Röttgering, H. J. A., et al. 2011c, A&A, 528, A38
van Weeren, R. J., Röttgering, H. J. A., Bagchi, J., et al. 2009, A&A, 506, 1083
van Weeren, R. J., Röttgering, H. J. A., Brüggen, M., & Hoeft, M. 2010, Sci, 330, 347
van Weeren, R. J., Röttgering, H. J. A., Intema, H. T., et al. 2012b, A&A, 546, A124
Vazza, F., Brüggen, M., van Weeren, R., et al. 2012, MNRAS, 421, 1868
Vazza, F., Brüggen, M., Wittor, D., et al. 2016, MNRAS, 459, 70
Venturi, T., Giacintucci, S., Dallacasa, D., et al. 2008, A&A, 484, 327
Venturi, T., Giacintucci, G., Dallacasa, D., et al. 2011, MNRAS, 414, L65
Venturi, T., Giacintucci, S., Dallacasa, D., et al. 2013, A&A, 551, A24
Weaver, J. R., Kauffmann, O. B., Ilbert, O., et al. 2022, ApJS, 258, 11
Wittman, D., Cornell, B. H., & Nguyen, J. 2018, ApJ, 862, 160
Wittman, D., Dawson, W., & Benson, B. 2014, MNRAS, 437, 3578
Wittman, D., Dell'Antonio, I. P., Hughes, J. P., et al. 2006, ApJ, 643, 128
Wittman, D., Stancioli, R., Finner, K., et al. 2023, ApJ, 954, 36
Wittman, D. M., Tyson, J. A., Dell'Antonio, I. P., et al. 2002, Proc. SPIE, 4836, 73
Wright, C. O., & Brainerd, T. G. 2000, ApJ, 534, 34
Yagi, M., Kashikawa, N., Sekiguchi, M., et al. 2002, AJ, 123, 66
Yoo, J., Ko, J., Sabiu, C. G., et al. 2022, ApJS, 261, 28
Yoo, J., Park, C., Sabiu, C. G., et al. 2024, ApJ, 965, 145
Yoon, M., Lee, W., Jee, M. J., et al. 2020, ApJ, 903, 151
Zhang, C., Churazov, E., Forman, W. R., & Jones, C. 2019, MNRAS, 482, 20
Zhang, X., Simionescu, A., Akamatsu, H., et al. 2020, A&A, 642, A89
Zhang, X., Simionescu, A., Stuardi, C., et al. 2021, A&A, 656, A59
Ziparo, F., Braglia, F. G., Pierini, D., et al. 2012, MNRAS, 420, 2480
Zitrin, A., Bartelmann, M., Umetsu, K., Oguri, M., & Broadhurst, T. 2012, MNRAS, 426, 2944
ZuHone, J. A., Kowalik, K., Öhman, E., Lau, E., & Nagai, D. 2018, ApJS, 234, 4